Structural and strain analysis in the Late Paleozoic coastal accretionary wedge of central Chile

Dissertation
zur Erlangung des Grades

„Doktor der Naturwissenschaften"

am Fachbereich 09: Chemie, Pharmazie und Geowissenschaften

der Johannes Gutenberg-Universität in Mainz

Peter Paul Erich Richter
geboren in Aachen

Mainz, August 2007

Erklärung

Ich versichere hiermit die Arbeit selbstständig und nur unter Verwendung der angegebenen Quellen und Hilfsmittel verfasst zu haben.

Mainz, August 2007

Abstract

In this study structural and finite strain data are used to explore the tectonic evolution and the exhumation history of the Chilean accretionary wedge. The Chilean accretionary wedge is part of a Late Paleozoic subduction complex that developed during subduction of the Pacific plate underneath South America. The wedge is commonly subdivided into a structurally lower Western Series and an upper Eastern Series. This study shows the progressive development of structures and finite strain from the least deformed rocks in the eastern part of the Eastern Series of the accretionary wedge to higher grade schist of the Western Series at the Pacific coast. Furthermore, this study reports finite-strain data to quantify the contribution of vertical ductile shortening to exhumation. Vertical ductile shortening is, together with erosion and normal faulting, a process that can aid the exhumation of high-pressure rocks.

In the east, structures are characterized by upright chevron folds of sedimentary layering which are associated with a penetrative axial-plane foliation, S_1. As the F_1 folds became slightly overturned to the west, S_1 was folded about recumbent open F_2 folds and an S_2 axial-plane foliation developed. Near the contact between the Western and Eastern Series S_2 represents a prominent subhorizontal transposition foliation. Towards the structural deepest units in the west the transposition foliation became progressively flat lying. Finite-strain data as obtained by Rf/ϕ and PDS analysis in metagreywacke and X-ray texture goniometry in phyllosilicate-rich rocks show a smooth and gradual increase in strain magnitude from east to west. There are no evidences for normal faulting or significant structural breaks across the contact of Eastern and Western Series. The progressive structural and strain evolution between both series can be interpreted to reflect a continuous change in the mode of accretion in the subduction wedge. Before ~320-290 Ma the rocks of the Eastern Series were frontally accreted to the Andean margin. Frontal accretion caused horizontal shortening and upright folds and axial-plane foliations developed. At ~320-290 Ma the mode of accretion changed and the rocks of the Western Series were underplated below the Andean margin. This basal accretion caused a major change in the flow field within the wedge and gave rise to vertical shortening and the development of the penetrative subhorizontal transposition foliation.

To estimate the amount that vertical ductile shortening contributed to the exhumation of both units finite strain is measured. The tensor average of absolute finite strain yield S_x=1.24, S_y=0.82 and S_z=0.57 implying an average vertical shortening of ca. 43%, which was compensated by volume loss. The finite strain data of the PDS measurements allow to calculate an average volume loss of 41%. A mass balance approximates that most of the solved material stays in the wedge and is precipitated in quartz veins. The average of relative

finite strain is S_x=1.65, S_y=0.89 and S_z=0.59 indicating greater vertical shortening in the structurally deeper units. A simple model which integrates velocity gradients along a vertical flow path with a steady-state wedge is used to estimate the contribution of deformation to ductile thinning of the overburden during exhumation. The results show that vertical ductile shortening contributed 15-20% to exhumation. As no large-scale normal faults have been mapped the remaining 80-85% of exhumation must be due to erosion.

Zusammenfassung

In dieser Studie werden strukturelle und finite Verformungsdaten benutzt um die tektonische Entwicklung und die Exhumierungsgeschichte des chilenischen Akkretionskeils zu untersuchen. Dieser ist Teil eines spätpaläozoischen Subduktionskomplexes, der sich während der Subduktion der Pazifischen Platte unter Südamerika gebildet hat. Der Keil wird üblicherweise in eine strukturell tiefer liegende Westliche Serie und eine strukturell höher liegende Östliche Serie unterteilt. In dieser Studie wird eine progressive Entwicklung und Veränderung von Struktur- und Verformungsdaten aufgezeigt, angefangen in den am wenigsten deformierten Gesteinen der Östlichen Serie bis hin zu den höhergradig deformierten Gesteinen in der Westlichen Serie an der pazifischen Küste. Des weiteren wird mit den finiten Verformungsdaten der Anteil der vertikalen duktilen Ausdünnung an der Gesamtexhumierung quantifiziert. Vertikale duktile Ausdünnung ist neben Erosion und Abschiebungstektonik ein Prozess, der zur Exhumierung von Hochdruckgesteinen führen kann.

Im östlichen Teil der Östlichen Serie sind die Strukturen durch sedimentäre Lagen charakterisiert. Diese sind mit einer penetrativen S_1 Schieferung assoziiert und durch aufrechte Chevron-Falten verfaltet. Das Einfallen dieser F_1 Falten ändert sich nach Westen hin von Ost- zu West-vergent. Die S_1 Schieferung wird Richtung Westen zusehends an liegenden, offenen F_2 Falten verfaltet und es bildet sich parallel zu den Achsenebenen eine S_2 Schieferung aus. Am Übergang zwischen Östlicher und Westlicher Serie stellt S_2 eine markante subhorizontal orientierte Transpositionsfoliation dar. In den strukturell tiefsten Einheiten im Westen wird diese Transpositionsfoliation immer flachliegender. Die finiten Verformungsdaten, die man aus den Analysen mit der Rf/ϕ- und PDS-Methode an Metagrauwacken und mit der XTG-Methode an Phyllosilikat reichen Gesteinen erhält, zeigen einen gleichmäßigen und graduellen Anstieg der Verformungsmagnitude von Ost nach West. Diese progressive Entwicklung kann dahingehend interpretiert werden, dass sie eine kontinuierliche Änderung des Akkretionsmodus in der Subduktionszone darstellt. In der Zeit vor ~320-290 Ma wurden die Gesteine der Östlichen Serie frontal am Plattenrand akkretiert. Diese Art der Akkretion verursachte horizontale Verkürzung und die aufrecht stehenden Falten. Um ~320-290 Ma änderte sich der Akkretionsmodus und die Gesteine der Westlichen Serie wurden unter den Plattenrand subduziert und basal akkretiert. Dies verursachte eine starke Veränderung der Art der Deformation im Keil. Die Gesteine wurden nun vertikal verkürzt und es bildete sich die penetrative Transpositionsfoliation.

Die absoluten und relativen Verformungsdaten der beiden Serien werden außerdem benutzt um den Anteil der vertikalen duktilen Ausdünnung an der Gesamtexhumierung zu quantifizieren. Tensormittelwerte der Hauptverformungsachsen der absoluten Verformungsdaten ergaben $S_x=1,24$, $S_y=0,82$ und $S_z=0,57$ und implizieren eine vertikale Verkürzung von ca. 43 %, die durch Volumenverlust kompensiert wird. Aus den Verformungsdaten der PDS-Messungen lässt sich ein durchschnittlicher Volumenverlust von 41 % errechnen. Mit einer Massenbilanz lässt sich abschätzen, dass der größte Teil des gelösten Materials im Akkretionskeil bleibt und in Form von Quarzadern wieder ausfällt. Für die Tensormittelwerte der relativen Verformungsdaten lassen sich Werte von $S_x=1,65$, $S_y=0,89$ und $S_z=0,59$ bestimmen. Diese indizieren eine stärkere vertikale Verkürzung für die strukturell unteren Einheiten als für die höher gelagerten. Ein einfaches Model, welches Geschwindigkeitsgradienten entlang eines vertikalen Flusspfades in einem Gleichgewichtskeil integriert, kann zur Bestimmung des Anteils der vertikalen duktilen Ausdünnung an der Gesamtexhumierung genutzt werden. Die Ergebnisse zeigen, dass dieser Anteil nur ca. 15-20 % ausmacht. Da keine großmaßstäblichen Abschiebungen beobachtet werden können, ist davon auszugehen, dass die restlichen 80-85 % der Exhumierung auf Erosion zurückgehen.

Table of contents

1. Introduction and problem definition

The circumpacific area is characterized at its continental margins by several accretionary systems (Fig. 1.1). These accretionary systems have been the focus of research for a long time. A typical example for such an accretionary system is the Chilean accretionary wedge, which is part of a Late Paleozoic subduction complex that developed during subduction of the Pacific plate underneath South America. In this study parts of the Chilean accretionary wedge are investigated with the main focus on the problems described in the following chapters (1.1-1.3).

1.1 Mode of accretion

The wedges in the circumpacific area show different types of architectures, which probably reflect different modes of accretion. Basically two different types of architectures are distinguished. On the one hand in the Franciscan, Aleutian and Japanese accretionary wedges, higher grade rocks tectonically rest above lower grade ones (MIYASHIRO, 1973; SUPPE, 1973; COWAN, 1974; PLATT, 1975; MOORE & ALLWARDT, 1980). For the Franciscan accretionary wedge it has been shown that the major tectonic contacts are postmetamorphic. Their development is considered to be a result of a late-stage out of sequence faulting (PLATT, 1975; SUPPE, 1978; BOLHAR & RING, 2001; RING & BRANDON, 1994, 1999, 2006; RING & RICHTER, 2004).

Fig. 1.1: Map showing the circumpacific accretionary wedges.
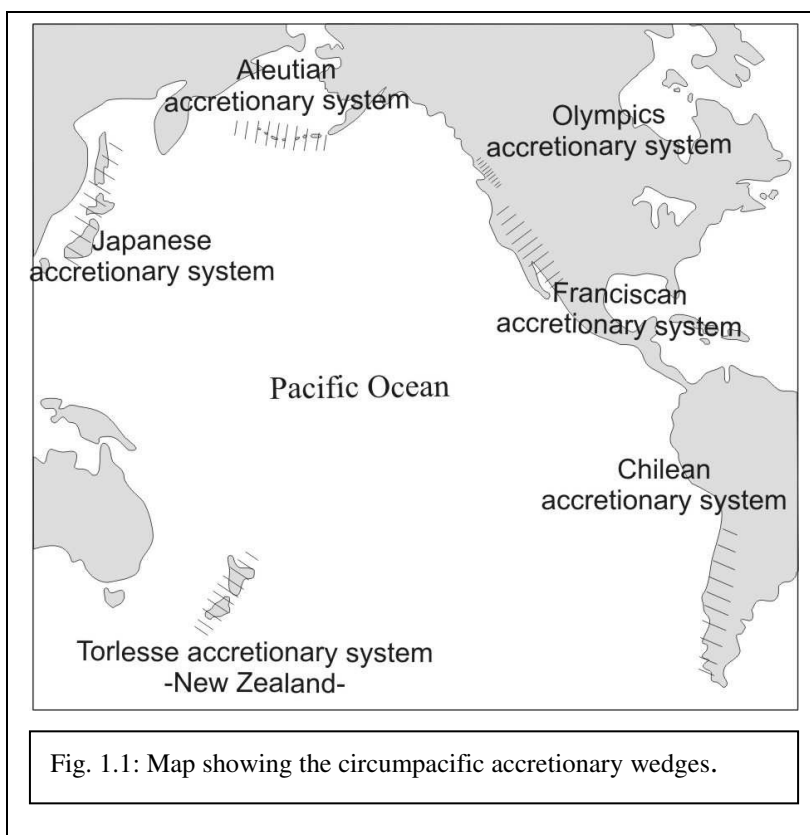
In the Franciscan, Aleutian and Japanese wedges, the rocks were initially underplated and subsequently accretion became frontal, which caused late horizontal shortening across the wedge. On the other hand, in the Torlesse accretionary belt of New Zealand, the Olympics

subduction complex of western North America and the coastal accretionary wedge of Chile, the highest grade rocks occur in the tectonically deepest levels and metamorphic grade decreases structurally upwards (HERVÉ, 1988, BRANDON & CALDERWOOD,1990, MORTIMER, 1993, DECKERT ET AL., 2002). In these wedges the rocks were initially frontal accreted and changed into underthrusting with a basal mode of accretion. The transition between higher and lower grade rocks remained largely obscure.

The consequences of these changes in the mode of accretion are illustrated with the flow-field concept of Feehan & Brandon (1999) and Ring et al. (1999). Generally, different modes of accretion cause different types of material flow and lead to different flow fields within the wedge. There are two end members: (1) In the first case frontal accretion is depicted. Erosion at the top of the wedge causes material flow towards the upper rear part of the wedge. Due to the converging flow lines a thickening flow field develops, showing wholesale horizontal contraction. (2) In contrast, the second case shows basal accretion. Underplating to the base of the wedge and erosion at the top of the accretionary wedge leads to a thinning flow field. It is
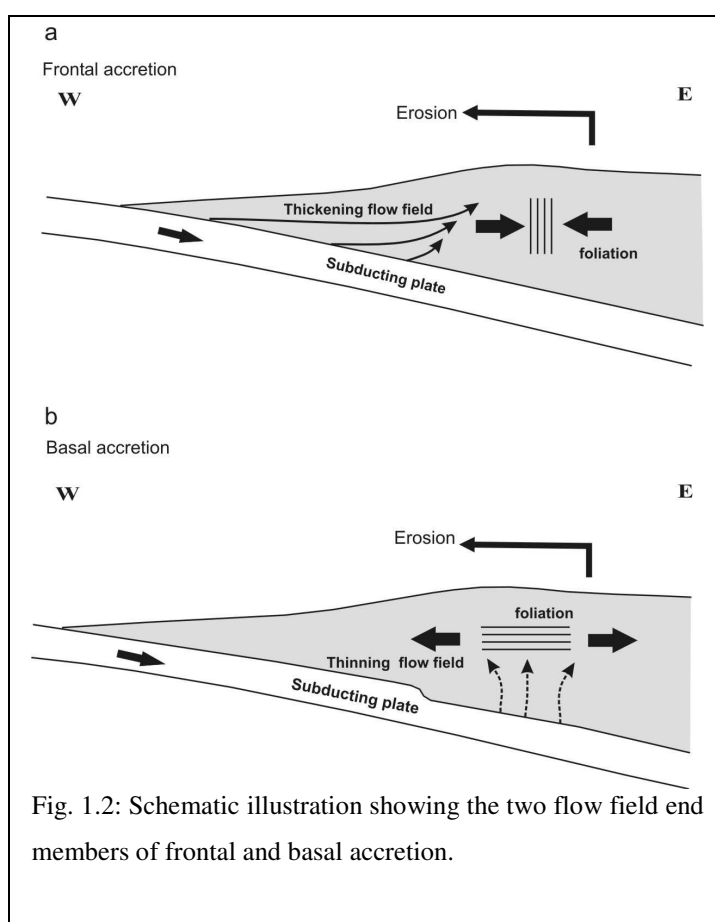
Fig. 1.2: Schematic illustration showing the two flow field end members of frontal and basal accretion.

characterized by diverging flow lines which cause a widespread vertical contraction, indicating horizontal extension in the rear of the wedge (Fig. 1.2). There are intermediate cases between those two end-member types of accretion. A major question is whether the changes in the mode of accretion are transitional or abrupt.

In this study structural and finite strain data are presented in order to develop a tectonic model for the Chilean accretionary wedge, which is well exposed in Central Chile. Thereby the question of the mode of accretion of different rock series will be addressed.

1.2 Exhumation mechanisms

Beside the mode of accretion the exhumation of deeply subducted rocks is a fundamental problem in tectonics. Erosion, normal faulting and ductile thinning represent the main exhumation mechanisms (Fig. 1.3) and it is of special interest which of these mechanisms is the most important one (PLATT, 1993, BRANDON & RING, 1997, RING ET AL., 1999). The deeply subducted rocks of the accretionary wedge of central Chile are exhumed from c. 35-40 km depth, which corresponds with the observations of similar circumpacific wedges.

Fig.1.3: Schematic illustration of an accretionary wedge showing erosion, normal faulting and ductile thinning after Feehan & Brandon 1999. Left graph shows the linearity of the velocity gradient tensor L(z) in dependency with depth. The right graph shows that the amount of ductile thinning increases exponentially with depth, when propotional strain rate law is integrated over wedge thickness.

For the Franciscan accretionary wedge it was proved by Ring & Brandon (1999) and for the Olympic accretionary system by Brandon et al. (1998), that the exhumation is mainly erosion driven. In this study it is investigated, if this is valid for the Chilean accretionary wedge as well.
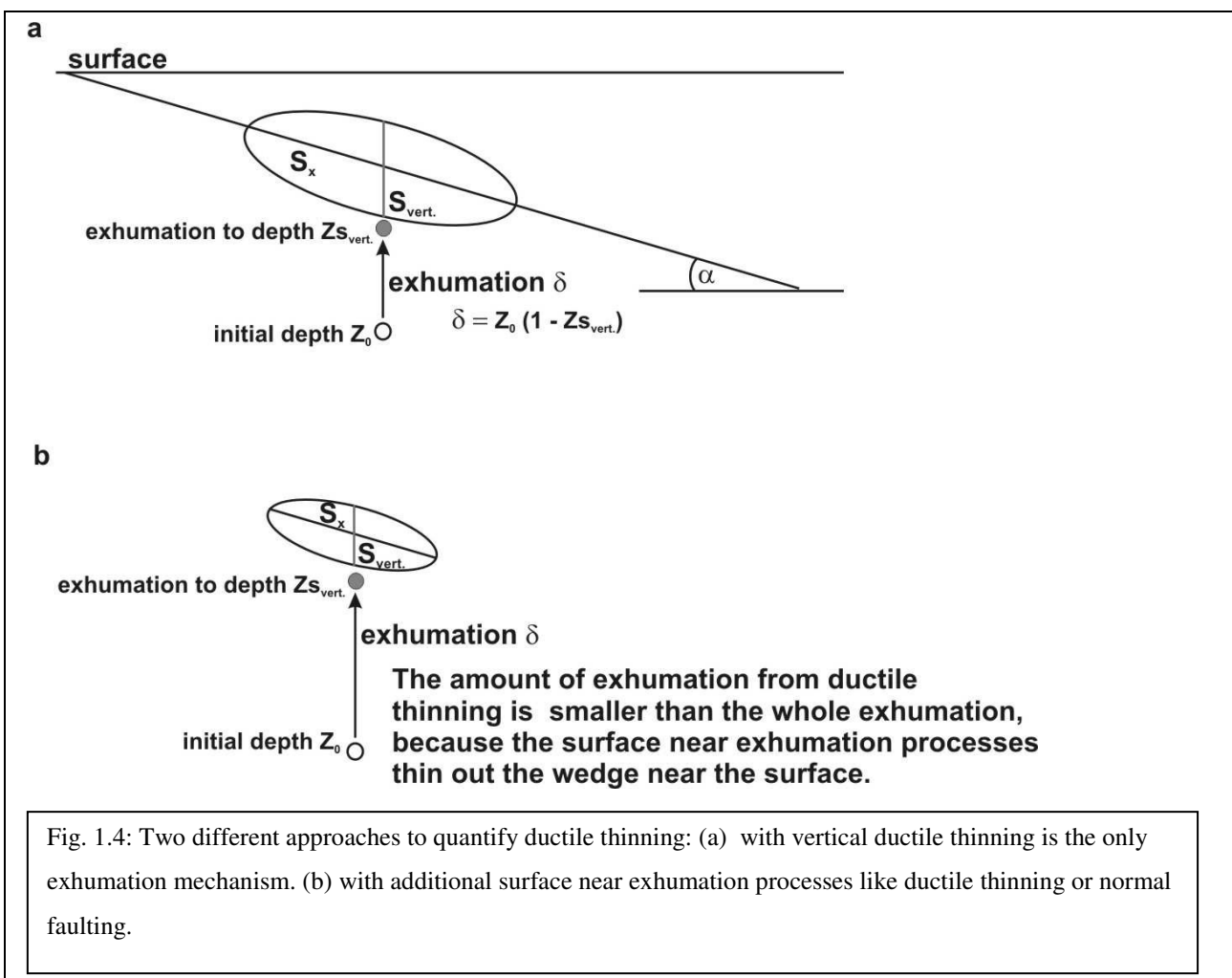
However, ductile thinning is commonly seen as an important exhumation mechanism. (SELVERSTONE, 1985, WALLIS ET AL., 1993, PLATT, 1993, WALLIS & BEHRMANN, 1996, FEEHAN & BRANDON, 1999, RING & BRANDON, 1999). Vertical ductile thinning is the measure of the amount of vertical shortening and closely connected with cleavage formation (RING ET

AL., 1999). Therefore, it is of special interest to quantify the contribution of vertical ductile shortening to exhumation.

Here are two different approaches to quantify ductile thinning: Assuming the easiest case that vertical ductile thinning is the only exhumation mechanism, exhumation can be described by the three dimensional position of the strain ellipsoid. The vertical stretch $S_{vert.}$ (with S=final length/initial length) is depending on the dimension of the bedding. The exhumation (δ) of a single grain, starting from an initial depth z_0 and ending at a second depth z_1 can be described by the equation: $\delta = z_1 (1- S_{vert.})$ (Fig. 1.4(a)). Certainly rocks only can be exhumed completely by vertical ductile thinning if $S_{vert.} = 0$, which corresponds with 100% shortening. Therefore, there must be other exhumation mechanisms either, which is probably the normal case in nature. This second case is illustrated in Fig. 1.4(b).

The exhumation from vertical ductile thinning is supplemented by an additional near surface exhumation process like erosion or normal faulting. Because of this surface near process, the bedding is thinned out faster than in the first case with ductile thinning as the only exhumation process. Thus, every increase of vertical ductile thinning distributes faster through a continuously thinned out block of the overlying bedding.

This means that there is a decrease in the increment of vertical ductile thinning from total exhumation. Furthermore, the ratio of vertical ductile thinning is depending on the deformation rate which is on its part regulated by depth. This means the nearer a particle is exhumed to the surface the smaller is the rate of vertical ductile thinning. Because of the continuously decrease of the amount of the overlying bedding the deformation rate decreases as well. Therefore, a model for quantifying vertical ductile thinning should contain the vertical ratio of rocks migrating through the wedge, as well as the ratio of the thinning of the overlying bedding in every point of the exhumation path. Feehan & Brandon (1999) developed a one dimensional model (Fig 1.3) describing the exhumation and the ductile thinning of a particle migrating through an accretionary wedge.

Fig. 1.4: Two different approaches to quantify ductile thinning: (a) with vertical ductile thinning is the only exhumation mechanism. (b) with additional surface near exhumation processes like ductile thinning or normal faulting.

The process of vertical ductile thinning has been quantified so far in only a very few studies (e.g. FEEHAN & BRANDON, 1999, RING & BRANDON, 1999). They unravelled that vertical ductile thinning contributes much less to exhumation than the maximum shortening in exhumed rocks near the surface shows. In these studies it has been determined, that the average amount of vertical ductile thinning captures only about 30% from exhumation.

1.3 Volume change in the wedge

Previous geochemical and strain studies found evidence for volume changes related to deformation in thrust belts (NEWMAN & MITRA, 1993, RING, 1996, RING ET AL. 2001). Beside loss of porosity, e.g. after compaction (PATERSON ET AL., 1995) and change in grain densities during mineral phase transitions (AUSTRHEIM ET AL., 1997), this is volume change due to dissolution processes (RAMSAY & WOOD, 1973, RING & BRANDON, 1999). The investigations of this study are focussed on the last point.

Related to this it is a question of interest, weather possibly solved material is transported over long distances out of the wedge, or if this material reprecipitates in the wedge again. In the first case the accretionary system would be an open system with a general volume loss. In the second case it would be a closed system which is on a larger scale volume constant.

In huge parts of the Coastal Cordillera in central Chile quartz veining is very prominent and might be related to dissolved SiO_2 material in the wedge.

However, in this study the average volume loss for the Chilean accretionary wedge is calculated and due to this, the influence of the dissolved material to quartz veining on different scales is estimated. In order to quantify the ratio of solved material from quartz grains in the wedge and the amount of precipitated material in quartz veins a mass balance is presented in this study (see chapter *11: Mass balance*).

2. Geographic overview

The Late Paleozoic accretionary wedge of central Chile is well exposed and therefore, it is possible to quantify deformation processes and to develop a model for the exhumation of the deeply subducted rocks of the Chilean accretionary wedge.

The area investigated in this study is localized in the metamorphic basement (light grey in Fig. 2.1) of the Coastal Cordillera of Central Chile and can be divided into two parts: One ranges from Constitución to Pichilemu between ~33°S-36°S. The other one is further in the north and ranges between 30°S and 31° 30´´S near Huantelauquen. The southernmost part, in this case the area near Constitución, represents a nearly undisturbed sequence of the ancient accretionary wedge. In contrast, the regions further in the north (near Pichilemu (~34°S) and near Huantelauquen (~31°S)) have been slightly overprinted by structures of younger events. The geological setting is described in the following:

Fig. 2.1.: Oveview over central Chile with two different working areas in the metamorphic basement between 30°S and 36°S.
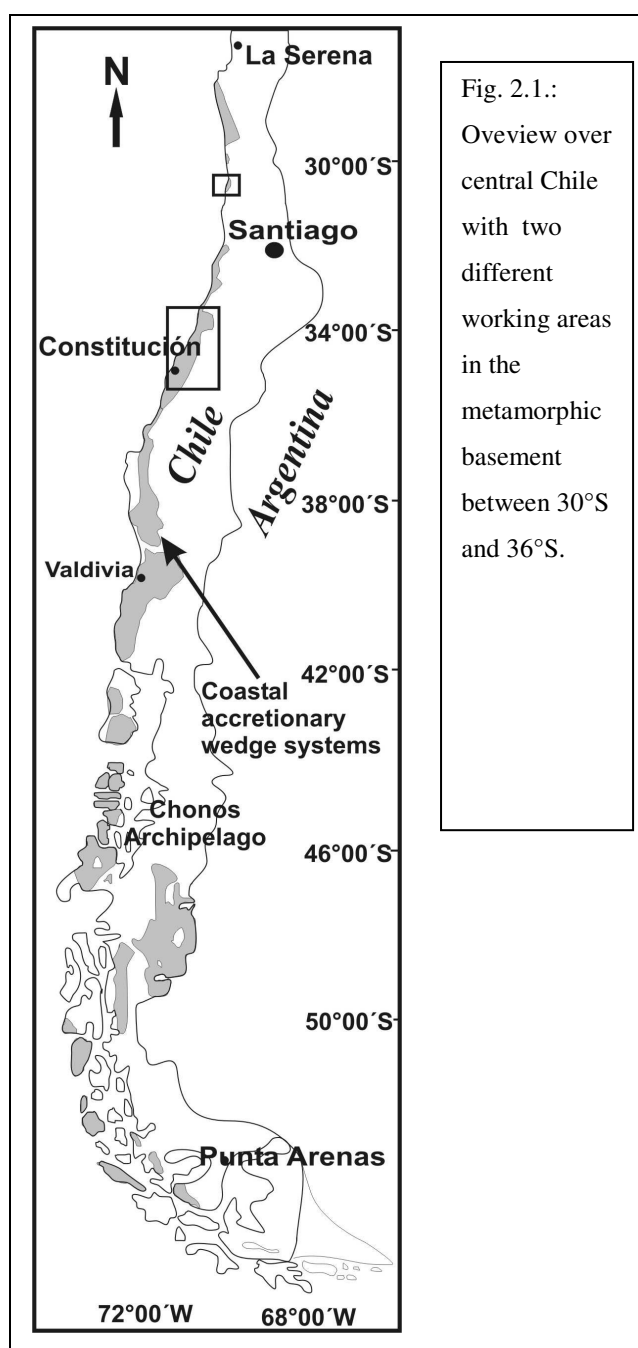
3. Geological setting

The Chilean accretionary wedge is part of a Late Paleozoic to Triassic subduction complex that developed during subduction of the Pacific plate underneath South America (Hervé, 1988). It represents a typical subduction complex with an accretionary wedge, a fore arc basin and a magmatic arc which crops out in a 50 – 100 km wide belt along the Chilean coast from central Chile to Tierra del Fuego. In northern Chile, this complex was strongly overprinted during ongoing activity along the convergent margin. In central Chile the pre-Andean subduction architecture is well preserved. The wedge is commonly subdivided into a structurally lower Western Series and an upper Eastern Series within the pre-Andean coastal accretionary belt, representing different tectonic environments (GONZÁLEZ-BONORINO, 1971; AGUIRRE ET AL., 1972; KATO, 1985; HERVÉ, 1988; WILLNER ET AL., 2005). The Western Series is composed of metagreywacke and metapelite of continental provenance as well as penetratively deformed and recrystallized metachert, metabasite and pervasive serpentinite assemblages (chlorite zone of lower greenshist grade) of oceanic origin (HERVE, 1974, 1981; KATO, 1985). Metamorphic conditions in the Western Series between 34°-36°S reached 7-11 kbar and 380-420°C at 320-290 Ma (WILLNER, 2005; WILLNER ET AL., 2005). Furthermore, in the Western Series quartz veining is prominent with veins up to one decimetre wide. Structurally it is characterized by a subhorizontal transposition foliation with pronounced banding. The Western Series is formed by basal accretion with slow exhumation rates of 0.2-0.6 km Myr^{-1} (GLODNY ET AL., 2005, WILLNER ET AL., 2005). In the Late Triassic, the Western Series was intruded by a few post-accretion granites.

The overlying Eastern Series consists of metagreywacke and metapelite, interpreted as continent-derived, turbidite successions (KATO, 1985; HERVÉ, 1988). Oceanic derived rocks like metachert, metabasite and serpentinite are largely absent and the lack of oceanic rocks is thought to be the most important feature for distinguishing between both series (GODOY & KATO, 1990; GLODNY ET AL., 2005) although it cannot really be used as a prime criterion, because Hervé et al. (2000) and Marioth (2001) observed metabasite occurrences in units between 44° and 46° S and at 26°S, which are structurally similar to the Eastern Series.

Between 34° and 36°S subduction- and accretion related metamorphic conditions in the Eastern Series are overprinted by a later contact metamorphism at 3kbar (WILLNER, 2005). In southern Chile between 44°-46°S, Willner et al. (2000) reported subduction- and accretion-related PT conditions of 4.5-6 kbar and 250-280°C. Similar PT conditions can be inferred from rocks in structural units comparable with the Eastern Series at 26°S (MARIOTH, 2001).

Along the entire Coastal Cordillera, where the high-temperature overprint does not occur, the white mica in the Eastern Series is high-Si phengite and part of very low-grade mineral assemblages of the pumpellyite-actinolite facies (WILLNER ET AL., 2000). Structurally it is characterized by large-scale, upright chevron folds, which are increasingly flattened and tightened structurally downwards. In the easternmost parts of the Eastern Series, which are structurally the uppermost parts, remaining sedimentary structures can be observed and within these areas pressure solution is the main deformation mechanism. The Eastern Series are the host rocks of Late Palaeozoic calc-alkaline batholiths between 32-36°S with a maximum of intrusion activity around 300 Ma (HERVÉ ET AL., 1988; LUCASSEN ET AL., 2004; WILLNER ET AL., 2005). The intrusions were accompanied by a high-temperature overprint that increases from biotite grade to andalusite-sillimanite grade towards the batholiths. Radiometric data constrain this contact metamorphic overprint at 300 Ma (WILLNER ET AL., 2005). $^{40}Ar/^{39}Ar$ ages from white mica that formed during the static high-temperature overprint show ages at 296–301 Ma. These ages are in accord with older K-Ar biotite ages ranging from 306 to 284 Ma and Rb-Sr whole-rock isochron ages of granites ranging from 312-294 Ma (HERVÉ, 1988; LUCASSEN ET AL., 2004).

During Mesozoic times tectonic events occurred episodically and shortened the continental margin by subduction erosion, which also affected the metamorphic basement (SCHEUBER ET AL., 1994; SCHEUBER & GONZALEZ, 1999). North of 35°S there were two contractional events have been noted within the forearc and during Jurassic times subduction direction was NW. This caused a sinistral strike-slip system stretching (SCHEUBER ET AL., 1994; SCHEUBER & GONZALEZ, 1999). In ~mid cretaceous times a second shortening event closed the Mesozoic intra –arc basins again (e.g. WILLNER ET AL., 2005).

It has been proposed by numerous authors that the Eastern Series and the Western Series represent a paired metamorphic belt (AGUIRRE ET AL., 1972; ERNST, 1975; KATO, 1985; HERVÉ, 1988; WILLNER ET AL., 2005). In both series a subhorizontal stretching lineation can be observed in the field as well as from the measured samples. The Eastern Series and the Late Paleozoic batholith in central Chile are in part overlain by Late Triassic to Early Cretaceous marine siliciclastic sediments and bimodal volcanic rocks. Initial deposition coincided in time with Triassic post-accretion granites in the Western Series. To the south of 40°S the rocks of the accretionary wedge are overlain by volcanosedimentary series of Jurassic ages (HERVÉ ET AL., 2000).

The contact between the Eastern and Western Series can be traced for more than 1500 km from ~31°S to ~50°S and has a general north-south orientation. In most places the contact has

been strongly overprinted by post-subduction structures. These structures either coincide with a Late Triassic rifting event or a mid-Cretaceous to recent crustal shortening event as a result of the modern Andean orogeny. The nature of this contact has been so far a long standing problem: it has been either interpreted as a transitional or a tectonic contact. It is a fundamental question whether both series belong to the subducting plate (GLODNY ET AL., 2005) or whether the Eastern Series is part of the overriding plate (ERNST, 1975, HERVÉ, 1988). Aguirre et al. (1972) and Ernst (1975) inferred that the Eastern and Western series are genetically associated and coeval. Ernst (1975) referred to the contact as the Coast Range Suture and argued that it represents an ancient convergent plate boundary, which implies that it has plate-tectonic dimensions. Hervé considered the Eastern Series to represent a Devonian passive margin that existed before onset of subduction, but the Western Series to be part of an accretionary wedge. Furthermore Willner (2005) considered the Western Series as underplated trench sediments now resting to the west of the stationary and older Eastern Series. All these interpretations have in common, that they imply a major tectonic contact separating both series from each other. In contrast, Godoy (1970), Gonzalez-Bonorino (1971) and Hervé (1988) noted a gradual structural transition across the contact between the Eastern and Western series at 34°-35°30´S. The only other region, where a transitional contact was considered in the Chilean basement is in the Chonos Archipelago at 44-46°S (DAVIDSON ET AL., 1987). All these studies inferred that the Eastern Series rocks were deposited east and inboard of the Western series. Concerning the contact, the working area of this study can be divided into three parts. The Rio Maule area, which represents a continuous structural section and shows smooth transition between the both series, the Pichilemu region, where the contact is characterized by the Pichilemu – Vichuquén Fault, which has been shown to be a post accretional brittle structure (WILLNER ET AL., 2005) and the Los Vilos region, where Eastern and Western Series are separated by a younger system of mostly sinistral shear zones.

4. Parameters of strain analyses

For the strain analyses, which is carried out in this study first some basic principles have to be defined: Based on the assumption that an undeformed geological body is a sphere with the radius r = 1, there are several parameters for changing shape under the influence of strain. These are changes in length of the axes, volume change and changes of the angles between the axes. The original sphere produces an ellipsoid, whose principal axes are the principal directions of extension (TWISS & MOORES, 1992). This strain ellipsoid is characterised by the length of the three principal axes X, Y, Z and the equation $X \geq Y \geq Z$. The lengths of these axes are changed during deformation. The stretch S is defined by:

$$S = \frac{L_f}{L_i}$$

with: L_f = finite length

L_i = initial length

Elongations e are equivalent parameters:

$$e = \frac{L_f - L_i}{L_i} = \frac{\Delta L}{L_i}$$

For the elongation and the stretch the equations $S_x \geq S_y \geq S_z$ and $e_x \geq e_y \geq e_z$ are given. Another important parameter is the volume change (ΔV) of the volume V. It is defined by the relation of a measured volume V to an initial volume and it is given by the equation:

$$\frac{\Delta V}{V_0} = \frac{V_0 - V_1}{V_0}$$

with: V_0 = initial volume
V_1 = final volume
ΔV = Volume change

To describe the change of the angle between two initially perpendicular axes during shearing the equation $\gamma = \tan \psi$ (RAMSAY & HUBER, 1983) is given.

First two orthogonal lines p and q change their orientation and take up the position of p´and q´. The geometric significance γ becomes clear if the relation of the two lines at the point with the distance 1 from the intersection point is considered after deformation.

With this, the parameters strain symmetry and strain type can be described.

4.1 Strain symmetry

To describe the strain symmetry of a homogenous deformation Park (1983) distinguished three different cases:

a)   Prolate strain symmetry

 Extension in X- direction and shortening in Y and Z direction can be obtained.

Fig. 4.1: From PARK, 1983: prolate strain symmetry
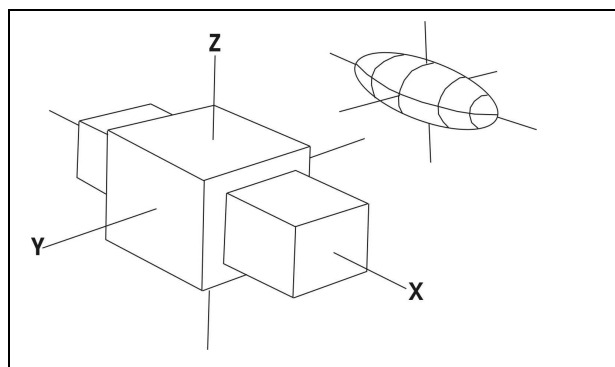
b) Oblate strain symmetry

This case shows shortening in Z direction and extension in X- and Y-direction.

Fig. 4.2: From PARK, 1983: oblate strain symmetry
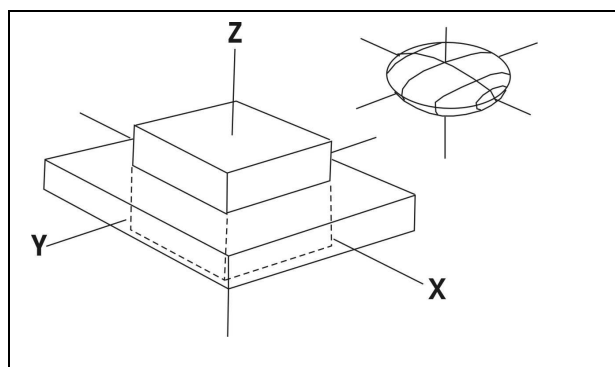
c) Plane strain

The length of the Y-axis stays constant. There is extension in X direction and shortening in Z direction

Fig. 4.3: From PARK, 1983: plane strain
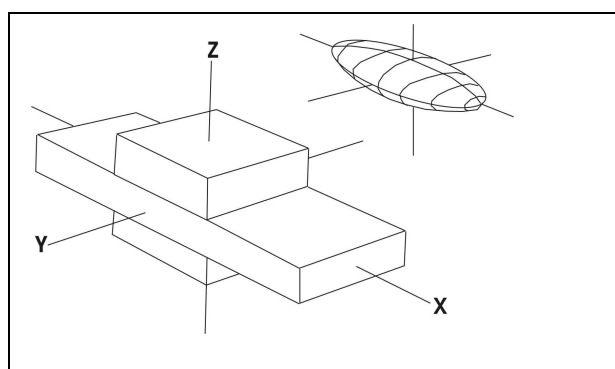
To illustrate the strain symmetry a Flinn diagram is used (FLINN, 1962).

Fig. 4.4: From: PARK, 1983: FLINN diagram (A) for constant volume, the plane strain line forms a diagonal axis (B) In consideration of volume loss the plane strain axis moves into the oblate filed.
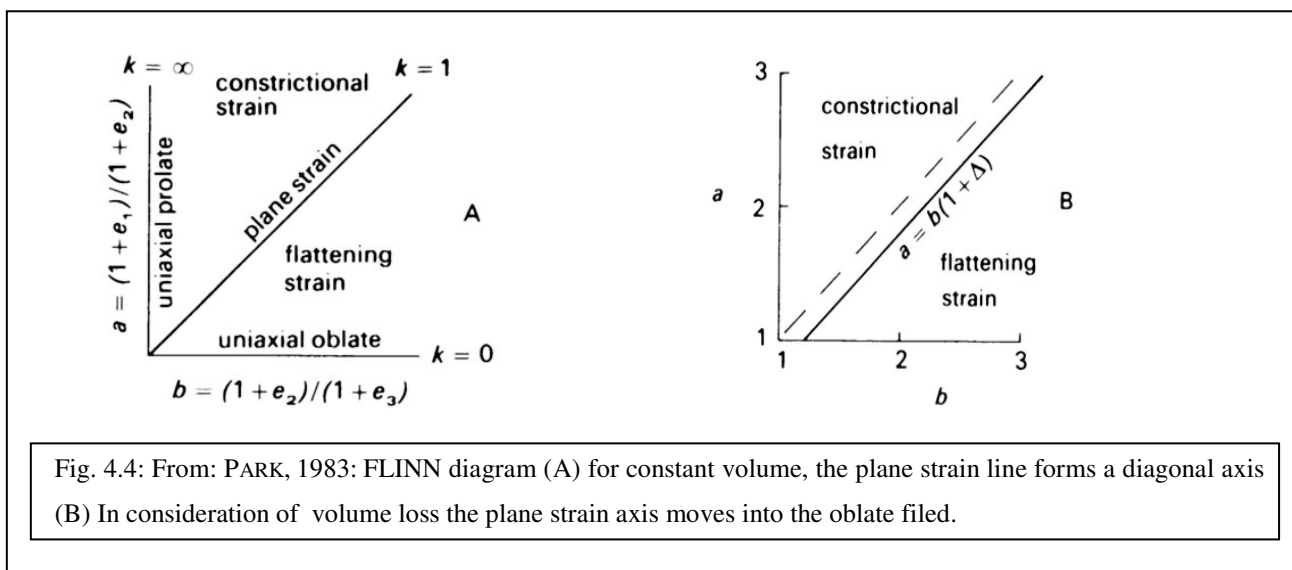
In the two dimensional Cartesian coordinate system of the Flinn diagram the ordinate a and the abscissa b are defined by:

$$a = \frac{S_x}{S_y} \quad \text{and} \quad b = \frac{S_y}{S_z}$$

The different symmetries of the strain ellipsoids are defined by the value k:

$$k = \frac{(a-1)}{(b-1)}$$

If the slope k = 1, it forms a diagonal axis through origin which corresponds with the plane strain axis. For a prolate strain ellipsoid the relationship $1 < k < \infty$ and for an oblate strain ellipsoid $0 < k < 1$ is given (PARK, 1983). If the volume does not stay constant the plane strain line moves into the oblate field. This case is described by the equation: a = b (1+Δ) whereas Δ represents the Volume change.

4.2 Strain type

The strain type is dependent on the volume change S_V. It can be distinguished between constrictional strain ($S_y < 1$), plane strain ($S_y = 1$) and flattening strain ($S_y > 1$).
The volume change S_V is defined by:

$$S_V = S_x * S_y * S_z = \frac{V_f}{V_i}$$

where V_f is the final volume of the deformed object and V_i its initial volume.

To describe the results of the absolute strain measurements, S_V-S_y diagrams are used, which can be fielded in dilatation ($S_V > 1$) and compaction ($S_V < 1$) separated by the isochoric strain line ($S_V = 1$), and constriction($S_y < 1$), and flattening ($S_y > 1$), separated by the plane strain line (BRANDON, 1995).

S_V-S_x diagrams are used to depict the coherency of volume change and extensional deformation with foliation development. It is assumed that the foliation is parallel to the direction of maximum extension X and perpendicular to the direction of maximum contraction Z (BRANDON, 1995). Due to the increase of the deviatoric strain a texture develops; the axial ratio R_{xz} can be used as a measure of the intensity.

R_{xz} is given by:
$$R_{xz} = \frac{S_x}{S_z}$$

The R_{xz} isolines can be projected into the diagrams. The principal axial ratio E_{Rxz} has the relationship $E_{Rxz} = \ln R_{xz} = 2E_x - E_v$ for plane strain with $E_y = 0$. In general it is defined by:

$$E_{Rxz} = 2E_x + 2E_y - E_V$$

E_x, E_y and E_z are the natural principal strains providing a useful basis for constructing a strain-magnitude space. The natural strain E is defined by $E = \ln S$ (BRANDON, 1995). Therefore we obtain $E_x \geq E_y \geq E_z$. In an open system the shortening in Z direction is associated with volume loss ($E_x = E_y = 0$, $E_x = E_v$).

In a closed system there is no volume change. The volume loss in the shortening direction Z is compensated in the extension direction ($E_x = -E_z$, $E_y = E_v = 0$).

4.3 Octahedral shear strain

The conventional octahedral shear strain can be used as a measure of the average distortion a sample suffered and is independent from strain geometry, volume change, strain path and rotational components of the deformation (BRANDON, 1995). So it can be used to compare the measurement results of different methods (e.g. R_f/Φ, PDS, XTG).
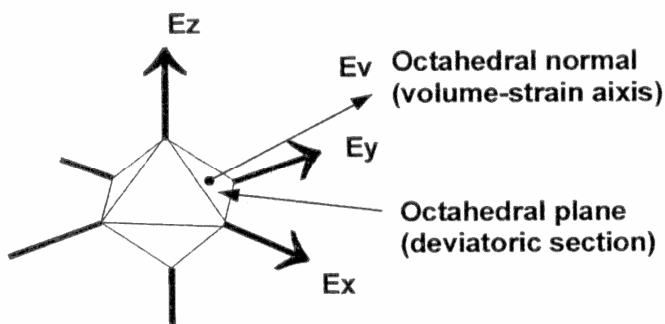
Fig.4.5: Sketch showing the geometry of octahedral plane and octahedral normal with respect to the natural principal strains with E = ln(S).

Assuming simple shear deformation, the shear strain γ along a specific direction can be calculated with the principal axial ratios R (with $R_{xy}=S_x/S_y$; $R_{xz}=S_x/S_z$ and $R_{yz}=S_y/S_z$) in this direction: $\gamma=\sqrt{(R-1)^2/R}$ (RAMSAY, 1967). The maximum possible shear strain recorded in a rock sample is calculated from the maximum axial ratio R_{xz}. The maximum axial ratio R_{xz} can be used as a proxy for cleavage intensity, because in the XZ section, where the shear strains have their maximum, a simple measure of the deviatoric strain is provided. Fundamentally, the total strain magnitude can be decomposed into two orthogonal components (BRANDON, 1995). These are two fundamental scalar measures of volume strain (here described as E_V (natural volume strain) and E_d (natural deviatoric strain)). According to the equation of chapter *4.2: Strain type*, E_V, describing the volume strain, can be given by:

$$E_V = 2E_x - E_{Rxz}$$

In contrast E_d describes the deviatoric strain component and does not refer to the total strain. It can be calculated:

$$E_d = \sqrt{1/3} \bullet \sqrt{(Ex-Ey)^2 + (Ey-Ez)^2 + (Ex-Ez)^2} = \sqrt{E_x'^2 + E_y'^2 + E_z'^2}$$

Whereas in this section here the E_x, E_y and E_z axis are represented by the principal deviatoric strains E_x', E_y' and E_z'.

In principal this can be envisaged as a cylinder with radius r having the volume strain axis in the center, described by the following general equation:

$$r^2 = (x - y)^2 + (y - z)^2 + (x - z)^2$$

Furthermore the β angle indicates a clockwise orientation of E_d in the deviatoric section with respect to the E_{Rxz} axis (Fig. 4.6).

The β angle can be seen as an angular version of the Lode´s parameter v (e.g. HOSSACK, 1968) which is defined by $v = \sqrt{3}\ tan\ \beta$.

Fig. 4.6: (AFTER BRANDON, 1995). Showing the deviatoric section, projectig data parallel to the volume strain axis onto the octahedral plane. $E_x^{'}, E_y^{'}$ and $E_z^{'}$ are the rescaled principal deviatoric strains as projected form of the E_x, E_y and E_z axes, viewed looking down the volume strain axis.
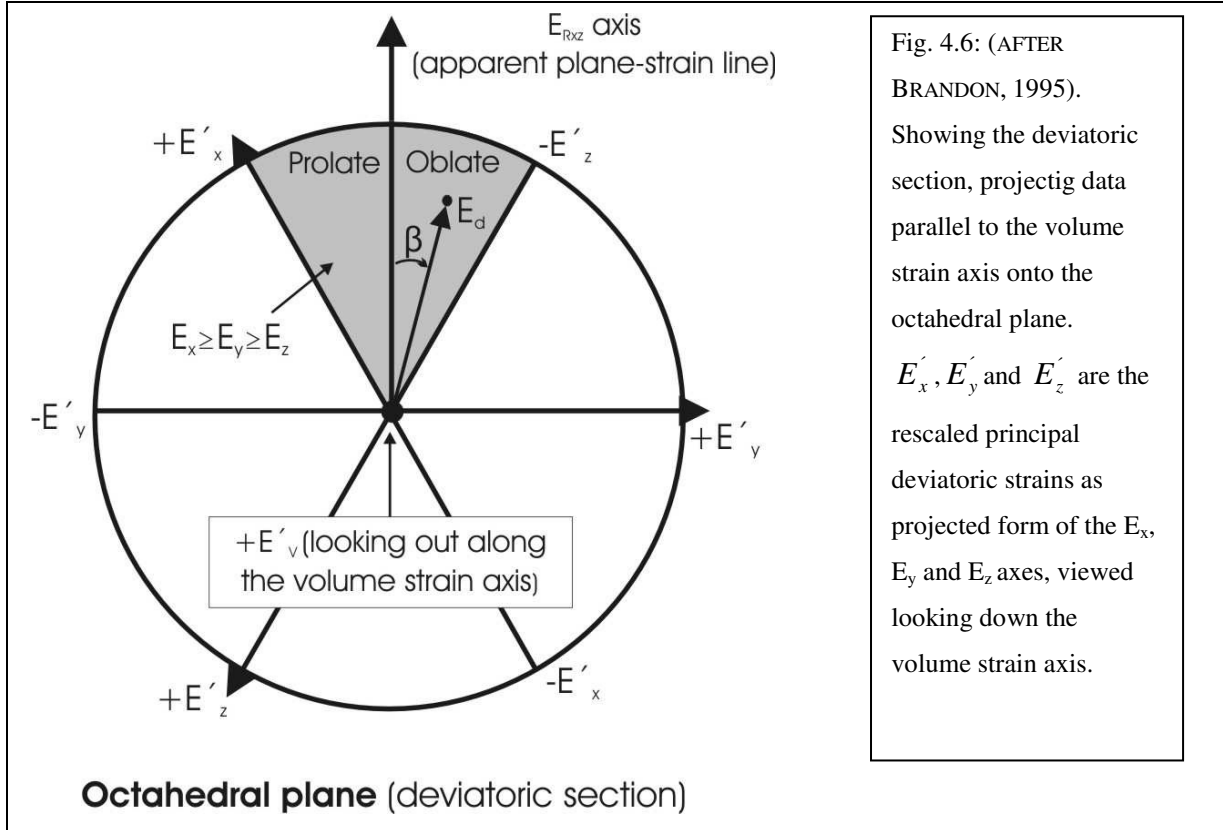
The E_v, E_d and β coordinates of the cylinder of Fig. 4.6 can be specified by the orthogonal axes E_{Rxz}, $E_y^{'}$ and E_v.

Therfore it can be written:

$$E_t\, r = \sqrt{1/2}\ E_{Rxz}\, l + \sqrt{3/2}\ E_y^{'}\, m + E_v\, n$$

and

$$Ed = \sqrt{(1/2)E_{Rxz}^2 + 3/2)E_y^{'2}}$$

whereas E_t is defined as : $E_t = \sqrt{E_d^2 + E_v^2}$ and l, m, n as the basis vectors from the E_{Rxz}, $E_y^{'}$ and E_v coordinate system.

To demonstrate the magnitude of the octahedral shear strain the principal deviatoric strains are sufficient. The general equation for finite shear strain γ (JAEGER & COOK, 1979) can be

considered as function of the initial orientation of a material line, defined by the direction cosines of *l*, *m* and *n*. This leads to the equation :

$$\gamma_{oct} = 2/3 \sqrt{\cosh^2(E_{Rxz}) + \cosh(E_{Rxz})\cosh(3E'_y) - 2}$$

More familiar measures of the deviatoric strain are the axial ratios R_{xy}, R_{yz} and R_{xz} which have following relationships:

$$E_{Rxy} = \ln R_{xy} = \ln(S_x/S_y) = E_x - E_y = E'_x - E'_y$$

$$E_{Ryz} = \ln R_{yz} = \ln(S_y/S_z) = E_y - E_z = E'_y - E'_z$$

$$E_{Rxz} = \ln R_{xz} = \ln(S_x/S_z) = E_x - E_z = E'_x - E'_z$$

The conventional octahedral shear strain γ_{oct} is defined as the amount of shear strain representing the integrated angular distortion experienced by material lines respectively passing through an octahedral normal and an octahedral plane. (NADAI, 1950, BRANDON, 1995). If $\gamma_{oct} = 1$, the final angle between the material line and the material plane that originated at the octahedral normal and octahedral plane, respectively, would be arctan (1) = 45° (Fig. 4.5). The equation for the conventional octahedral shear strain expressed with the axial ratios is given by:

$$\gamma_{oct} = \sqrt{R^2_{xy} + 1/R^2_{xy} + R^2_{yz} + 1/R^2_{yz} + R^2_{xz} + 1R^2_{xz} - 6} \, / 3$$

For details and further information on the calculation and its validity see M.T. Brandon 1995: Analysis of geologic strain data in strain magnitude space, *Journal of Structural Geology*, **17**, 1375-1385.

5. Methods

5.1 Absolute strain measurements

To measure absolute strain in pressure solved sandstones several techniques were used, presented by Brandon et al. (1994 & 1995) and Ring and Brandon (1999). These techniques can only be used for samples which have experienced no internal deformation and are only deformed by SMT (Solution Mass Transfer) deformation. Therefore, they cannot be used for high pressure rocks which have a huge amount of recrystallized material.

In order to determine the principal strain axes (X, Y and Z), volume change, internal rotation and absolute elongation of the components analyses on quartz grains were accomplished. To unravel the extensional and constrictional deformation, the mode method and the PDS (Projected Dimension Strain) method were used. Rotational components were determined by the SDA (Semi Deformable Antitaxial) method.

First the orthogonal principal strain axes X, Y and Z were deciphered. Then maximum, intermediate and minimum stretching directions S_x, S_y and S_z were determined, with $S_x \geq S_y \geq S_z$. In XY thin sections parallel to the foliation the maximum extension axis can be measured and in the perpendicular XZ thin sections the maximum shortening axis can be determined. For the processing of data the "Yale Deformation Programs" (ORIENT, AZIMUTH, MEANDEFM, MICRODIG, PDSCALC and FIBER) were used.

5.1.1. Solution Mass Transfer (SMT) deformation

The SMT- deformation has two processes of fundamental importance, which are pressure solution and solution transfer. Generally pressure solution takes place in areas where the grain boundaries are perpendicular to the shortening direction, i.e. in areas with maximum stress. (PASSCHIER & TROUW, 1996). So originally equant detrital grains, such as quartz, may be almost completely dissolved away and turned into thin platy

Fig. 5.1.: Pressure solution changing the shape of grains. (From: Microtectonics, Passchier and Trouw, 1996).

grains, parallel to and partly defining the foliation (TWISS & MOORES, 1992).The dissolved
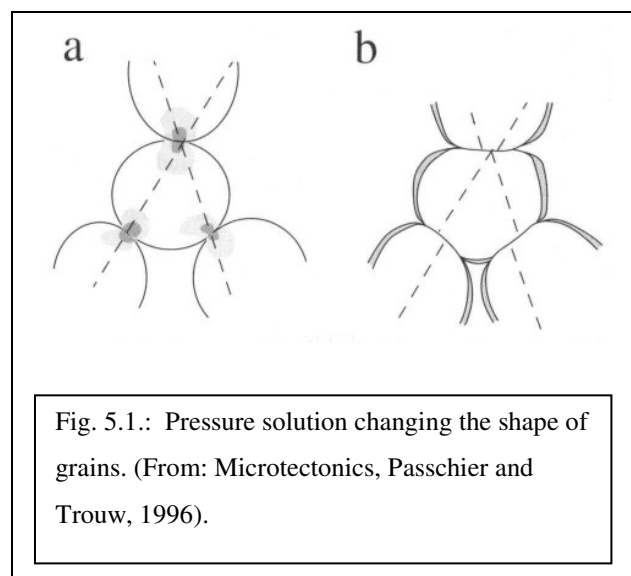
material can either migrate through the rock, e.g. by grain boundary diffusion over short distances, or by transport in a fluid flowing through pores or fractures over large distances (Twiss & Moores, 1992).

The dissolved material in areas of high stress precipitates in areas with lower stress. So grains can change their habitus without intergranular deformation. The reprecipitated material mostly accommodates as subgrains or fibres.

If the fluid transport takes place over larger distances, it accumulates as veins or is leaving the system completely (Passchier & Trouw, 1996, Ramsay & Huber, 1983).

5.1.2 Mode method

The mode method is used to determine the extensional distortion S_x. Therefore, the ratio of grains to fibres was detected in XZ thin sections using a microscope and a point counter. Generally fibre growth can be distinguished in multi -directional and uni-directional growing fibres, whereas multi-directional fibres have a radial alignment and point to all directions in XY sections. They represent a flattening strain type with Y>1. Uni-directional fibres only point in one direction, which is the direction of maximum extension, with Y≤1. The relation between the frequency of fibres m and the maximum stretch S_x is given by the equation:

$$S_x = 1/(1-m)$$

In the first case with multi-directional fibre growth, there would be extension in two directions (X- and Y- direction). It would follow:

$$S_x * S_y = \text{finite area/initial area} = 1/(1-m)$$
$$\text{with } S_x * S_y \text{ as square dimension}$$

5.1.3 The Projected Dimension Strain (PDS) method

The PDS method is used to determine the shortening stretches occurring on grain boundaries because of pressure solution and solution transfer (Ring & Brandon, 1999). Due to SMT deformation the original grain dimension in extension direction can be identified, because it stays constant in X-direction. Fibre growth occurs in the extension direction (X-direction) as well and is mostly parallel to the foliation. Shortening, because of SMT deformation, takes place in Z-direction and sometimes also in Y-direction and normally there is a lack of fibre

growth. These stretches (S<1) can be determined with the PDS method. To receive the average stretch 30-40 grains minimum have to be measured and the shortened diameters are divided by the initial diameter in X-direction. Due to using quartz grains measured in two-dimensional spheres (XY-plane, XZ-plane) there has to be a correction for the calculation of the three dimensional distortion (FEEHAN & BRANDON, 1998).

Using the PDS method the outlines of quartz grains were digitised first, with a Leitz-microscope and a Qtronix digitising board and the program MICRODIG. Afterwards the stretch of the principal strain axes is calculated with the program PDSCALC (Y in XY plane, Z in XZ plane). Undeformed rocks should have an average stretch of 1. Measurements in undeformed Sandstones of the "Great Valley Sequence" in California prove this assumption (RING & BRANDON, 1999).

5.1.4 Semi Deformable Antitaxial (SDA) method

The SDA method determines the internal rotation due to SMT deformation. Normally either the "rigid-fibre method" (DURNEY & RAMSAY, 1973; RAMSAY & HUBER, 1983) or the "deformable-fibre method" (RAMSAY & HUBER, 1983; ELLIS, 1986) are used for strain analyses of syntectonically grown fibres. But none of them reflects to the structural and textural circumstances of the thin sections. Therefore, the simulation program FIBER (BRANDON, 1994) was used to estimate deformation parameters from digitised antitaxial fibres.

In order to use the "rigid-fibre method", fibres must be deformed by translation and rotation processes relatively to the grain boundary, but not internal. Grains and fibres show a rigid behaviour. In contrast, when fibres deform after an initial growth like the wall rock the "deformable-fibre method" is used. In this case the deformation path would have to be reconstructed backwards to get information about deformation history, extensional stretching and rotational components.

The program FIBER is based on simulation processes and an inverse logarithm. Fibre growth is simulated on a circular area which depicts the centre of an average three dimensional grain. Finite deformation is determined by the integration of a velocity gradient tensor. With this, the general three dimensional deformation, including rotational components can be described. The FIBER program calculates the internal rotation using a non linear logarithm of the smallest sum of square, based on the Simplex method (Amoeba routine of Press et al., 1992,

P. 402) to search for the best fit solution. For the calculation there should be minimum 30-40 fibres digitised and the modal frequency of fibres, the average orientation of the foliation and the constrictional principal stretches (determined by the PDS method) are needed. Furthermore, it is necessary to make sure that the maximum stretch S_x is greater than 1.1 which is corresponding with an amount of 10% fibres. The measurements for the internal rotation were made on XZ planes.

As a measure for the internal rotation the average kinematic vorticity numbers (PASSCHIER & TROUW, 1996) are calculated with the FIBER program. The kinematic vorticity number Wk is a measure of the rotational quality of a flow type and is given by the internal rotation in relation to the absolute stretching rate. For coaxial progressive deformation Wk = 0 (pure shear). For non- coaxial deformation Wk = 1 (simple shear). The kinematic dilatancy number Ak is a measure of the rate at which a surface shrinks or expands with time. So it is defined by the Volume change in relation to the stretching rate (PASSCHIER, 1991). The modified kinematic vorticity number Wk* gives the relation between internal rotation and deviatoric stretching rate whereas Ak* is defined as the relation from the Volume change rate to the deviatoric stretching rate (RING & BRANDON, 1999).

The kinematic vorticity numbers are dimensionless numbers and normalised for strain rate. As an outcome of the numeric calculation of Wk, Wk* and Ak* an average velocity gradient tensor is generated, which gives the three dimensional finite strain and the internal rotation after integration.

5.2 Relative strain measurements

In HP rocks SMT deformation is not the only form of deformation. Rocks are characterized by intracrystalline deformation and recrystallisation processes. Due to this the proportion of the maximum stretching axis X does not necessarily reflect the original amplitude.

Therefore in these rocks the deformation can only measured relatively and not absolutely.

5.2.1 Rf/Φ analysis

With the Rf/Φ method (RAMSAY & HUBER, 1983) deviatoric strain data were obtained by measuring deformed quartz grains in thin sections of both series. In order to quantify the deformation they suffered, the elliptical shape (final elipticity Rf) and the angular orientation Φ of the deformed grains was determined. A least-squares best-fit ellipse was calculated for each marker outline, as well as its relative position and orientation, using the program RFPHISM

(written by M.T. Brandon: http://www.geology.yale.edu/~brandon/Software/YALEDEFM),

which was based on a method of Shimamoto & Ikeda (1976). The two major assumptions were that the analysed objects were initially ellipsoidal in shape and randomly orientated and that they were strained homogenously with their matrix.

Fig. 5.2.: Strain ellipsoid refering to the Rf/Φ method
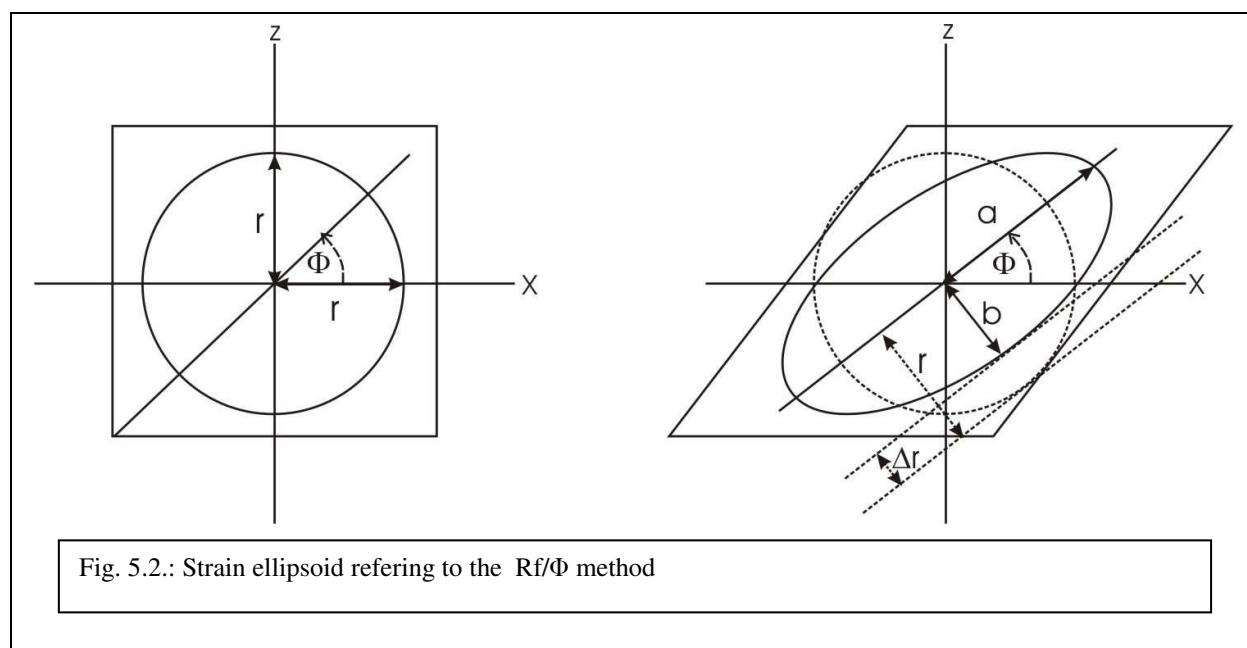
At constant volume the radius r can be expressed by: $r = \sqrt{ab}$. Due to being not sure if the deformation was at constant volume only the ratios of the maximum and minimum stretches can be determined. R is the axial ratio of an ellipse and it is defined by:

$$R = \frac{a/r}{b/r} = \frac{a}{b}$$

R does not involve the original length r, because it is unknown. In general an ellipse can be defined by the matrix:

$$[x \quad y]\begin{bmatrix} f & h \\ h & g \end{bmatrix}\begin{bmatrix} x \\ y \end{bmatrix} = 1$$

with the equations:

$$g = \frac{1}{R}\sin^2\Phi + R\cos^2\Phi$$

$$f = \frac{1}{R}\cos^2\Phi + R\sin^2\Phi$$

and

$$h = \left(\frac{1}{R} - R\right)\cos\Phi\sin\Phi \quad (\text{FRANKLIN, 1968}).$$

With these relationships the angular orientation of the deformed object can be determined by the equation: $\tan 2\Phi = \dfrac{2h}{f - g}$.

Tectonic strains were deduced from the χ^2 minima of the Rf/Φ analysis (PEACH AND LISLE, 1979). The 2D strain estimates (XY and XZ thin sections) were used to calculate the finite-strain ellipsoid according to the modified least-squares technique of Owens, 1984.

5.2.3 X-ray texture goniometry (XTG)

To avoid measuring strain partitioning effects additional XTG measurements on phyllosilicate- rich rocks have been performed. The 3D preferred orientations of phyllosilicate grains (001-planes of chlorite and muscovite) were measured with a reflection X-ray goniometer with Cu-α source and an impressed voltage of 40 kV and 30 mA. To improve grain statistics, a sample translation of +- 5 mm perpendicular to the principal goniometer axes was applied, leading to an irradiated sample area of about 100 mm^2. Because of the high amount of phyllosilicates, this technique is ideal for looking at strains in pelitic rocks. Furthermore, even SMT deformation does not affect the availability of the phyllosilicates as strain markers, as long as the solved material is precipitated as crystallographically continuous overgrowth on pre-existing grains (OERTEL, 1983). The intensity of reflected X-rays on lattice planes of a large number of grains was measured. The theoretical background for these measurements is given by implications of the Bragg-equation:

Fig. 5.3: Principles of the Bragg equation after Kleber et al. 1990, with the refraction angle Θ, and the space – lattice distance d. With azimuthally varied sample orientations, the orientation of the lattice planes of a sample can be determined and the intensity of the reflected X-ray beam can be measured.

$$n * \lambda = 2d * \sin \Theta$$

with the wavelength λ, the refraction angle Θ and the space lattice distance d. To get a relative measure of the alignment of the observed minerals, the diffractometer is first set to the correct refraction angle of the analysed mineral planes. Intensities are measured for different sample orientations with respect to the incoming X-ray beam. While the diffraction angle was held fixed the sample stage was successively tilted over 5° steps. At each tilt position single intensities were measured over an azimuthal range of 360° with 15° intervals. To keep

Fig. 5.4: Schematic sketch of the arrangement of the x-ray texture goniometer.
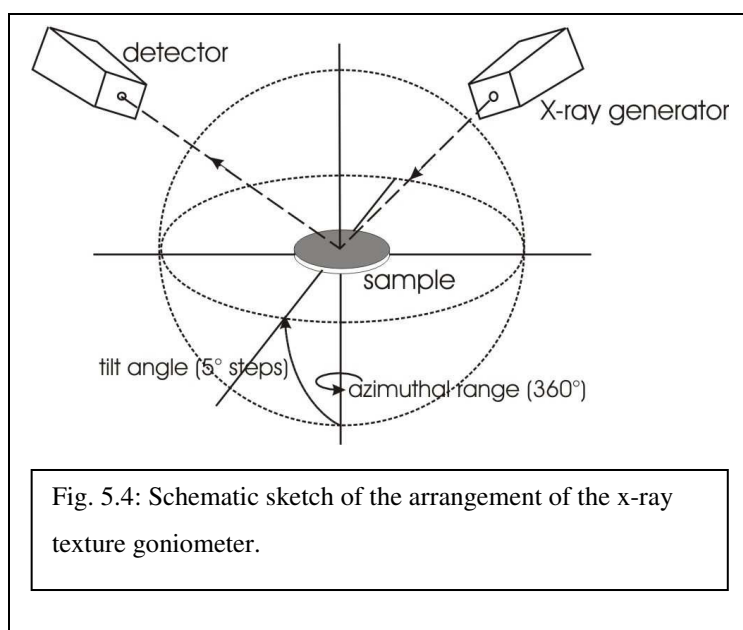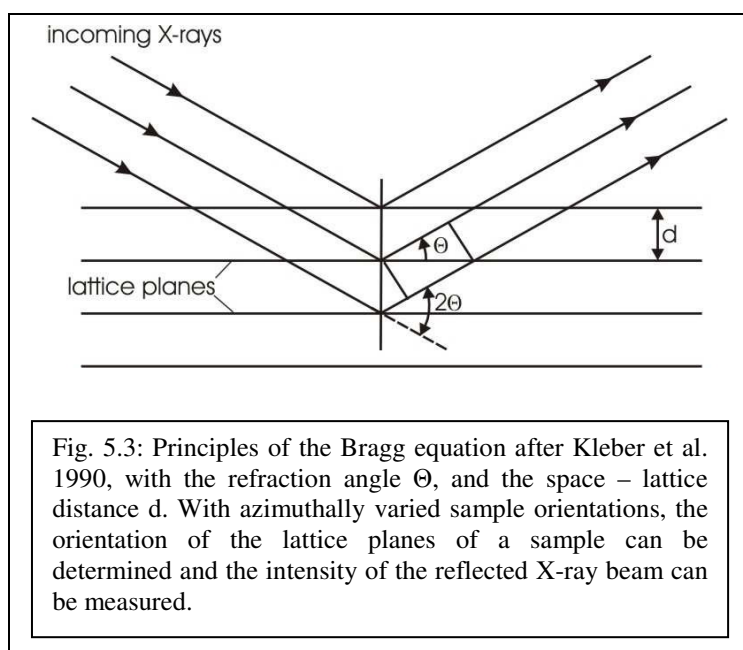
defocusing effects of the X-ray beam as small as possible, values were cut off at a maximum tilt angle of 40°.

March Strains

March (1932) showed that there is a relationship between orientation and strain. It is based on the observance that there is a unique distribution of grain orientation for every specific strain. It is given by the equation:

$$S'_i = \rho_i{}^{-1/3}$$

where S'_i is the principal deviatoric strain and ρ_i is the principal pole density of the lattice planes in a certain direction, divided by the average pole density of all orientations. Moreover the March model provides an approximation of the deformation history of the rock volume and coaxial strain increments (Oertel, 1983). Because the XTG method does not measure single plane orientations, the pole densities in March´s equation are replaced by reflection intensities:

$$S'_i = (i_{net}/i_{unif})^{-1/3}$$

with i_{net} as the intensity in a certain measured sample position and i_{unif} as the uniform intensity of all positions (OERTEL, 1983).

For calculating the principal stretches S_x, S_y and S_z and the principal axial ratios R_{xz}, R_{xy} and R_{yz} from the measured intensities, the XTGFIT program (by M. T. Brandon) was used. This program uses a best-fit least-squares algorithm based on a routine by Press et al. (1986). It iterates through a series of assumptions in order to find the quadratic coefficients for the XTG data that have consistency with the observed measurements.

5.3 Digital image processing (Radius method)

With the digital image processing method the complete amount of quartz in a thin section is determined and compared to the amount of quartz in veins of a thin section. The method uses differences in colour spectra to separate quartz from other components. To detect quartz, the thin sections were scanned under an automatic polarization microscope using the Radius (rapid particle analysis of digital images by ultra-high-resolution scanning of thin sections) method (SEELOS & SIROCKO, 2005). For counting and measuring the particles the image-processing Software AnalySIS has been used.

In a first step the colour thresholds of quartz has to be defined. Every colour spectrum is composed by a red, a blue and a green component as well as 255 greyscales. As end-members a grain orientated in extinction direction and a grain orientated at a 90° angle to this, which has the maximum brightness, are used. The thresholds have to be defined separately for both cases. All other orientated grains have intermediate spectrums between those two end-members. In this study the colour threshold setting for quartz is light yellow up to white. For grains orientated in extinction direction the colour threshold is light- to dark brown.
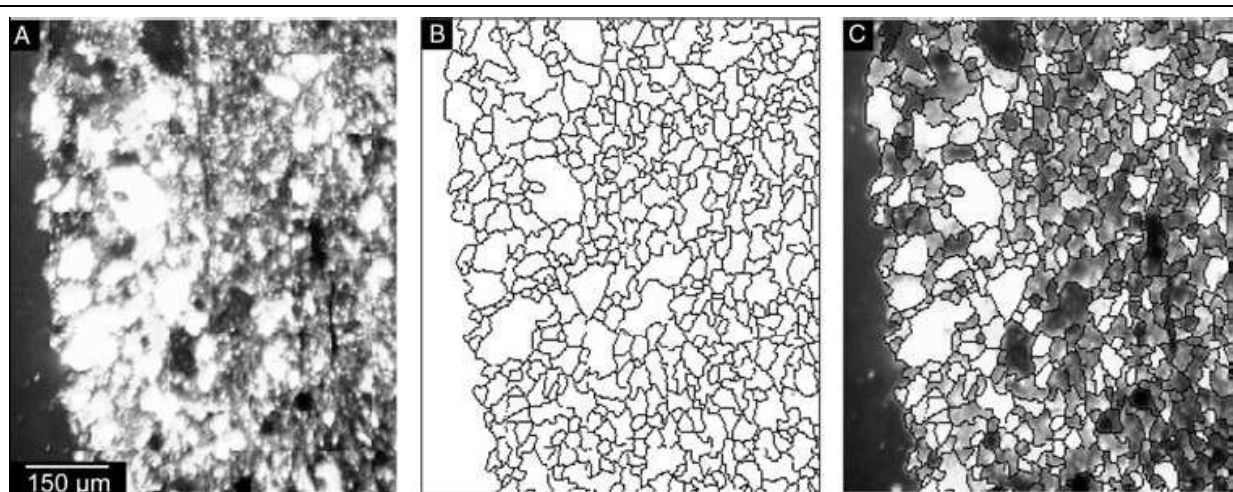
Fig. 5.5: The watershed algorithm identifies the edges of particles on a monochrome image (A) and transfers them into a binary filter matrix (B). As a result a combined picture can be generated (C). On the basis of defined colour thresholds, for every single grain it can be determined whether it is quartz or not. (From Seelos & Sirocko, 2005).

In a second step the amount of quartz can be detected by adding up the grain sizes of single quartz grains. The grains are specified with the Equivalent circle diameter (ECD) in µm². Thin sections are scanned stepwise on a fully automatic polarization microscope (Zeiss Ortoplan, Carl Zeiss AG, Göttingen, Germany) combined with a digital microscope camera (SiS Colorview II, Soft Imaging Systems GmbH, Stuttgart, Germany). The scans are made under polarized transmitted light and a magnification of 25×. All adjustment parameters for the microscope table (Märzhäuser) and the digital camera are controlled by the software AnalySIS.

Colour detection of particles (RADIUS-2):

The image-processing software AnalySIS offers the possibility to separate single grains by using a so-called 'watershed algorithm' (AnalySIS Ref.-Handbuch, 1999). The recognition of particle edges is based on two facts: the inner edges of two adjacent grains show minimal changes in colour, and the outer edge is characterized by small indentations. The watershed algorithm assigns these colour anomalies and connects them with the indentations on the outer edge of the two adjacent particles. Other modules of AnalySIS include detection settings like lower and upper pixel boundary, which demarcate the counting range.

Fig. 5.6: (A) Thin section with quartz under polarized ligt. (B) Region of interest (ROI) defined manually within the section.
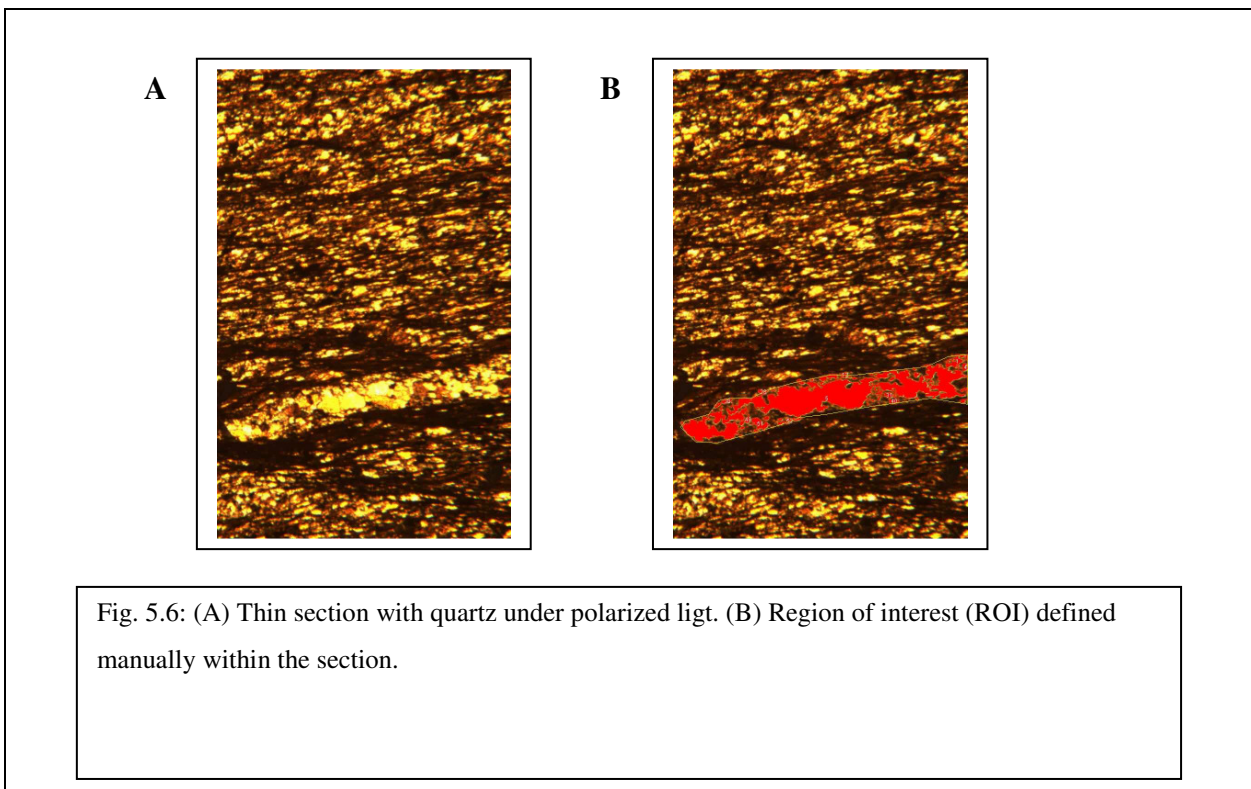
The implemented RADIUS-1 routines are controlled by programmable macros, which allow a nearly complete automation of scanning processes (SEELOS, 2004). The scanning procedure consists of 40 single-image records. The overlapping of two adjacent edges is adjusted or automatically by AnalySIS. Utilizing these settings, the application calculates the number of single pictures for a complete thin-section record.

The user can also define regions of interest (ROIs). In this study two types of ROIs were distinguished: The thin section as a whole and the regions consisting of quartz veins. To prevent an imbalance between the length of a sample and the maximum particle sizes, the following measurement method was implemented into RADIUS-2: every grain is measured regardless of sampling intervals in its maximum dimension. The first appearance of a particle is recognized by the program and assigned to the dedicated sample segment, independent of its diameter (SEELOS & SIROCKO, 2005). A classification sub-module allows the definition of particle classes (grains orientated in extinction direction and grains orientated 90° to this) for every ROI based on the results above.

After running the RADIUS-2 particle detection, a data set which includes the following particle parameters for each ROI is obtained:

1. Absolute number of counted particles per class.

2. Percentage of particle areas on ROI area per class.

3. Mean ECD per class.

4. Mean form factor per class (non-dimensional).

5. Mean elongation per class (non-dimensional)

The digital image processing method is used to estimate the ratio of dissolved quartz in single grains and the amount of SiO_2 which is accumulated in quartz veins (on thin section scale). With the PDS method an average volume loss was calculated. It is of interest, whether this material is transported over longer distances and is concentrated in bigger veins, or if the material accumulates near to where it was diossolved and generates smaller veins on the μm scale.

In order to obtain a three dimensional impression, thin sections in XY and XZ directions are used. With this parameters (amount of the whole quartz, average amount of solved material and amount of quartz material in the veins) a mass balance can be calculated.

6. Parameters for mass balance

From the PDS measurements on quartz grains an average volume loss can be calculated (Chapter: 5.1.3). It is of fundamental interest, whether the dissolved material was transported out of the wedge, which would reflect an open system, or whether it stayed within the wedge, which would reflect a close system. Generally advective solution transfer involves open system transport of material by the physical motion of the solution and is controlled by hydraulic gradients (e.g. RUMBLE ET AL., 1982, ETHERIDGE ET AL., 1983, COX ET AL., 1987). Diffusional solution transfer involves closed system transport of locally derived material through an essentially static solution, controlled by chemical potential between source and sink (e.g. BACH, 1974, KERRICH ET AL., 1978, RAMSAY, 1980).

However, the scale on which volume loss occurs is of significant importance, because volume loss is scale dependent (COX, 1993). There must always be some correspondingly bigger volume in which mass is conserved, unless the principle that mass can neither be created nor destroyed is wrong (COX, 1993). Main questions are: What constitutes an open – and a closed system? And how far is material transported?

It has been observed in thin sections and in the field that quartz veins and quartz rods are very prominent which might be a consequence of local reprecipitation of dissolved quartz.

In chapter 11 an approximation of the material flow in the Chilean wedge is presented. This has been appraised by the correlation of the volume of solved material in the quartz grains and the volume precipitated in quartz veins.

As background for this mass balance the ratio of the whole amount of solved SiO_2 to the amount of SiO_2 in quartz veins is calculated. To develop a three dimensional image of the veins the proportion of quartz and other, non quarzitic material has been determined in two dimensional slices in two directions (XY-direction and XZ-direction). Therefrom it is possible to estimate a three dimensional volume for the quartz veins.

In the two dimensional space (independent of the scale) the amount of quartz as a whole has to be detected.

The equation:
$$A_{qz} = A_{ent.} - A_{ocomp.} \qquad (I)$$

With: A_{qz} = Amount of quartz ,
$A_{ent.}$ = Entire amount of components in the observed space and
$A_{ocomp.}$ = all non quartz components

describes the amount of quartz in a two dimensional space.

For further calculations the values are standardized to 100% of quartz as a whole. Afterwards the percental amount of quartz in the veins can be determined with the equation:

$$A_{qzv} = A_{qz} - A_{qznv} \qquad (II)$$

With: A_{qz} =Amount of quartz ,

         $A_{qzv.}$ =Quartz bound in veins

         A_{qznv} =all single quartz grains not bound in a vein.

If there are any other components in the veins than recrystallized, their amount has to be determined and subtracted from the amount of the vein.

To estimate the flux of solved SiO_2, the scale for the observations has to be defined. For this approximation three different scales have been chosen. The first one is the thin section scale and includes quartz veins up to 1mm in width. The second one is on the scale of a rock sample including veins of 1mm – 2cm scale. The third scale is an outcrop and here all veins with more than 2cm width (up to veins with several dm width) are described. For the determination on thin section scale the RADIUS program has been used (see chapter: 5.3). In XY and XZ thin sections the total amount of quartz and the amount of quartz in veins has been determined via colour spectrum detection.

Fig. 6.1.: Part of a thin section with quartz vein. (a) shows the thin section under polarized microscope. (b) shows the detected quartz grains with red and brown colours in the section. (c) shows the recrystallized quartz within defined grain boundaries (blue lines).
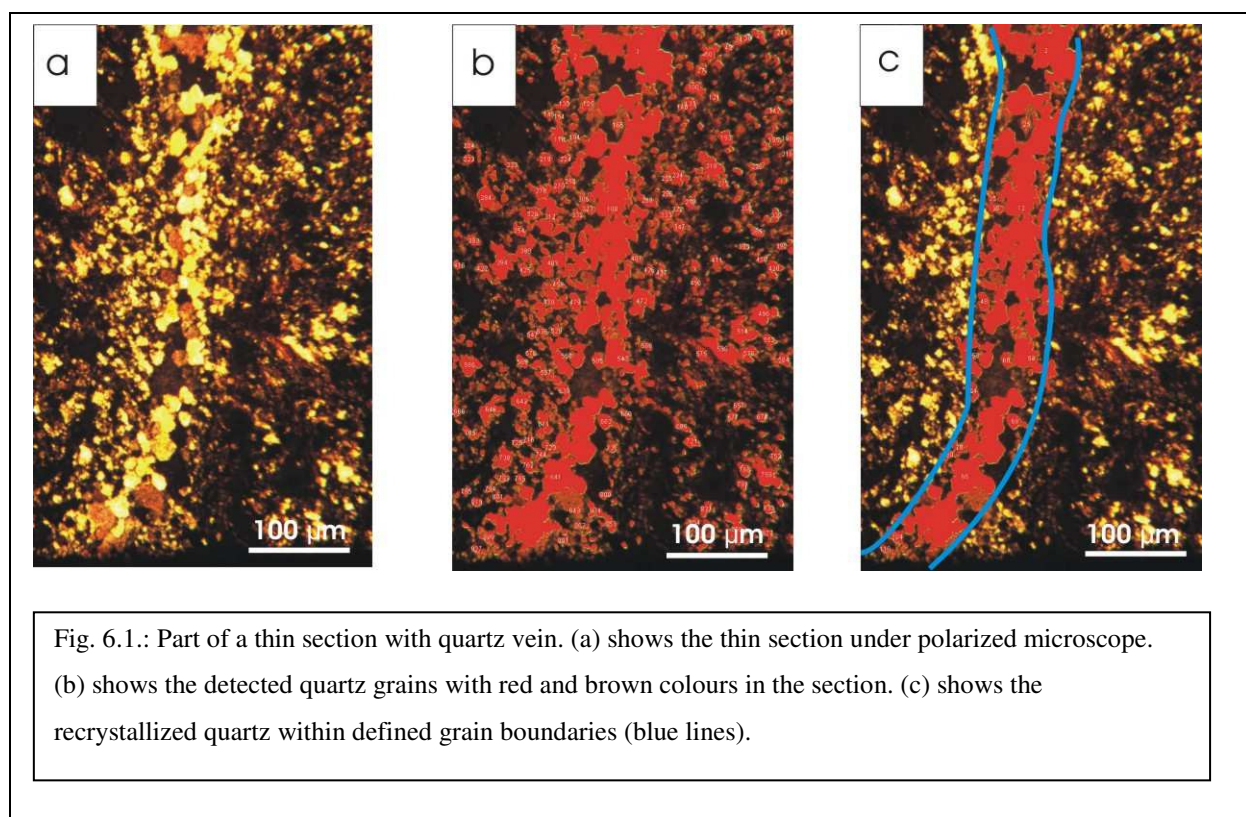
One difficulty is that RADIUS does not define the borders of a vein automatically, so that the contacts to the wall rock have to be defined manually (blue lines in Fig. 6.1.c). It is important to assess the same criterions for the contacts of the recrystallized quartz to the surrounding material, to make sure that a self contained pattern can be created and the error caused by varying measures stays rather small.

Fig. 6.2: Quartz vein in Sample 93 in XZ direction, overlain by a 1cm² grid to detect the amount of the vein in contrast to the whole sample in two dimensional space.
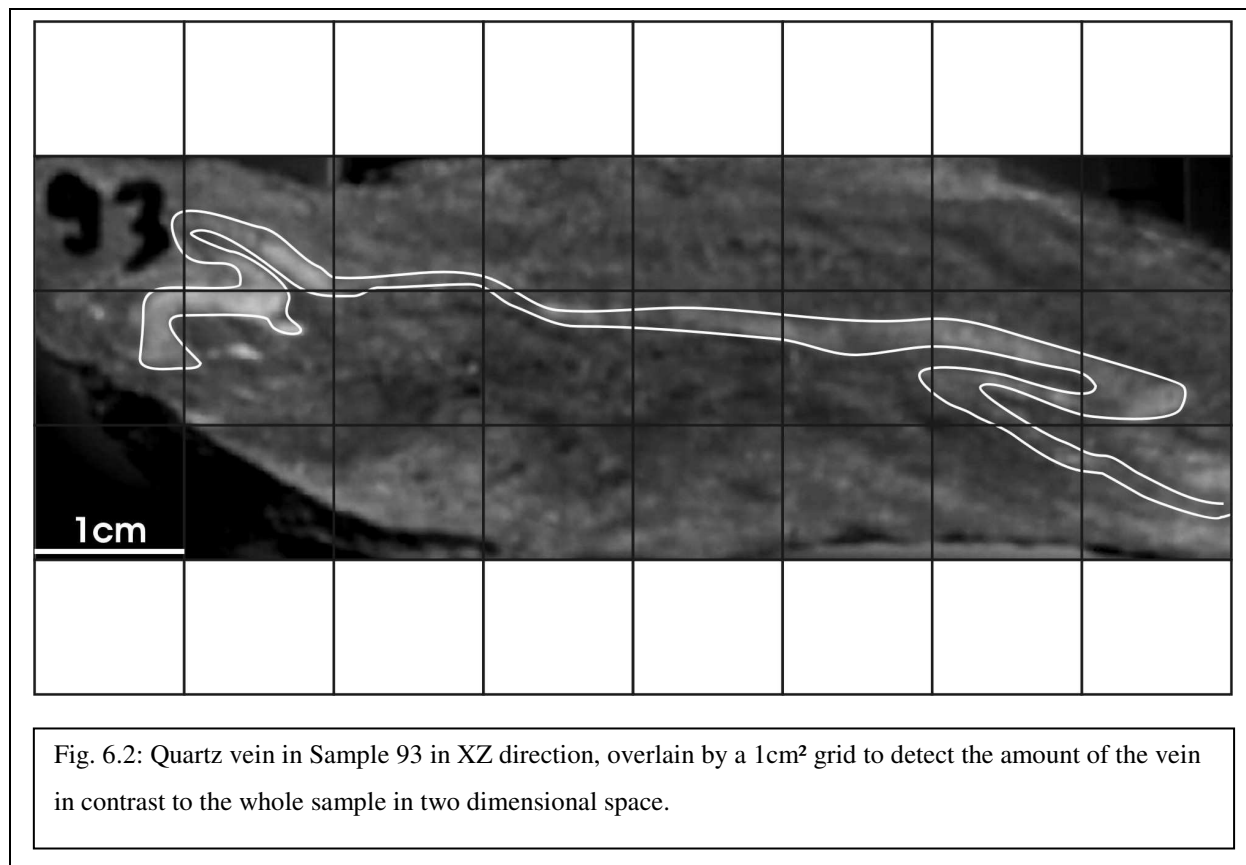
On the next larger scale, the principles for the measurements remain the same, which means that equation I and II are also used for the calculations. In contrast to the thin section scale, the samples cannot be detected automatically, but have to be measured with a grid which is overlain over the sample. The ratio between quartz grains and other non quarzitic material is already known from the thin section analyses. For the approximation a grid of 1cm² has been chosen, because it is adapted best for the veins which should be detected (<2cm).

With detections on slices of two different directions (XY and XZ) in the same sample, it is possible to interpolate the three dimensional volume of the veins. In contrast to the first two cases, this is only rarely possible on larger scales, because larger veins in field are often only viewable from one direction. So it is in most cases not possible to interpolate a three dimensional image, which enlarges the error of the approximation in these cases.

7. Structural data

To get a detailed, representative overview of structures in the Coastal Cordillera of Central Chile, in this chapter the structural data of the study area are described separately for the three areas Rio Maule, Pichilemu and Los Vilos:

7.1 Structures in the Rio Maule area

The area along the Rio Maule transect represents a nearly undisturbed sequence of the ancient accretionary wedge. Therefore, structural data are presented here, in order to unravel whether the contact between Eastern and Western Series is of transitional or of tectonic nature. Structurally the transect shows a continuous evolution from the easternmost part, which is characterized by upright folding of sedimentary bedding, to the westernmost part, where a pronounced subhorizontal transposition foliation is dominant (Fig.7.1.). East of Forel, sedimentary bedding S_0 is well preserved and includes structures like load casts and graded, convolute and cross bedding. As shown in the cross section S_0 is deformed by open to tight, generally upright F_1 chevron folds at 10m to 100m scale. The axes trend NNW-SSE and dip shallowly either to the south or to the north. Near to the Late Paleozoic batholith the F_1 axial planes are slightly overturned to the east. This structural pattern changes near Pichaman, where F_1 is overturned to the west. The steeply dipping axial plane foliation S_1 represents the dominant structure in the whole eastern section.

About 500 m east of Forel S_1 and F_1 are homoaxially refolded by open recumbent F_2 folds on the metre scale. The F_2 folds have subhorizontal east-dipping axial planes and are associated with a likewise east-dipping S_2 foliation. Further west the F_2 folds become progressively tighter and the F_2 axial planes and S_2 are rotated by and by into a shallowly east dipping position. On the closely spaced S_2 planes, west of Forel, a WNW trending stretching lineation L_2 is well developed (Fig. 7.9). Coevally, between Forel and Maquehua, quartz veining becomes more prominent. The first generation of these veins is tightly to isoclinally folded about F_2 axes. S-C relationships and asymmetric clasts indicate a top WNW sense of shear, which is compatible with the consistent westward vergence of F_2. Due to this S_2 parallel shear, F_2 fold hinges are sheared out and result in rootless F_2 folds.
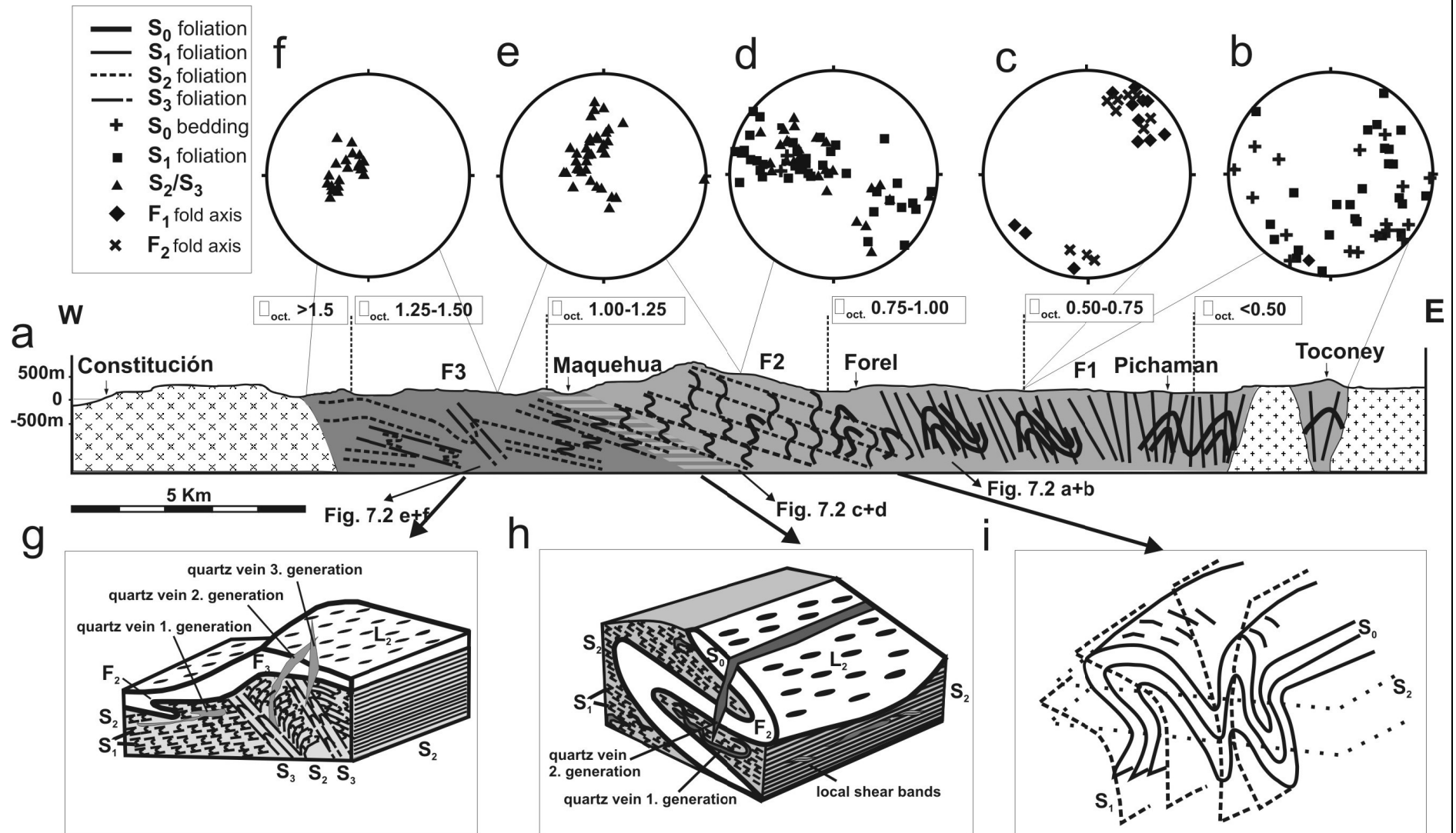
Fig. 7.1 from PETER P. RICHTER, UWE RING, ARNE P. WILLNER & BERND LEISS: Structural contacts in subduction complexes and their tectonic significance: The Late Paleozoic coastal accretionary wedge of central Chile, 2007: (a) Progressive structural development along Rio Maule transect showing the evolution from upright folding of S_0 between Toconey and Pichaman o a pervasive transposition foliation in the west. The conventional octahedral shear strain, γ_{oct}, which is a measure for the strain magnitude, increases to the west. (b-f) Stereograms showing orientational data for the different structures. (g-i) Sketches showing the structural development in detail. Localities from where photographs in Fig.7.1 were taken are also indicated
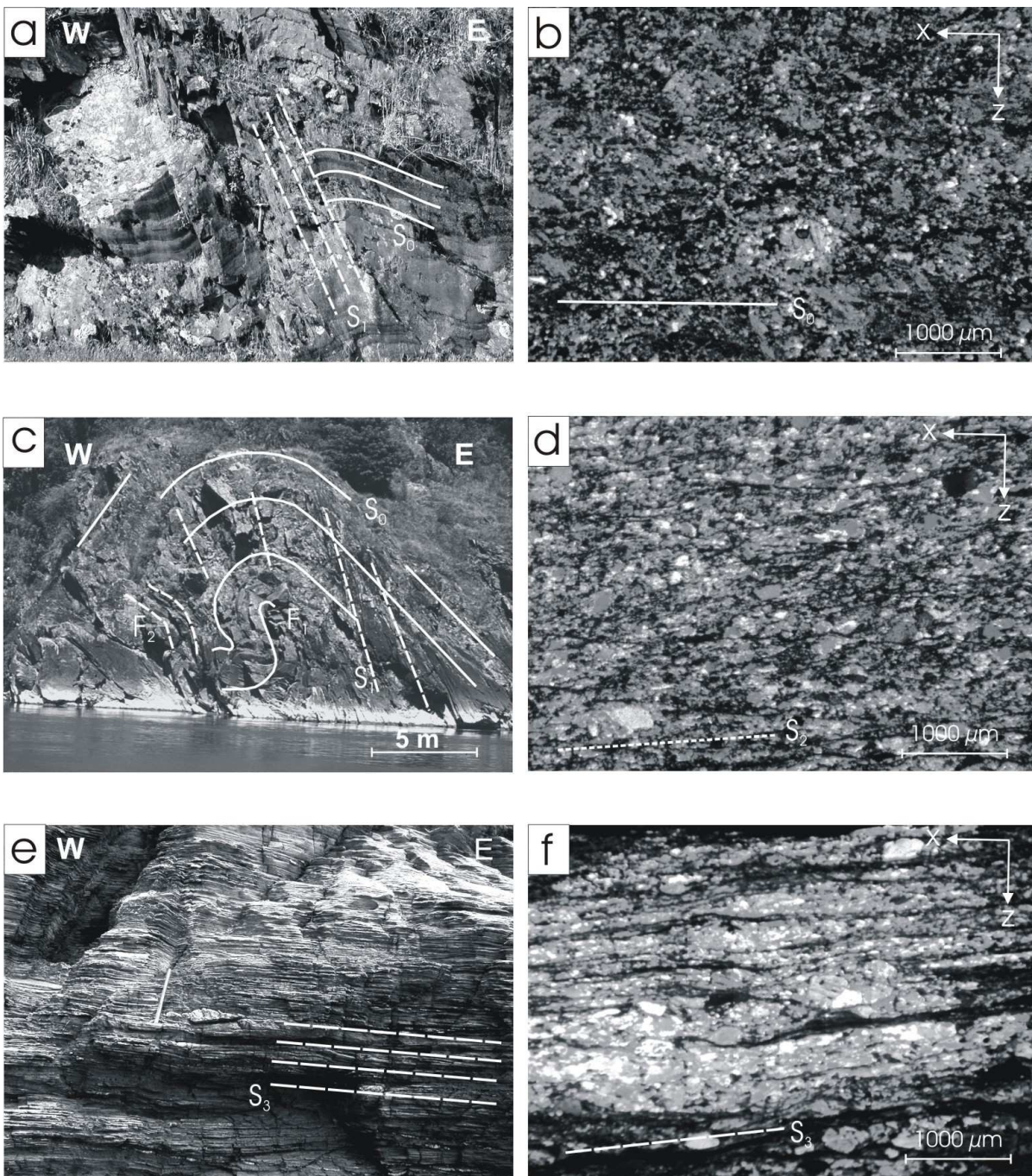
Fig. 7.2: Field and thin section photographs from the Rio Maule transect illustrating increasing deformation from east to west (for locations refer to Fig. 7.1.1). (a) Folding of S_0 and development of associated S_1 in the hinge of a F_1 fold. (b) Thin section from this locality depicts a weak preferred orientation of the minerals (c) Folding of S_1 about west-vergent F_2 fold. (d) Microphotograph shows flattened quartz grains and aligned micas forming spaced S_2 foliation. (e) Pervasive transposition foliation with isoclinal intrafolial folds. (f) Thin-section photographs shows strongly preferred orientation of white mica and chlorite.

Further west, S_2 is progressively folded about F_3 folds in highly deformed domains. They have NW- SE trending axes and subhorizontal axial planes and reach maximum sizes of m scale, but mostly stay rather small on dm scale. The F_3 folds are associated with the development of a S_3 foliation which may dominate locally. The supposed contact between Eastern and Western Series is situated near Maqehua, where the extreme narrowly spaced S_2 planes in the metapelites dominate. In the metapsammites S_1 is occasionally preserved and S_0 can be inferred from metapsammite - metapelite alternations (Fig.7.2, pics.(a) & (b)).

The S_3 foliation, produced by the folding of S_2 by F_3 folds, rotates into S_2 parallel position and causes a penetrative S_2/S_3 transposition foliation. As well, an omnipresent WNW trending stretching lineation $L_{2/3}$ becomes prominent. It is characterized by elongated quartz grains and quartz rodding and has a subparallel position to F_2 fold axes. Post D_2 quartz veins are folded by F_3 folds. Near Maquehua quartz veins are isoclinally folded with axes trending subparallel to $L_{2/3}$; locally these folds are refolded about similarly orientated axes. This new folding produces a new crenulation cleavage, which rotates into the S_2/S_3 transposition foliation, developing S > L tectonites. Quartz boudins, asymmetric folds and shear bands yield a consistent WNW shear sense. Kinematic indicators associated with $L_{2/3}$ at the coast south of Constitución show alternating top to the WNW and top to the ESE shear senses (Fig.7.9).

The shear bands show an evolution of early formed ductile shear bands (10-15° angles to the penetrative foliation) to brittle-ductile shear bands(30-35° angles to the penetrative foliation) finally to brittle normal faults. Late quartz filled tension gashes cut all older structures.

In conclusion the structural development along the Rio Maule transect shows smooth and gradual changes in the style of deformation and therefore represents a continuous structural section.

7.2. Structures in the Pichilemu area

North of Constitución, structures of the Pichilemu area were investigated in order to find out where are similarities and where are differences to the Rio Maule transect.

Fig.7.4 shows a Block diagram of a schematic cross section in the Pichilemu area. Structures here again are characterized by large scale, upright S_0, S_1 folds in the east and subhorizontal small scale, tight to isoclinal folds in the west.

Generally the sequence of structures from the Constitución area can here be traced as well, because all fold structures (F_1-F_3) appear here as well.

The transposition foliation in the southern part of the Pichilemu area is predominantly subhorizontal (Fig. 7.3). But the orientation of the transposition foliation also reveals some differences to the Constitución area, because in the northern part it is partly folded by postaccretionary large scale folds and rotated into a steep, almost subvertical, position. This folding has also been recognised by Martin et al. (1999) at 40° S and was related to an episode of post-Permian transpression.

Between Pichilemu and Lago Vichuquén this area is characterized by the Pichilemu-Vichuquén fault. In the vicinity of the fault structures are slightly steepened and rotated into a subvertical position. The lateral offset is probably rather huge and it can be observed that the fault does not necessarily cut off the octahedral shear strain contour lines, but displaces them against each other. In the case of Fig. 8.4, two, γ_{oct} sections with the same values are juxtaposed against each other. Fig. 7.4 shows that the Pichilemu-Vichuquén fault has a slight vertical and a larger transversal offset.
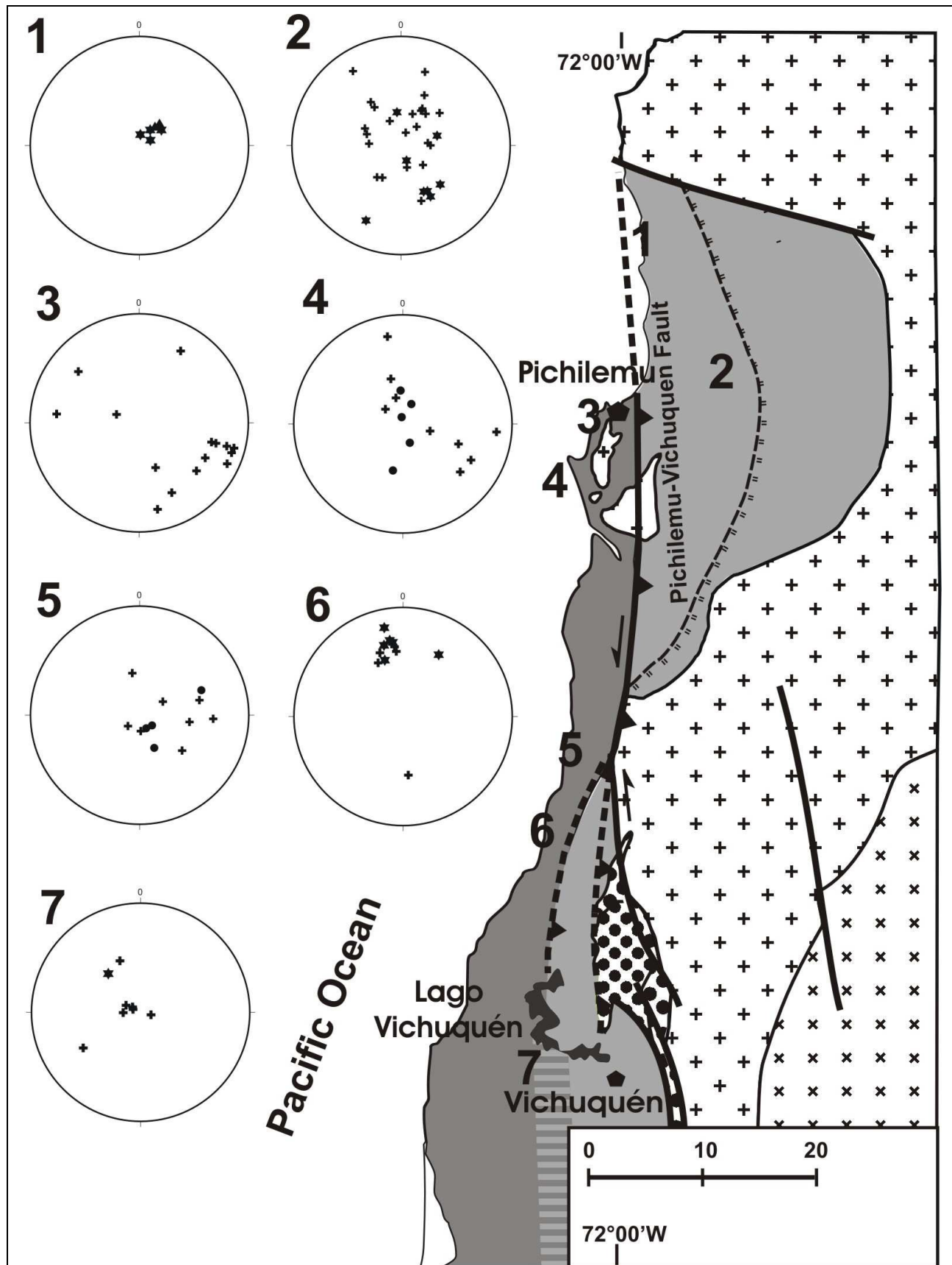
Fig.7.3: Map showing structures between Pichilemu and the Lago Vichuquén (S1 (asterisks), S2 (crosses) and S3 (dots)). Most planes are lying rather flat, except at localities 3 and 6 where the stereoplots show steep orientations.

Fig. 7.4: Schematic cross section between Pichilemu and the Lago Vichiquén. The Pichilemu-Vichuquen Fault appears at the contact of Eastern and Western series and steepenes the structures related to the late paleozoic accretionary wedge in its direct adjacency. The γ_{oct} sections are displaced laterally and equal-value sections are juxtaposed against each other.

In the Pichilemu area also often kinkbands occur (Fig. 7.5), which have an invariably steep dip of 65°-85° and are mostly conjugated to each other. They have a thickness of up to 3-4 cm and the foliation within is rotated antithetical. The kinkbands are mostly bound to pelitic rocks and are probably formed due to subhorizontal shortening. Upright folding of these kinkbands around steep dipping axis occurs locally.

Fig. 7.5 : (a) Steeply dipping kinkbands from the Bucalemu – Lago Vichuquén (point 5 and 6 of Fig. 7.3) area. Sometimes they are folded and rotated into a flatter position. (inside the dashed circle) (b) Often the kinkbands are conjugated with ~ an angle of 45° to each other. They have a preferred orientation of NE - SW.
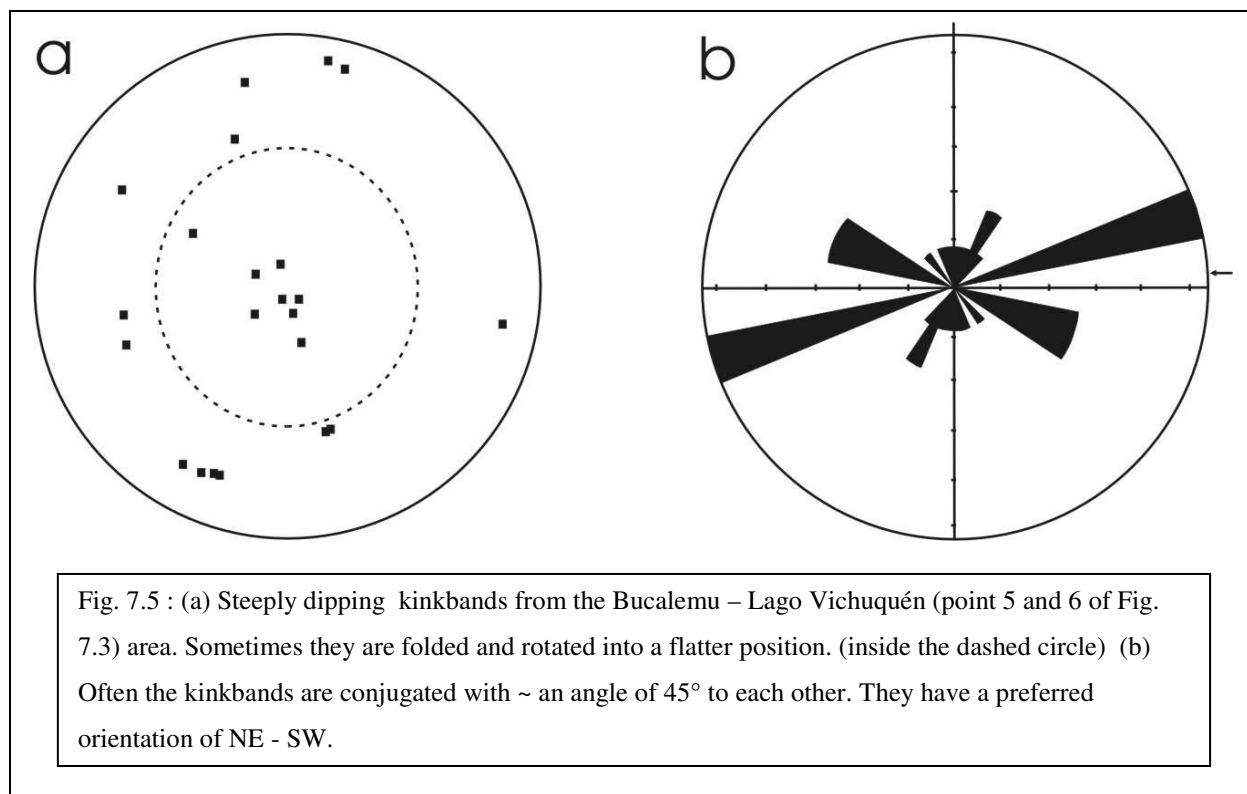
At several locations (Infernillo –Pichilemu; Punta Lobos; Bucalemu) semibrittle shear zones can be observed. This shear zones are rather small and can normally be traced for about 30m – 100m. Within these mostly subvertical shear zones smaller cataclastic zones of dm thickness can be found (See also chapter *7.4: Shear zones*).

7.3 Structures in the Los Vilos area

In the Los Vilos area in the Eastern Series S_0 and S_1 structures have been observed, whereas both have subparallel orientations. Large scale, upright folds characterize the whole series. The steep axial planes of these upright folds may alternate slightly, but are in most cases dipping to the west. Most of these folds have fold axis trending to the NW (Fig. 7.6) and the single planes show dip angles between 60°-80°. Hence, the Eastern Series shows similar structures as in the Constitución and Pichilemu area. In the easternmost part it can be observed, that coinciding with the Pichilemu area the basement is overlain by Mesozoic sediments.

The Western Series shows flat lying, subhorizontal orientations. Most planes have dipping angles around ~ 30° and show no preferred dipping directions. Mostly they present open folds showing a circular strike. Generally the S_2 and S_3 planes of the Western Series show random distribution patterns, except in the westernmost part, which is locally characterized by subhorizontal S_3 planes and might represent the structurally lowest unit. Eastern Series and especially the Western Series are intruded by numerous basaltic and rhyolitic dykes.

Fig. 7.6: (a) Pole diagramm of of the Eastern Series with a calculated average β axis, plunging flatly to the NW. (b) and (c) show that most planes are rather steep and have a NW- SE orientation. (d)-(e) Shows a stereoplots of the mostly flat lying Western Series. There is only a very weak preferred NW – SE orientation.

(Data Fig. (a)-(c) own data and T. Charissé 2004, data Fig. (d)-(e) from T. Charissé 2004 and additional own data.)

Fig. 7.7 shows in detail that the upright folds of the Eastern Series and the flat lying structures of the Western Series are separated by steep shear zones with different kinematics and different dipping directions (see Chapter *7.4: Shear zones*).

Near the shear zones the planes are often steepened with dip angles up to 80°. In many cases N – S trending kinkband systems can be observed which are obviously related to the shear zones which have the same orientation. In contrast to the Constitución – Pichilemu area structures are difficult to trace in this area and even if they are not affected by shear zones or intruding dykes they are much more inhomogeneous than in the south.

Fig. 7.7: (a) Showing schematic cross section in Los Vilos. Eastern- and Western Series are separated from each other by several shear zones and intruded by rhyolitic and basaltic dykes. (b) - (e) Shows that the sinistral shear zones have additionally normal fault and thrust fault components.
(The cross section has been developed with own field date and additionally data from T. Charissé, T. Güth and S. Reballedo).

7.4 Shear zones

The area of Punta Los Lobos and the Infernillo near Pichilemu, and especially the area of Los Vilos are characterized by young, mostly N-S trending shear zones. These strike-slip faults show consistently a sinistral sense of shear and can be traced for about 100-200m near Pichilemu and even for several hundred meters in the Los Vilos area. In Los Vilos these semiductile zones reach widths between 5 and 50 m. In most cases they have a subvertical position with steep dipping of 75° - 90°. Sometimes they show a thrust component and are associated with zones of cataclastic material with varying thickness. Often synthetic Riedel shears to the main fault can be observed and used to determine the sense of shear. In a few cases the appendant conjugated Riedel shears become apparent as well (Fig.7.8).

Fig.7.8 (a) shows the for the Los Vilos area common average orientation of the shear zones of 76°/81°, which means that they are predominantly steep standing and have an ENE dipping. Mostly the Riedel shears have an angle of 30°-35° to the main shear planes and are orientated in NE-SW direction. In most cases a sinistral shear sense can be obseved (Fig 7.8 (b)).

Fig. 7.8: (a) Pole diagram with shear plane orientations of Los Vilos, and indicated sinistral shear sense (b) Showing a rose diagram with separated directions of Riedel Shears and shear planes. (Data from T. Charissé 2004 & additional own data).
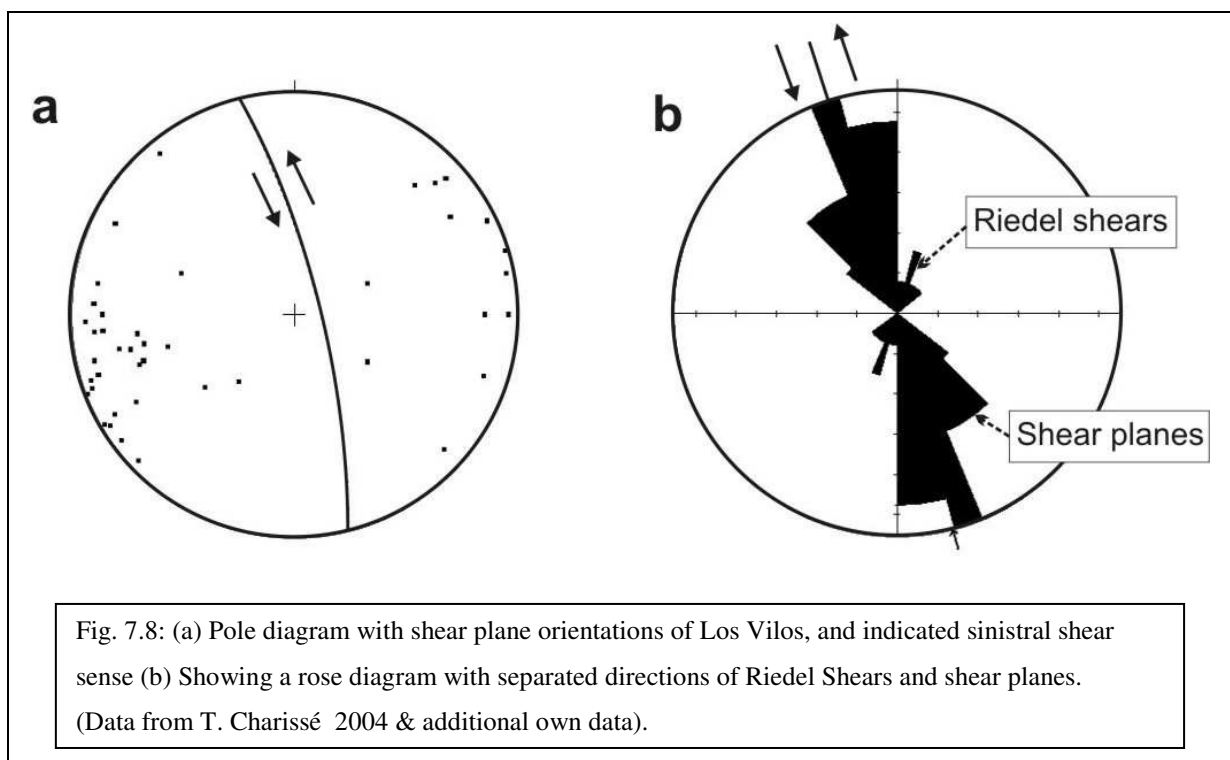
Furthermore often slickensides are preserved which also indicate a sinistral sense of shear. Crack veins, boudins and shear fractures parallel to the shear zones in mudstones support this observation.

The shear zones show shortening perpendicular to the subduction direction of the accretionary wedge. Although no relative ages between the single shear zones could be assessed it is obvious that the shear zones reflect an E-W orientated shortening event, with a huge strike–slip component.

However, Eastern and Western Series are unconformably overlain by a Triassic breccia, which is also affected by the shear zones. The contact between the breccia and the underlying basement is sharp, but within the breccia a slight N-S tendency of the longitudinal axis of its elliptical shaped clasts has been measured (CHARRIER, 1985). This fits with the strike of the considerably younger shear zones.

The shear zones often occur together with a bimodal magmatism of undeformed rhyolitic and basaltic dykes, which makes it possible to draw conclusions concerning the ages of the strike–slip faults. In Los Vilos these semibrittle shear zones are cross cutting this bimodal dykes of Jurassic ages. Similar structures can be found widely along the coast of north-central Chile (REBELLEDO & CHARRIER, 1997, IRVINE ET AL., 1988).

7.5 Stretching lineation

In the entire Constitución – Pichilemu area a WNW- ESE trending stretching lineation $L_{2/3}$ is present. It is marked by elongated quartz grains and quartz rodding. Mostly it is subparallel to the F_2 fold axes. The orientation of the stretching lineation does not change along traverses from Eastern to the Western Series. Mainly statically grown porphyroblasts (predominantly biotite, andalusite and staurolithe) show quartz-filled tension gashes with the same direction as the regional stretching lineation. Shear bands, asymmetric folds and quartz boudins yield a consistent top WNW sense of shear in the Eastern Series. With increasing vertical shortening, in the Western Series $L_{2/3}$ show alternating top to the WNW and top to the ESE shear senses. Late quartz filled tension gashes cut all older structures.

Fig. 7.9 shows that the X directions from strain analysis have the same approximately E – W trending orientation as the stretching lineation observed in field. It is notable that the F_1 folds of the Eastern Series, the penetrative foliation and the magmatic arc are perpendicular to this direction.

The younger Pichilemu- Vichuqén fault in the north of the area does not seem to affect the orientation of the stretching lineation with the exception of an anomalous area north of Lago Vichuquén with N-S trending directions.

In the northernmost part, the area of Los Vilos these stretching lineations have a much more complicated distribution pattern, because they are often affected by the multiple younger shear zones. Because of this, the stretching lineations can only be observed in these cases, where the accretion related structures are well preserved (for detail see Chapter *7.4: Shear zones*).
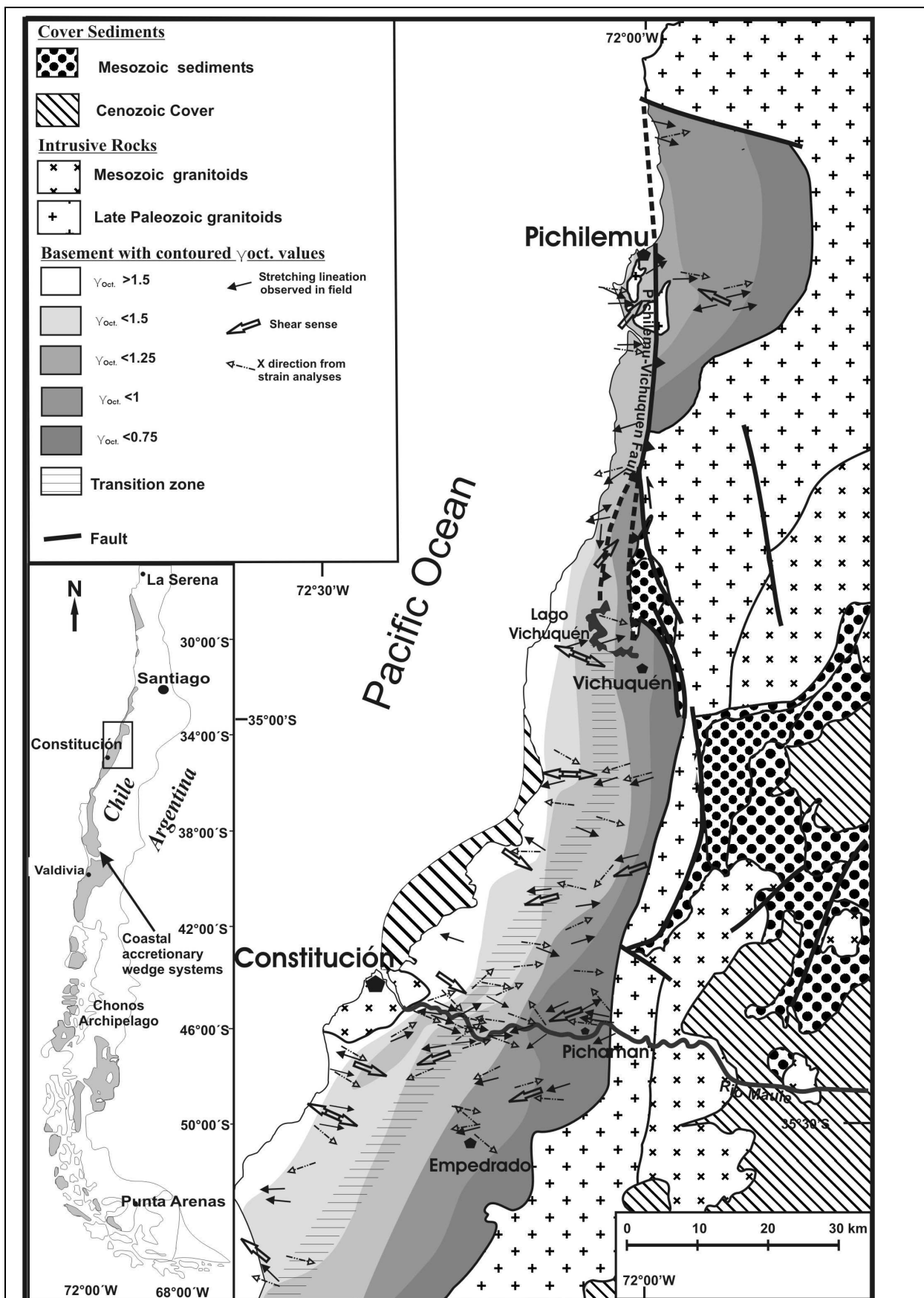
Fig. 7.9: Preferred stretching lineations, x directions from strain analysis and shear senses in the Constitución – Pichilemu area.

8. Strain data

In order to shed light on the strain conditions in the Chilean accretionary wedge 115 samples were collected all over the working area. Therefrom finite strain data were calculated with the Rf/Φ, XTG and PDS methods. The data are shown in Tables 8.1-8.3 and 8.4 and the localities of the finite strain samples are shown in Fig. 8.1 for the area between Constitución and Pichilemu and in Fig. 8.2 for Los Vilos.
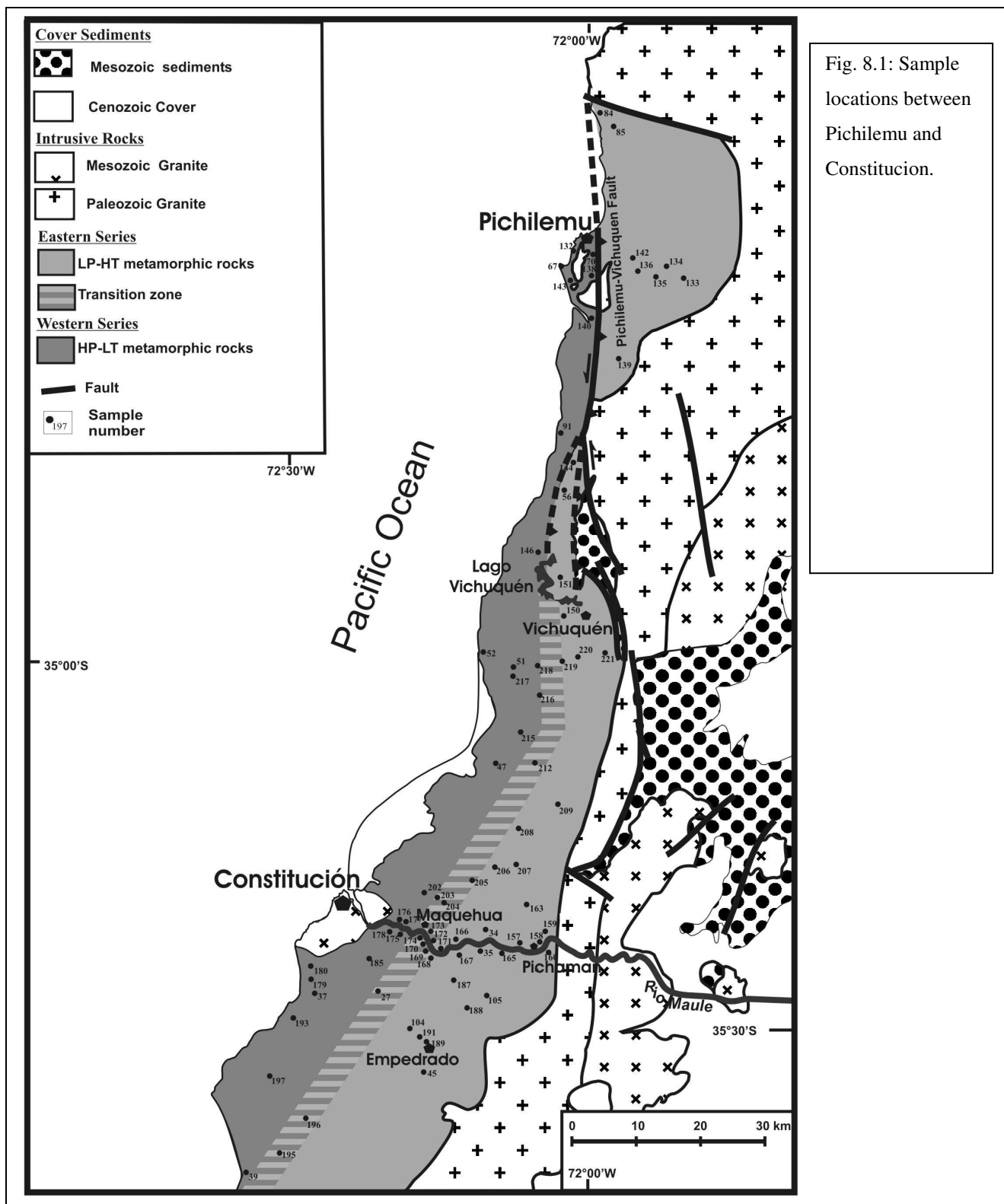
Fig. 8.1: Sample locations between Pichilemu and Constitucion.

Fig. 8.2: Sample locations in the area north of Los Vilos.
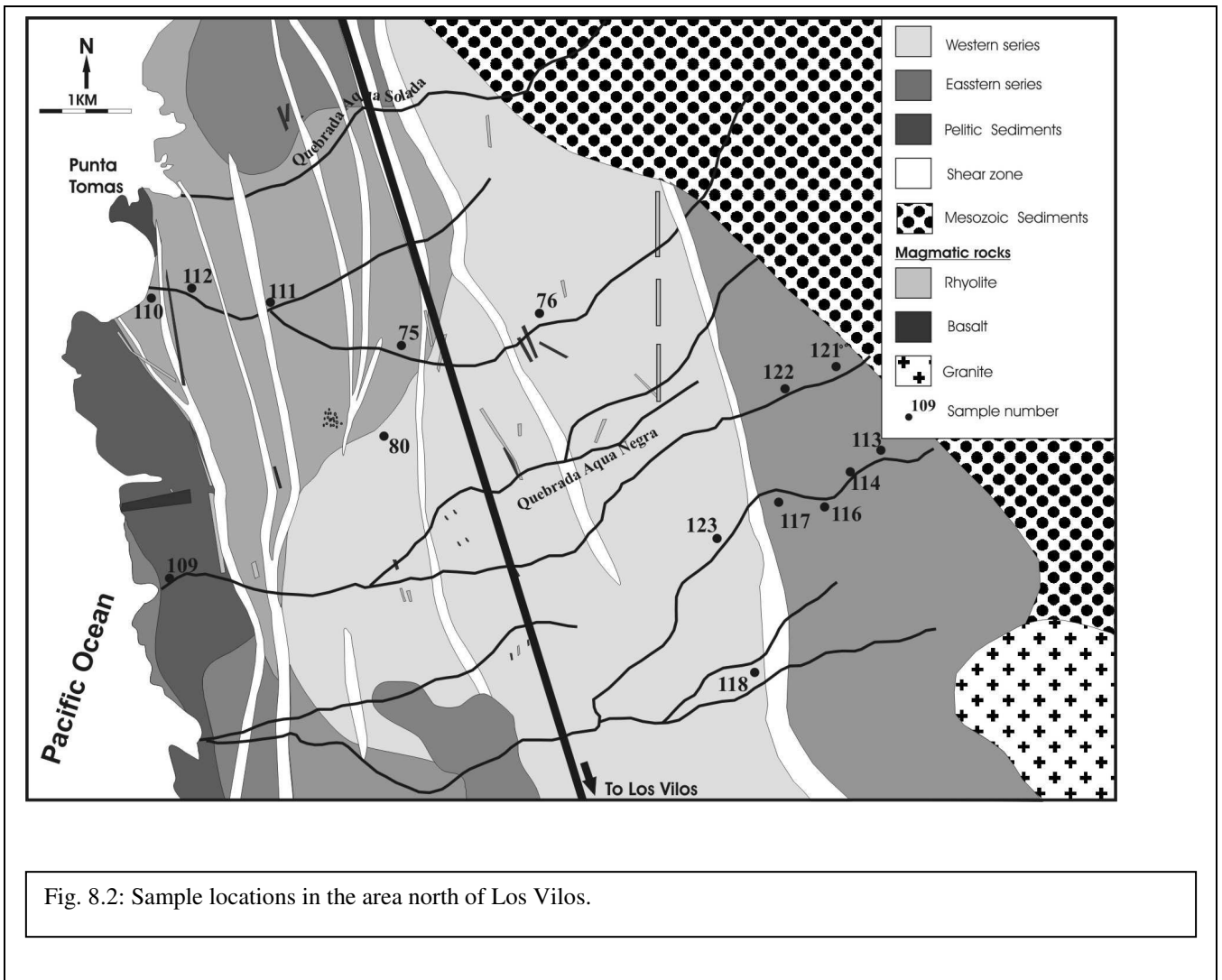
8.1 Conventional octahedral shear strain

In order to compare the strain data of the different methods the conventional octahedral shear strain $\gamma_{oct.}$ was calculated and has been plotted and contoured in Fig. 8.3, Fig. 8.4 and Fig. 8.5. For contouring intervals < 0.5, 0.5 – 0.75, 0.75 – 1.00, 1.00 – 1.25, 1.25 – 1.5 and > 1.5 have been chosen, to ensure that the resolution is high enough to draw a conclusion about the strain distribution. The thresholds of the single intervals are selected randomly.
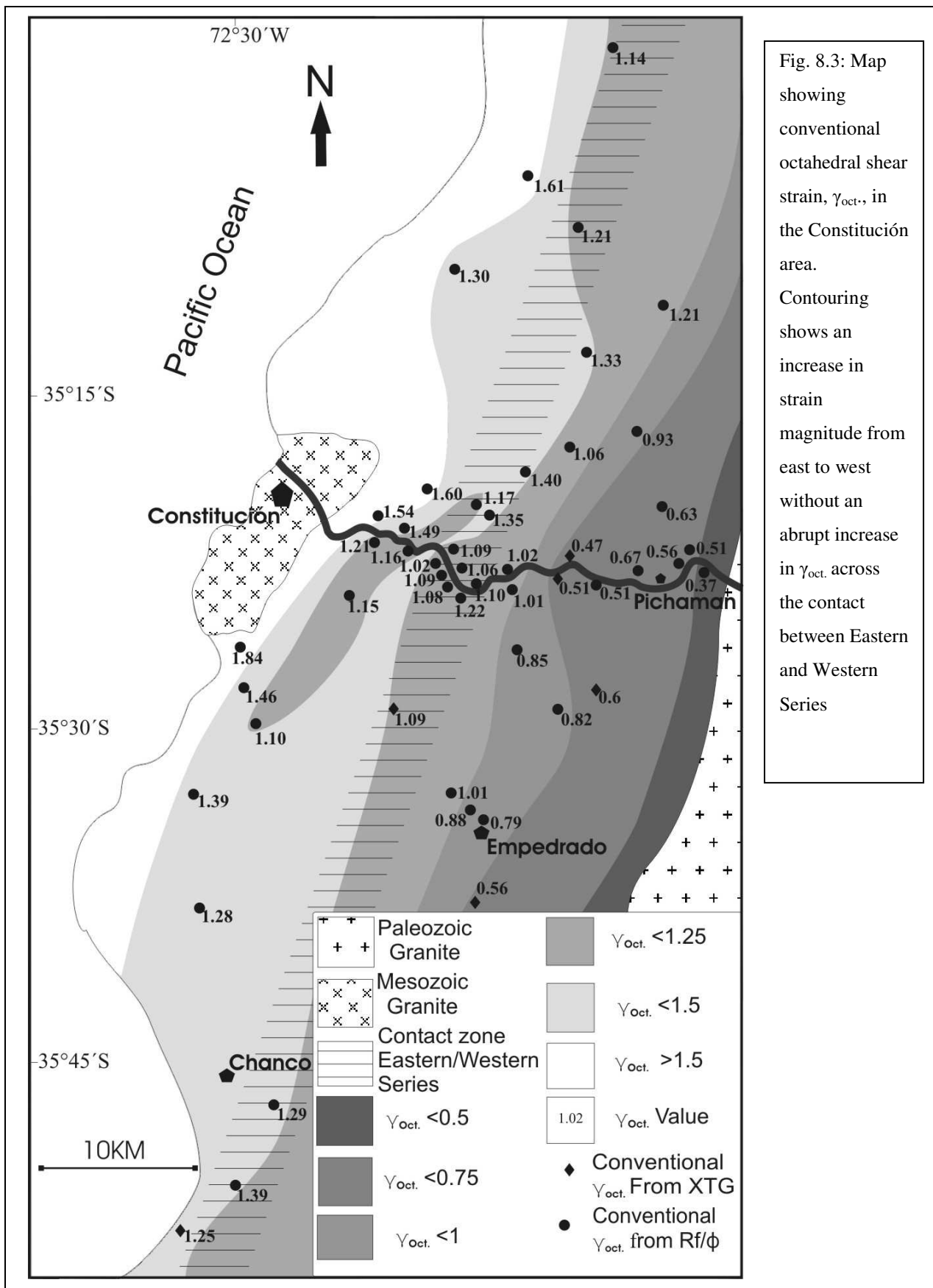
Fig. 8.3: Map showing conventional octahedral shear strain, $\gamma_{oct.}$, in the Constitución area. Contouring shows an increase in strain magnitude from east to west without an abrupt increase in $\gamma_{oct.}$ across the contact between Eastern and Western Series
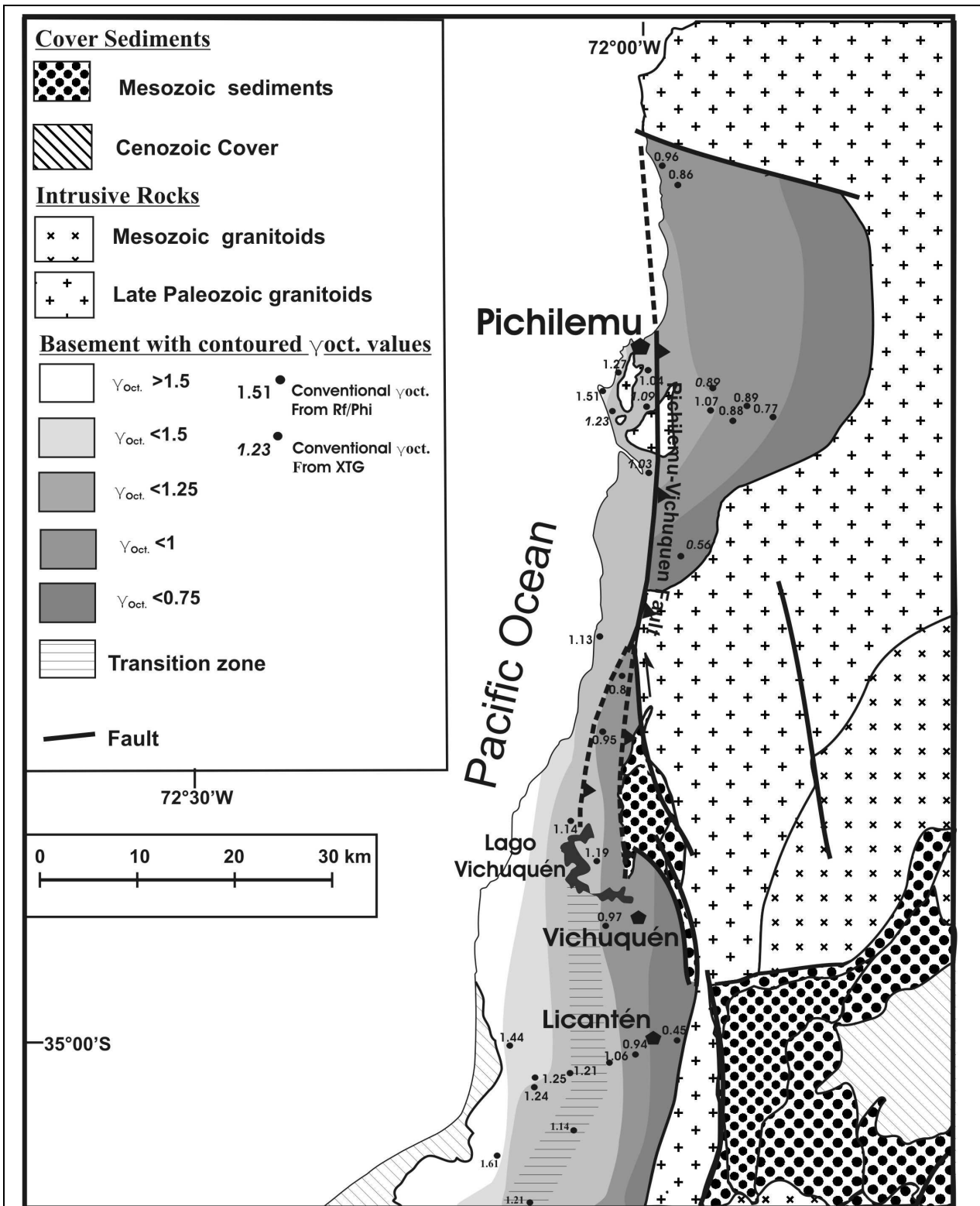
Fig. 8.4: Map showing conventional octahedral shear strain, $\gamma_{oct.}$, in the Pichilemu area. Contouring shows an increase in strain magnitude from east to west without an abrupt increase in $\gamma_{oct.}$ across the contact between Eastern and Western Series, although in the northern part the Eastern and Western Series are separated by the Cretaceous Pichilemu Vichuqén fault.

Table 8.1: Strain data for Constitución (Fig. 8.3)

| Sample	X-direction	Y-direction	Z-direction	S_x	S_y	S_z	R_{xy}	R_{xz}	R_{yz}	$\gamma_{oct.}$
CH-02-27	92°/04°	182°/01°	272°/86°	1.93	0.75	0.69	2.58	2.78	1.08	1.09
CH-02-30	325°/18°	218°/46°	71°/45°	1.26	0.56	0.39	2.24	3.26	1.45	1.18
CH-02-34	292°/62°	207°/02°	116°/28°	1.25	0.98	0.82	1.29	1.55	1.19	0.37
CH-02-35	120°/34°(-X)	209°/0°	301/56°	1.40	0.91	0.79	1.54	1.78	1.16	0.51
CH-02-37	140°/05°	230°/02°	326°/85°	1.93	0.79	0.66	2.45	2.92	1.19	1.10
CH-02-39	290°/04°	198°/06°	40°/82°	2.07	0.72	0.67	2.88	3.08	1.07	1.25
CH-02-75	56°/22°	154°/24°	270°/62°	1.86	0.84	0.64	2.22	2.89	1.31	1.05
CH-02-83	288°/05°	198°/06°	45°/83°	1.76	1.08	0.53	1.63	3.36	2.05	1.19
CH-02-92	282°/43°	180°/14°	76°/43°(-Z)	1.97	0.76	0.67	2.59	2.96	1.14	1.14
CH-02-93	274°/56°	184°/03°	93°/33°(-Z)	1.95	1.01	0.51	1.93	3.86	2.00	1.38
CH-02-98	296°/50°	201°/18°(-Y)	98°/48°	1.37	0.88	0.83	1.56	1.66	1.07	0.47
CH-02-104	320°/42°	210°/20°	102°/40°(-Z)	1.86	0.77	0.70	2.41	2.66	1.10	1.01
CH-02-107	103°/80°	192°/0°	283°/10°	1.46	0.91	0.75	1.60	1.96	1.22	0.60
CH-02-109	54°/63°	335°/0°	234°/26°(-Z)	1.89	0.95	0.56	2.00	3.40	1.70	1.21
CH-04-157	66°/60°	192°/20°	290°/20°	1.26	0.93	0.59	1.35	2.13	1.58	0.67
CH-04-158	278°/39°	52°/42°	166°/22°	1.22	0.86	0.63	1.41	1.93	1.37	0.57
CH-04-159	276°/2°	11°/86°	184°/15°	1.23	0.79	0.69	1.55	1.79	1.15	0.52
CH-04-160	228°/76°	11°/12°	102°/6°	1.29	0.93	0.84	1.39	1.54	1.10	0.38
CH-04-164	96°/60°	4°/2°	274°/30°	1.25	1.10	0.64	1.14	1.96	1.72	0.62
CH-04-165	87°/4°	177°/2°	269°/85°	1.29	0.83	0.73	1.55	1.76	1.13	0.51
CH-04-166	88°/18°	126°/28°	327°/58°	1.62	1.11	0.56	1.46	2.90	1.99	1.02
CH-04-167	129°/25°	224°/6°	324°/64°	1.59	1.13	0.56	1.41	2.86	2.03	1.01
CH-04-168	73°/38°	163°/2°	254°/52°	2.16	0.87	0.63	2.48	3.45	1.39	1.28
CH-04-169	56°/15°	330°/2°	233°/74°	1.75	1.00	0.57	1.75	3.08	1.76	1.07
CH-04-170	126°/8°	34°/7°	264°/78°	1.52	1.26	0.52	1.21	2.93	2.42	1.10
CH-04-171	107°/3°	181°/16°	15°/70°	1.60	1.08	0.50	1.48	3.20	2.16	1.15
CH-04-172	106°/1°	182°/18°	12°/71°	1.60	1.02	0.53	1.57	3.04	1.94	1.07
CH-04-173	145°/15°	54°/7°	286°/72°	1.96	0.93	0.64	2.11	3.08	1.46	1.10
CH-04-174	113°/3°	22°/2°	266°/83°	1.63	1.09	0.56	1.50	2.92	1.96	1.02
CH-04-175	94°/22°	194°/20°	323°/60°	1.64	1.19	0.51	1.38	3.18	2.31	1.16
CH-04-176	135°/13°	39°/28°	258°/56°	1.67	1.38	0.43	1.21	3.87	3.20	1.55

CH-04-177	71°/22°	163°/18°	290°/62°	1.84	1.19	0.46	1.54	4.03	2.61	1.49
CH-04-178	113°/22°	10°/05°	260°/65°	1.95	0.88	0.58	2.22	3.36	1.51	1.21
CH-04-179	121°/10°	213°/8°	344°/78°	2.21	0.78	0.58	2.83	3.83	1.35	1.46
CH-04-180	120°/20°	212°/2°	295°/68°	2.50	0.77	0.52	3.25	4.82	1.48	1.84
CH-04-185	60°/36°	149°/02°	242°/55°	1.86	0.94	0.57	1.98	3.26	1.65	1.15
CH-04-187	244°/75°	12°/10°	115°/10°	1.56	1.04	0.61	1.50	2.55	1.70	0.86
CH-04-188	74°/25°	340°/10°	224°/62° (-Z)	1.15	0.69	0.46	1.66	2.48	1.49	0.82
CH-04-189	132°/60°	19°/13°	282°/25° (-Z)	1.27	0.80	0.52	1.59	2.42	1.52	0.79
CH-04-191	260°/19°	162°/19°	29°/62°	1.29	0.72	0.50	1.81	2.58	1.43	0.88
CH-04-193	130°/02°	220°/22°	30°/68° (-Z)	2.14	0.82	0.57	2.62	3.72	1.42	1.39
CH-04-195	104°/36°	12°/04°	264°/52° (-Z)	1.95	1.03	0.50	1.89	3.90	2.06	1.40
CH-04-196	81°/52°	192°/12°	288°/34°	1.76	1.15	0.50	1.53	3.55	2.32	1.29
CH-04-197	251°/02°	342°/20°	152°/72°	1.62	1.03	0.60	1.57	2.70	1.72	0.92
CH-04-202	47°/21°	142°/14°	261°/64°	2.25	0.87	0.51	2.59	4.37	1.68	1.61
CH-04-203	100°/34°	192°/01°	283°/54°	1.94	0.86	0.60	2.24	3.25	1.45	1.18
CH-04-204	76°/08°	346°/01°	254°/82°(-Z)	2.08	0.84	0.57	2.49	3.63	1.46	1.34
CH-04-205	84°/06°	176°/02°	288°/82°	2.13	0.84	0.56	2.55	3.80	1.49	1.41
CH-04-206	98°/26°	201°/26°	312°/62°	1.72	1.03	0.56	1.66	3.06	1.84	1.07
CH-04-207	76°/65°	190°/11°	285°/22°	1.77	0.83	0.68	2.14	2.60	1.22	0.94
CH-04-208	283°/26°	29°/31°	161°/48°	1.94	1.00	0.52	1.95	3.74	1.92	1.34
CH-04-209	219°/58°	349°/24°	90°/22°	1.72	1.14	0.51	1.51	3.35	2.22	1.21
CH-04-212	106°/02°	16°/02°	262°/88° (-Z)	1.67	1.19	0.50	1.40	3.32	2.37	1.22
CH-04-215	273°/09°	183°/07°	50°/79°(-Z)	2.38	0.68	0.61	3.49	3.88	1.11	1.61
CH-04-216	130°/04°	222°/22°	38°/68°(-Z)	1.95	0.80	0.64	2.43	3.06	1.26	1.14

In the Constitución area, $\gamma_{oct.}$ shows a pronounced increase in strain magnitude from east to west, whereas the smallest value of 0.37 (east of Pichaman) occurs in the easternmost part and the highest value of 1.84 (south of Constitución) in the westernmost part near the Pacific coast. In the same direction there is an increase in the maximum stretch, S_x, which ranges from 1.23 in the east to 2.50 in the west. Consistent with this the maximum shortening, S_z, ranges from 0.84 in the east to 0.46 in the west.

The least deformed samples ($\gamma_{oct.}$ <0.75) are from areas characterized by upright F_1 folding, preserved sedimentary structures and axial-plane S_1 foliation (see chapter *7: Structural data*). The contour interval of $\gamma_{oct.}$, 0.75-1.00, coincides with folding of S_1 by F_2 folds and an incipient development of a S_2 foliation. In the $\gamma_{oct.}$ interval of 1.00-1.25 the S_2 foliation is

rotated into a subhorizontal position which is associated with a pervasive development of S_2. The contact between Eastern and Western Series approximately coincides with γ_{oct} values of 1.25-1.50. In the westernmost and structurally lowermost outcrops of the Western Series values increase up to $\gamma_{oct.} > 1.50$.

Table 8.2: Strain data for Pichilemu (Fig. 8.4)

Sample	x-direction	y-direction	z-direction	S_x	S_y	S_z	R_{xy}	R_{xz}	R_{yz}	$\gamma_{oct.}$
CH-02-51	292°/16°	26°/14°	156°/68°	2	0.8	0.6	2.51	3.35	1.34	1.25
CH-02-52	329°/39°	100°/39°	224°/28°	2.04	0.97	0.51	2.11	4.04	1.91	1.45
CH-02-56	93°/13°	01°/14°(-Y)	223°/70°	1.29	0.7	0.47	1.84	2.77	1.51	0.96
CH-02-67	350°/18°	78°/24°	216°/60°	1.76	1.22	0.44	1.44	4	2.78	1.51
CH-02-70	230°/03°	332°/210°	131°/68°	1.88	0.77	0.7	2.44	2.71	1.11	1.03
CH-02-84	213°/15°	304°/02°	36°/76°	1.27	0.58	0.43	2.06	2.72	1.33	0.96
CH-02-85	288°/05°	198°/06°	45°/83°	1.35	0.8	0.53	1.68	2.56	1.52	0.86
CH-02-91	336°/23°	234°/28°(-Y)	100°/52°	1.77	0.66	0.62	2.68	2.85	1.06	1.14
CH-04-132				1.82	0.72	0.53	2.54	3.41	1.34	1.28
CH-04-133	195°/05°	290°/51°	100°/39°	1.18	0.72	0.5	1.64	2.36	1.44	0.77
CH-04-134	53°/01°	145°/23°	319°/50°	1.66	0.95	0.63	1.74	2.65	1.52	0.9
CH-04-135	35°/34°	300°/07°	199°/54°(-Z)	1.7	0.89	0.66	1.9	2.58	1.36	0.89
CH-04-136	304°/24°	196°/34°	60°/47°(-Z)	1.7	1.06	0.55	1.6	3.07	1.92	1.08
CH-04-138				1.76	0.71	0.61	2.47	2.88	1.16	1.09
CH-04-139				1.2	0.82	0.57	1.61	1.71	1.44	0.56
CH-04-140	308°/18°	212°/21°	75°/62°(-Z)	1.66	0.88	0.56	1.88	2.97	1.58	1.03
CH-04-142	254°/31°	147°/26	24°/48°	1.27	0.86	0.49	1.47	2.62	1.78	0.89
CH-04-143	25°/20°	113°/02°	212°/68°	2.05	0.74	0.66	2.76	3.13	1.14	1.23
CH-04-144				1.45	0.72	0.64	2.02	2.28	1.13	0.8
CH-04-146	25°/20°	113°/02°	212°/68°	1.79	0.98	0.51	2.43	2.75	1.93	1.14
CH-04-150	102°/06°	191°/01°	289°/84°	1.62	1.08	0.57	1.49	2.82	1.89	0.98
CH-04-151	56°/03°	147°/30°	320°/60°	1.83	0.74	0.62	2.48	2.95	1.19	1.12
CH-04-217	104°/25°	205°/21°	329°/55°	1.96	0.9	0.57	2.19	3.47	1.58	1.25
CH-04-218	301°/34°	207°/08°	102°/54°(-Z)	2.03	0.75	0.66	2.7	3.1	1.15	1.21
CH-04-219	296°/05°	213°/42°	31°/48°	1.76	0.98	0.58	1.79	3.06	1.71	1.07
CH-04-220	68°/02°	158°/20°	325°/74°	1.76	0.86	0.66	2.04	2.69	1.32	0.95
CH-04-221	65°/62°	165°/08°	258°/27°	1.15	0.99	0.68	1.17	1.69	1.45	0.46

In the southern part of the Pichilemu area the distribution of the finite strain data is very similar to that in the Constitución area. The $\gamma_{oct.}$ values increase smoothly from 0.45 east of Licantén up to 1.61 near the Pacific coast in the west. The northern part is characterized by the Pichilemu-Vichuquén fault which crops out from the Lago Vichuquén to Pichilemu where it continues in the Pacific Ocean. East of the fault $\gamma_{oct.}$ values range from 0.56 to 0.96, whereas they range between 1.01 and 1.51 west of the fault. On each side of the fault there is again a smooth increase in strain magnitude from east to west. The maximum stretch S_x in the Pichilemu area range between 2.05 in the west and 1.18 in the east. The maximum shortening S_z again increases towards the east. At the coast at Punta Los Lobos S_z has values of 0.44 and in the Eastern Series it goes up to 0.66. It is important to notice that there are no detectable breaks in the $\gamma_{oct.}$ values at the Pichilemu-Vichuquén fault.

As interpretation for this it can be assumed that the vertical offset probably must have been rather small. In contrast, the lateral displacement might be more significant, because the contour lines of equal γ_{oct} values show clearly a lateral offset. At the fault the contour lines of $\gamma_{oct.} < 0.75$, < 1.00 and < 1.25 are displaced against the γ_{oct} interval $1.25 - 1.5$. The map pattern suggests that the offset is approximately 20 to 25 km.

On the basis of the strain data the Pichilemu-Vichuquén fault is probably a sinistral, post accretional brittle fault with a bigger lateral offset and possibly an adittional small vertical component. This structure is only a local structure which is limited to the northern Pichilemu region (see chapter *9.2: Structural contacts: Pichilemu*).

The southern part, south of the Lago Vichuquén, shows the same distribution of $\gamma_{oct.}$ values as in the Constitución area. The $\gamma_{oct.}$ values range in the profile between Licantén and the coast from 0.45 in the east to 1.61 in the west. Again here the maximum stretch S_x increases and maximum shortening S_z decreases from east to west. Values for S_x range between 2.38 in the west and 1.15 in the easternmost part, whereas S_z reaches values of 0.51 in the west and 0.68 in the east.

Table 8.3: Strain data for Los Vilos (Fig. 8.5)

Sample	x-direction	y- direction	z-direction	S_x	S_y	S_z	R_{xy}	R_{xz}	R_{yz}	$\gamma_{oct.}$
CH-02-75	56°/22°	154°/24°	270°/62°	1.86	0.84	0.64	2.22	2.89	1.31	1.05
CH-02-76	02°/24°	97°/05°	200°/65°	1.4	0.87	0.82	1.61	1.71	1.06	0.5
CH-02-80	224°/17°	89°/52° (-Y)	324°/32°	1.11	0.98	0.93	1.13	1.19	1.05	0.15
CH-02-109	54°/63°	335°/0°	234°/26°(-Z)	1.89	0.95	0.56	2	3.4	1.7	1.21
CH-02-110	168°/04°	76°/36°	266°/54°	1.88	0.77	0.69	2.43	2.75	1.13	1.04
CH-02-111	54°/11°	324/02°	224°/78°	1.22	0.92	0.54	1.33	2.24	1.68	0.73
CH-02-112	46°/13°	138°/02°	237°/76°	1.23	0.6	0.45	2.06	2.72	1.32	0.96
CH-02-113	177°/50°	310°/30°	56°/25°	1.25	0.85	0.83	1.47	1.51	1.03	0.39
CH-02-114	154°/0°	64°/62°(-Y)	245°/28°	1.13	0.68	0.41	1.67	2.78	1.66	0.95
CH-02-116	216°/59°	01°/22°	100°/19°	1.4	0.66	0.43	2.12	3.27	1.54	1.17
CH-02-117	37°/44°	136°/10°	235°/44°	1.23	0.91	0.51	1.36	2.4	1.77	0.8
CH-02-118	298°/20°	196°/28°	55°/54°	1.77	0.8	0.71	2.2	2.5	1.13	0.91
CH-02-121	132°/24°	28°/25°(-Y)	260°/52°	1.11	0.99	0.68	1.13	1.63	1.45	0.43
CH-02-122	19°/26°	109°/0°	199°/64°	1.36	0.82	0.5	1.66	2.71	1.63	0.92
CH-02-123	170°/35°	223°/53°	71°/31°	1.43	0.85	0.82	1.69	1.74	1.03	0.53

The distribution of γ_{oct} values in Los Vilos is more complex than in the other areas. Because of the several postaccretionary shear zones, displacing Eastern and Western Series against each other, the continuous increase of strain can only be traced partly in this area. Therefore, there are no $\gamma_{oct.}$-contour lines shown in Fig. 8.5. Anyhow, it can be observed, that there are huge changes in the $\gamma_{oct.}$ values at the borders of different units; e.g. from 1.05 to 0.15. (Fig. 8.5)

Nevertheless, within the single units, so far they are not affected by any shear zones, a tendency of gradual increase can be recognised. In the easternmost part of the Los Vilos area, $\gamma_{oct.}$ values increase from east to west from 0.39 to 1.16. But even here it is difficult to observe a well defined distribution. In the middle part of the area, the Western Series crops out and shows a very erratic distribution of strain values. The maximum stretches S_x range between 1.89 and 1.11 and the maximum shortening S_z ranges between 0.82 and 0.41. But again it is not possible to bring these values in an ascending or descending order along a profile.

The reason for this unstructured, dispersive strain distribution are the younger shear zones occurring numerously in this area.

The distribution of the $\gamma_{oct.}$ values is depicted in this chapter in three different areas. The Constitución area shows a continuous transition between Eastern and Western Series (Fig. 8.3). The Pichilemu area contains a cretaceous brittle fault separating both series (Fig. 8.4), and in Los Vilos occurs a young shear zone system displacing the two series against each other (Fig. 8.5). These different structural conditions lead to slightly different distributions of the strain data. The closer inspection of the contact and the interpretation of the strain data are shown in chapter *9: Structural contacts*.
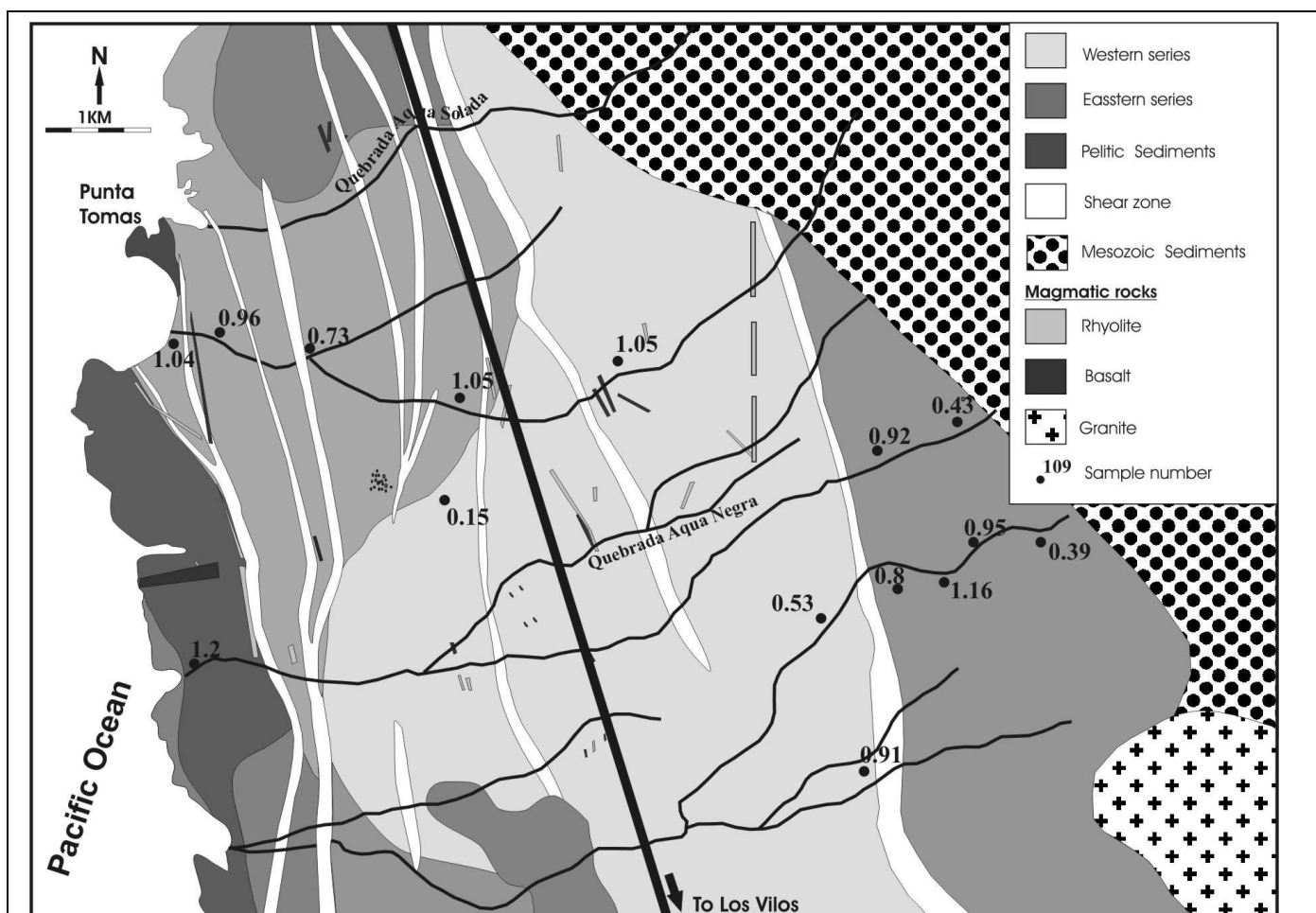

Fig. 8.5: Map showing conventional octahedral shear strain, $\gamma_{oct.}$, in the Los Vilos area. Because of the great displacement of the two series by several hear zones here are no $\gamma_{oct.}$ -contour lines shown. At the shear zones the $\gamma_{oct.}$ values often increase by leaps and bounds.

The presented $\gamma_{oct.}$ values in this chapter here have been calculated from Rf/Φ and XTG measurements. Additionally at several sample localities PDS measurements have been made. The $\gamma_{oct.}$ values calculated by the PDS measurements and in almost every case coincide very well with the $\gamma_{oct.}$ values calculated from the other methods.

 At comparable geological settings in different areas, the calculations for the conventional octahedral shear strain result approximately in the same values (e.g. $\gamma_{oct.}$ values for the Eastern Series always range between 0.3 and 1.2 independent of the locality where the sample was collected). Nevertheless, these data are discussed separately in the next chapter (*8.2: Strain analysis with the PDS method*), because with the PDS method the average Volume loss was calculated, which is needed for the calculation of the vertical ductile thinning (Chapter 10).

In Fig. 8.6 the axial ratios R_{xy} and R_{yz} are plotted aginst each other, in order to characterize the strain symmetry dependent on the $\gamma_{oct.}$ values. Therefore the diagram includes $\gamma_{oct.}$ iso-lines. The samples plotted here are from the Constitución and the southern Pichilemu area. It can be observed, that at the same $\gamma_{oct.}$ values different strain symmetries are occurring. This means, that highly prolate symmetries as well as oblate and plain strain symmetries can be observed at the same degree of distortion. With increasing octahedral shear strain the diversification of the symmetries increases as well. For the Rio Maule section these symmetries differ a lot in their distribution pattern. The cause for this distribution pattern cannot be clarified fully, but probably it is because of local structures like hinge zones and limbs in the different folds.
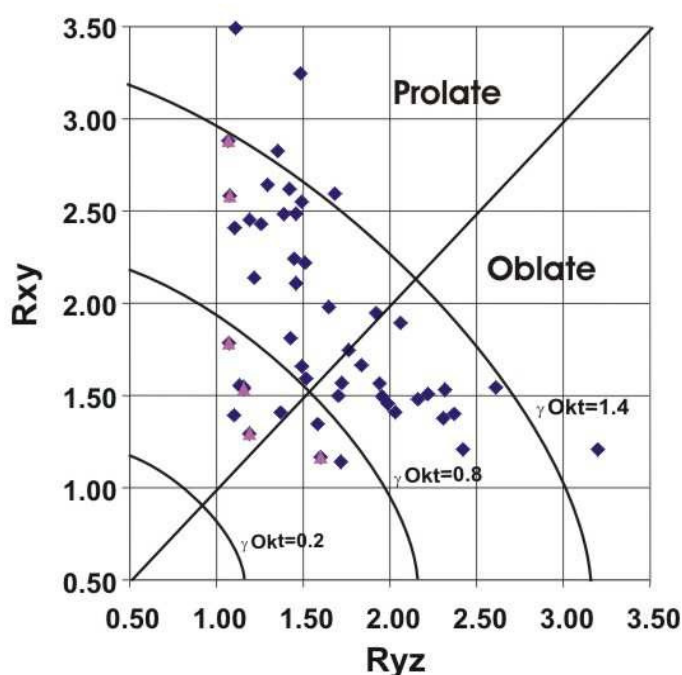

Fig. 8.6: Here the axial ratios R_{xy} and R_{yz} are plotted dependent on the $\gamma_{oct.}$ values (shown as $\gamma_{oct.}$ iso-lines). Data are showing prolate as well as oblate symmetries at the same $\gamma_{oct.}$ values. The diversification increases with increasing $\gamma_{oct.}$ values.

8.2 Strain analysis with the PDS method

To determine the volume loss in quartz grains the PDS method was used. Samples of the Eastern Series, with only pressure solution as deformation mechanism, have been measured in order to determine the average amount of SiO_2 a single grain lost during deformation
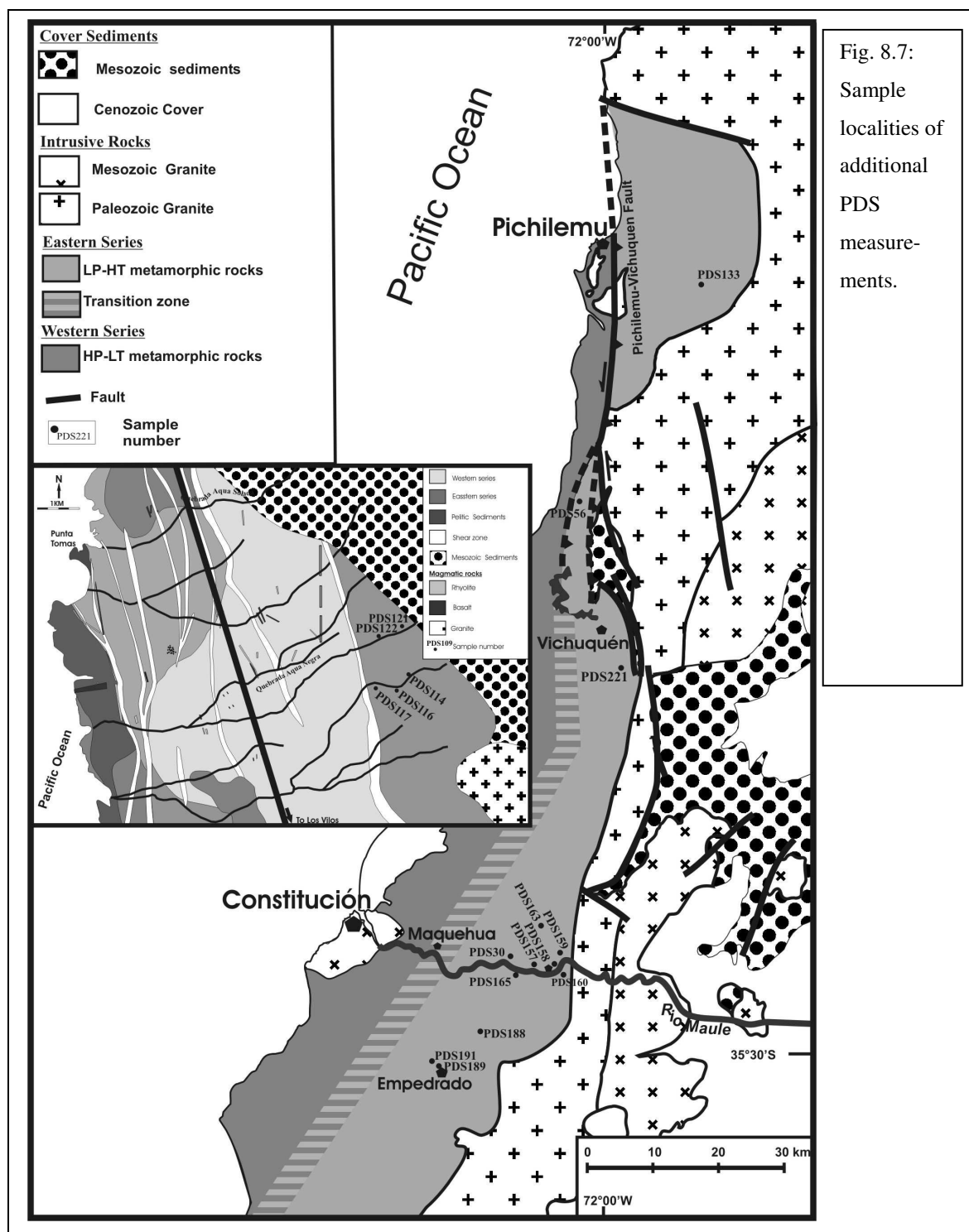

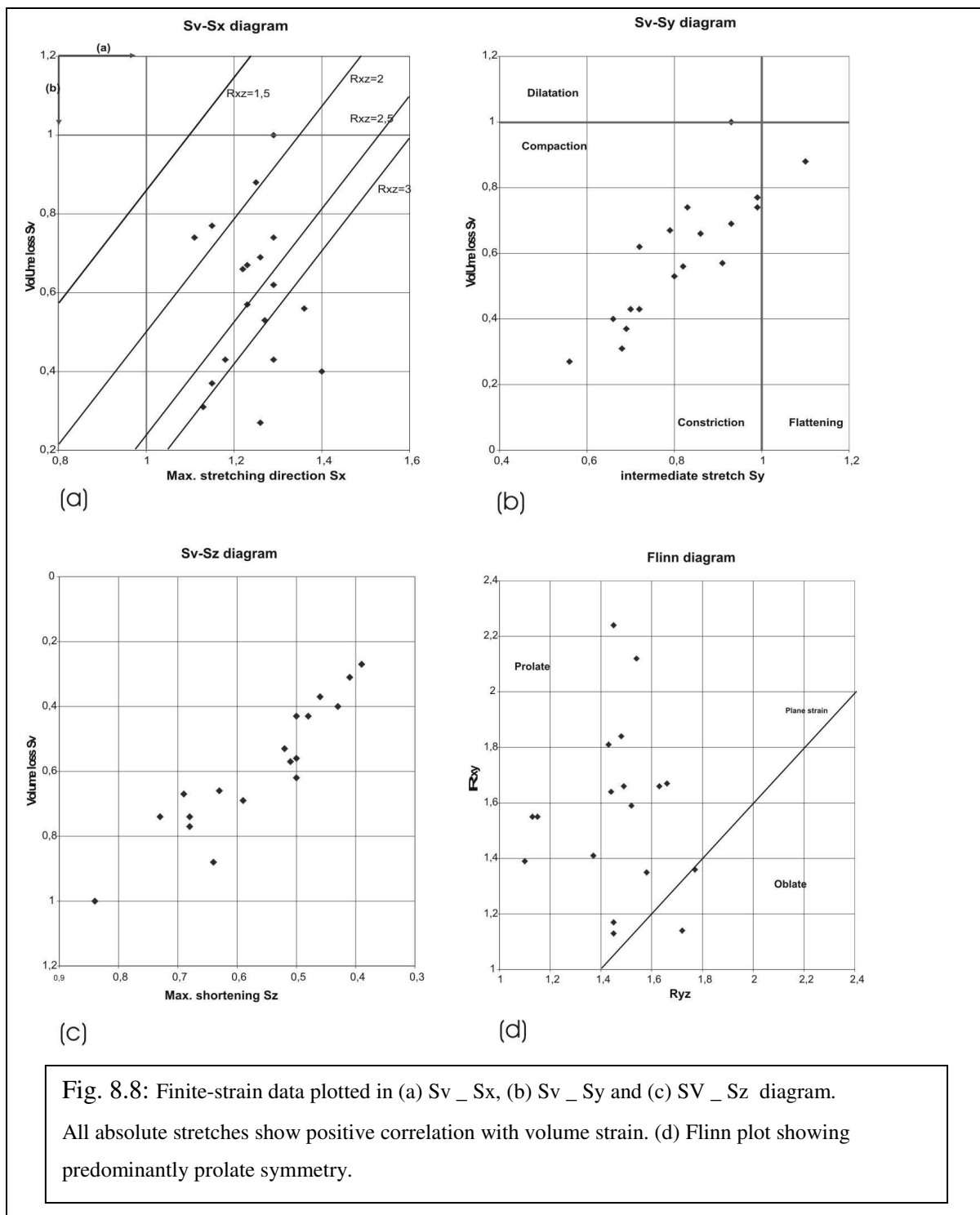Fig. 8.7: Sample localities of additional PDS measure-ments.

Table 8.4: Strain data from PDS measurements

Sample	x-direction	y- direction	z-direction	S_x	S_y	S_z	S_v	R_{xy}	R_{xz}	R_{yz}	$\gamma_{oct.}$
PDS-30	325°/18°	218°/46°	71°/45°	1.26	0.56	0.39	0.27	2.24	3.26	1.45	1.18
PDS-50	353°/14°	250°/41°	97°/45°	1.29	0.7	0.48	0.43	1.84	2.72	1.48	0.93
PDS-114	154°/0°	64°/62°(-Y)	245°/28°	1.13	0.68	0.41	0.31	1.67	2.78	1.66	0.95
PDS-116	216°/59°	01°/22°	100°/19°	1.4	0.66	0.43	0.4	2.12	3.27	1.54	1.17
PDS-117	37°/44°	136°/10°	235°/44°	1.23	0.91	0.51	0.57	1.36	2.4	1.77	0.8
PDS-121	132°/24°	28°/25°(-Y)	260°/52°	1.11	0.99	0.68	0.74	1.13	1.63	1.45	0.43
PDS-122	19°/26°	109°/0°	199°/64°	1.36	0.82	0.5	0.56	1.66	2.71	1.63	0.92
PDS-133	195°/05°	290°/51°	100°/39°	1.18	0.72	0.5	0.43	1.64	2.36	1.44	0.77
PDS-157	66°/60°	192°/20°	290°/20°	1.26	0.93	0.59	0.69	1.35	2.13	1.58	0.67
PDS-158	278°/39°	52°/42°	166°/22°	1.22	0.86	0.63	0.66	1.41	1.93	1.37	0.57
PDS-159	276°/2°	11°/86°	184°/15°	1.23	0.79	0.69	0.67	1.55	1.79	1.15	0.52
PDS-160	228°/76°	11°/12°	102°/6°	1.29	0.93	0.84	1	1.39	1.54	1.1	0.38
PDS-163	96°/60°	4°/2°	274°/30°	1.25	1.1	0.64	0.88	1.14	1.96	1.72	0.62
PDS-165	87°/4°	177°/2°	269°/85°	1.29	0.83	0.73	0.74	1.55	1.76	1.13	0.51
PDS-188	74°/25°	340°/10°	224°/62° (-Z)	1.15	0.69	0.46	0.37	1.66	2.48	1.49	0.82
PDS-189	132°/60°	19°/13°	282°/25° (-Z)	1.27	0.8	0.52	0.53	1.59	2.42	1.52	0.79
PDS-191	260°/19°	162°/19°	29°/62°	1.29	0.72	0.5	0.62	1.81	2.58	1.43	0.88
PDS-221	65°/62°	165°/08°	258°/27°	1.15	0.99	0.68	0.77	1.17	1.69	1.45	0.46

The maximum stretches S_x of the PDS samples are rather small and they range between 1.11 and 1.4. The values for S_y range between 0.56 and 1.11 and for S_z between 0.39 and 0.84. The average tensors for the principal stretches of table 8.4 are 1.24 for S_x, 0.82 for S_y and 0.57 for S_z. This means that there is an average extension in X direction of 24%. In Y direction, there is a shortening of 18% and due S_y is smaller than 1, it shows a constrictional strain type. The Z direction is the direction with the maximum distortion, and has a shortening of 43%. The samples have an average volume loss of 41%, because the average S_v has a value of 0.59.

All absolute stretches show a positive correlation with volume strain. Finite strain data have been plotted into $S_x - S_v$, $S_y - S_v$ and $S_z - S_v$ diagrams (Figs. 8.8 (a)-(d)). In the $S_v - S_x$ diagram, S_v and S_x can be regarded as the open and closed components of the deformational system. Therefore, a strain path parallel to S_v (b) would represent a pure volume strain, and a path parallel to S_x (a) would characterize constant-volume ($S_v = 1$) plane-strain deformation,

where extension in X is balanced by shortening in Z. Furthermore in the $S_v - S_x$ diagram (Fig. 8.8(a)) there are maximum axial ratio R_{xz} are plotted, which are considered to be a proxy for cleavage intensity. The closed-system case ($S_v = 1$) requires only half as much strain as the open-system case to produce the same R_{xz} ratio (BRANDON, 1995). As it is shown in diagram 8.8(a), the values do not plot on either of these strain paths, indicating that deformation apparently involved both closed and open-system behaviour.

Fig. 8.8: Finite-strain data plotted in (a) Sv _ Sx, (b) Sv _ Sy and (c) SV _ Sz diagram.
All absolute stretches show positive correlation with volume strain. (d) Flinn plot showing predominantly prolate symmetry.

In the S_v – S_y diagram (Fig. 8.8(b)) it is shown that the values plot in the constrictional field and show compaction. With the decrease of S_y an increase of S_v can be noticed, which means that with high shortening values of the intermediate direction, there is a great amount of volume loss.

The S_v – S_z diagram (Fig. 8.8(c)).shows correlating with the S_v - S_y diagram an increase of the volume loss if there is an increase of the shortening. Thus the shortening is compensated by volume loss and not by extension in X or Y direction.
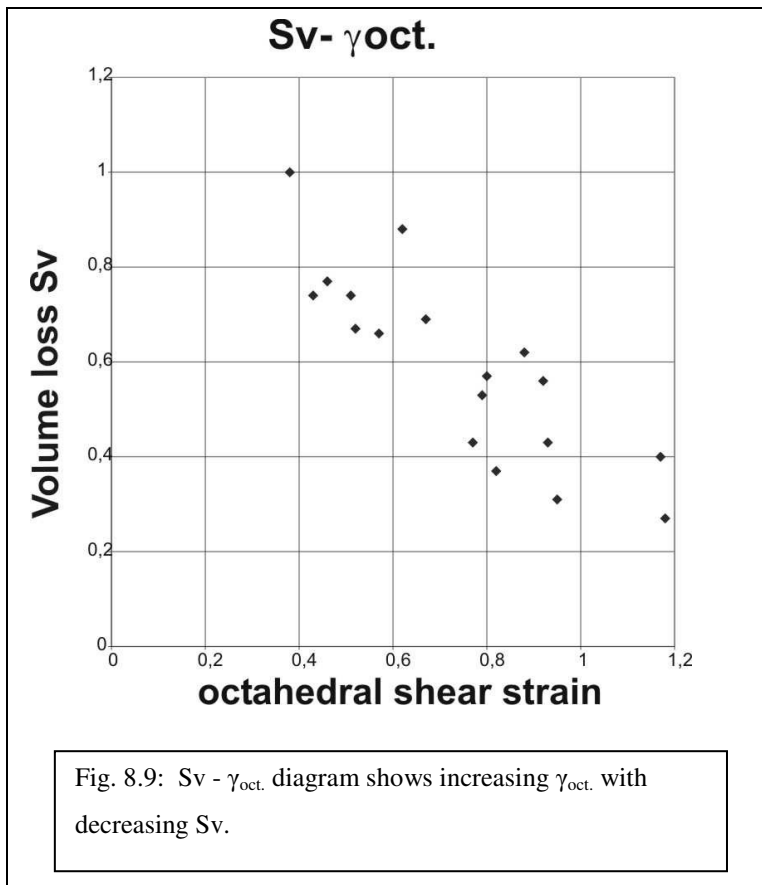
The values of the Flinn diagram (Fig. 8.8 (d)) plot predominantly in the prolate field *1< k<∞* . Because of the average volume loss of Δ = 41% the plane strain line does not hit the origin any more, but has the gradient *a = b(1+Δ)*.

The S_y - $\gamma_{oct.}$ (Fig. 8.9) diagram shows that S_v can vary a lot with the same octahedral shear strain. Nevertheless, there is the clear trend that $\gamma_{oct.}$ values increase with increasing amounts of solved material. This means the bigger the volume loss, the bigger becomes the $\gamma_{oct.}$ value.

Fig. 8.9: Sv - $\gamma_{oct.}$ diagram shows increasing $\gamma_{oct.}$ with decreasing Sv.
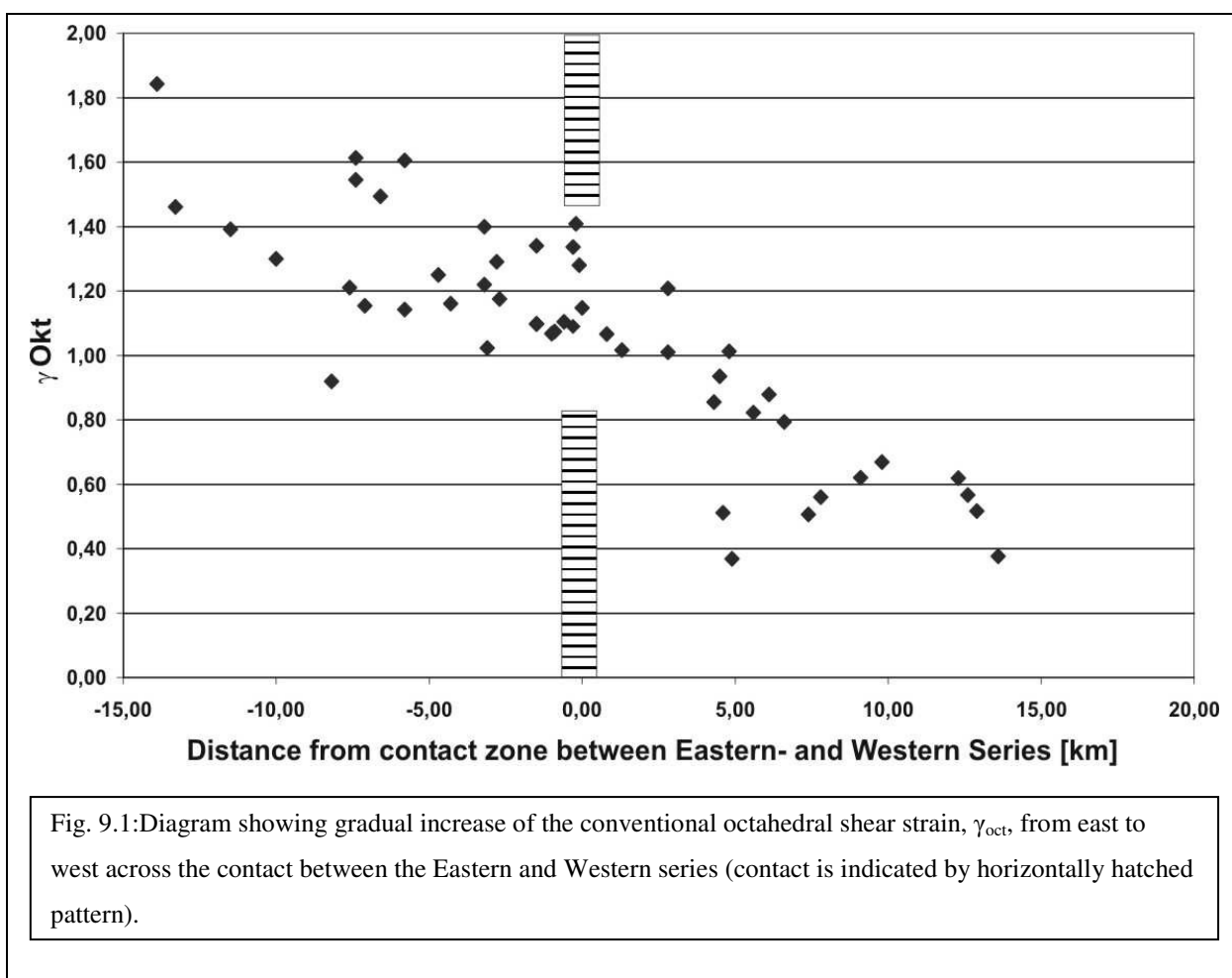
9. Structural contacts

To summarize the descriptions in the introduction and documentations by the structural and finite strain data in chapters 7 and 8 there are three different types of contact zones in the study area. The Rio Maule area represents a nearly undisturbed sequence of the ancient accretionary wedge. The Pichilemu area is characterized by the Pichilemu Vichuquén fault, a brittle structure probably formed at approximately 100 Ma (WILLNER ET AL., 2005). Near Huantelauquen, in the Los Vilos area, Eastern- and Western Series are overprinted by numerous post subduction structures of Triassic or of Cretaceous ages.

9.1 Rio Maule

Structural and finite strain data show, that there is no structural break across the boundary of the Eastern and Western Series. In this Constitución – Rio Maule area the accretionary wedge represents a continuous structural section. The structural development along the Rio Maule shows distinct changes in the style of deformation from east to west (cp. Chapter 7): Upright large-scale folds become progressively overturned to the west and finally are converted into isoclinal, sheared, recumbent, small-scale intrafolial folds.

The finite strain data are in line with structural continuity across the contact. Plotting $\gamma_{oct.}$ values against distance in the east – west direction (Fig. 9.1) illustrates a continuous and smooth increase in the strain magnitude from east to west. It is important to note that there are no detectable breaks in $\gamma_{oct.}$ values across the contact between the both series.

This progressive structural and strain evolution can be interpreted to reflect a continuous tectonic evolution in the accretionary wedge. With increasing vertical shortening kinematic indicators change from top-to-the-west in the central part of the area to alternating top-to-the-west and top-to-the-east shear sense indicators in the westernmost part of the transect. This progressive structural change has been caused by a temporal change in the mode of accretion which is portrayed by using the flow line model for accretionary wedges by Feehan & Brandon (1999) and Ring et al. (1999) in Chapter *12.1: Tectonic model for the Chilean accretionary wedge*.

Fig. 9.1:Diagram showing gradual increase of the conventional octahedral shear strain, γ_{oct}, from east to west across the contact between the Eastern and Western series (contact is indicated by horizontally hatched pattern).
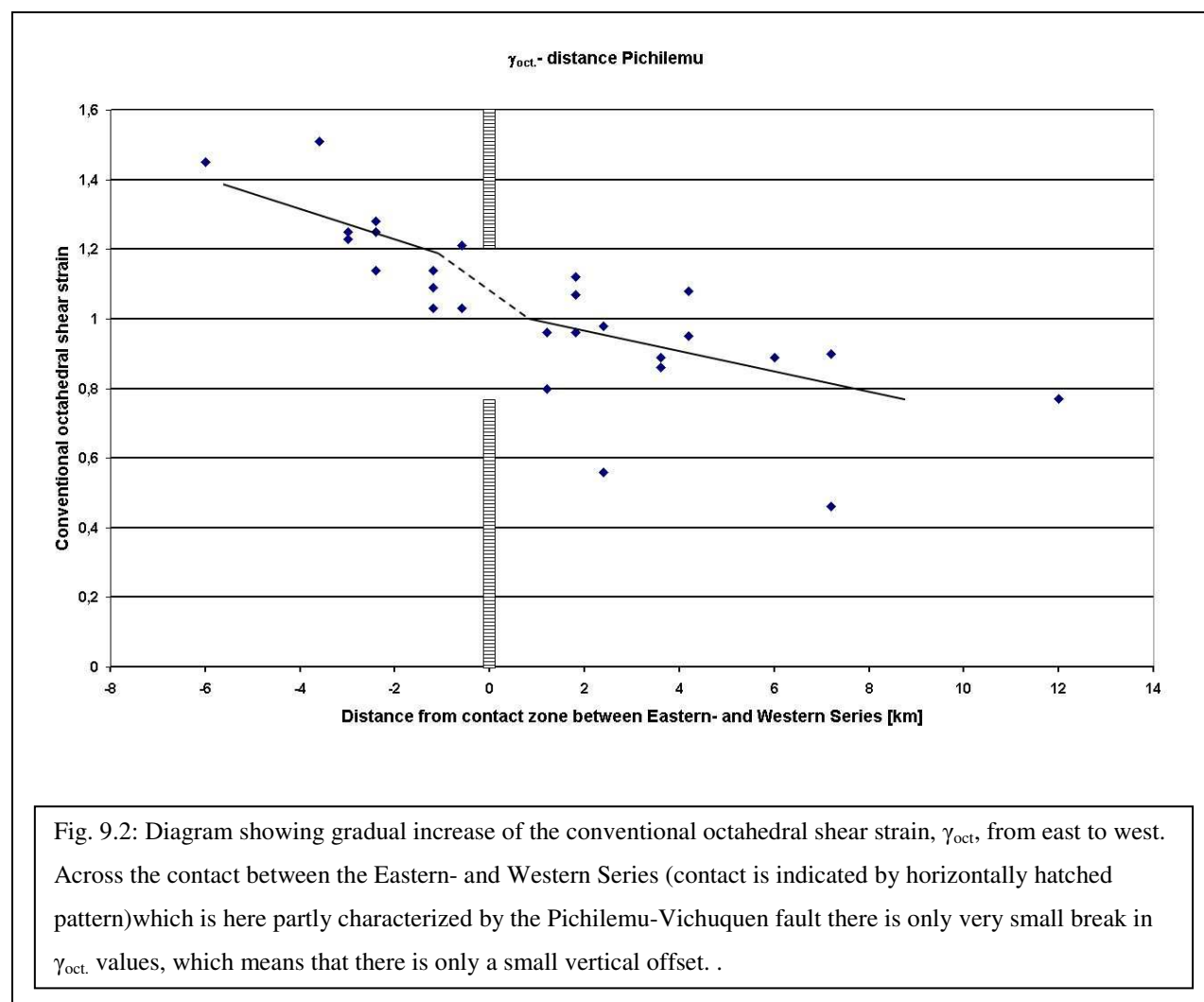
9.2 Pichilemu

Basically the Pichilemu area shows the same structural progression and the same finite strain patterns as the Rio Maule area. Unlike the southern part of the working area the Eastern and Western Series are divided by the Pichilemu – Vichuquén fault which crops out between Pichilemu and the Lago Vichuquén. This prominent brittle fault structure is probably of Cretacious ages (WILLNER ET AL., 2005). It was first shown by Hervé et al. (1984) that it cuts isogrades produced during the high temperature metamorphic overprint of the Eastern Series. The fault is characterized by cataclastic rocks and in the surrounding area of the main fault plane, smaller mesoscopic brittle faults appear. These fault structures contain breccia and thin clayey layers at the dm scale. Several tectonic structures like Riedel shears, extension cracks and fibre growth can be observed. They show reverse faulting and a lateral shear component, which is consistent with the subhorizontal shortening axes and subvertical extension axes near

the fault. Away from the direct vicinity of the fault no minor fault planes can be observed in the field.

The deformation field caused by the fault varies from the one caused by the accretionary wedge. Mostly z-axes are subnormal to the trace of the fault. Only in some cases there are oblique orientations, which might be due to some local rotation during strike-slip movement. The Pichilemu-Vichuquén fault cuts Jurassic sediments and therefore it must be younger or has developed synsedimentary. Willner et al. (2005) associated the fault with a cyclic accelerated cooling and exhumation as derived from the interpretation of fission track ages of apatite (80-113 Ma) and modelling of track length. In north – central Chile fission track ages from apatite around 100 Ma are widespread.

Thus the Pichilemu-Vichuquén fault does not represent a structure related to the ancient accretionary wedge. But indeed in the vicinity of the fault the younger structures have obscured the original structures and orientations of the accretionary system by the episodic shortening events during continuing activity along the convergent margin.

Fig. 9.2: Diagram showing gradual increase of the conventional octahedral shear strain, γ_{oct}, from east to west. Across the contact between the Eastern- and Western Series (contact is indicated by horizontally hatched pattern)which is here partly characterized by the Pichilemu-Vichuquen fault there is only very small break in $\gamma_{oct.}$ values, which means that there is only a small vertical offset. .

Whereas the fault has only one main fault plane in the northern part, it splits into three strands in the southern part (e.g. Fig. 8.1). The eastern and the intermediate part of these strands cut off the Mesozoic cover sediments from the adjacent Paleozoic batholith and the Eastern Series. The western part of these three endings traces the contact zone between Eastern- and Western Series down to the Lago Vichuquén, where it is cut off and replaced by the transitional structure as described in the Rio Maule area.
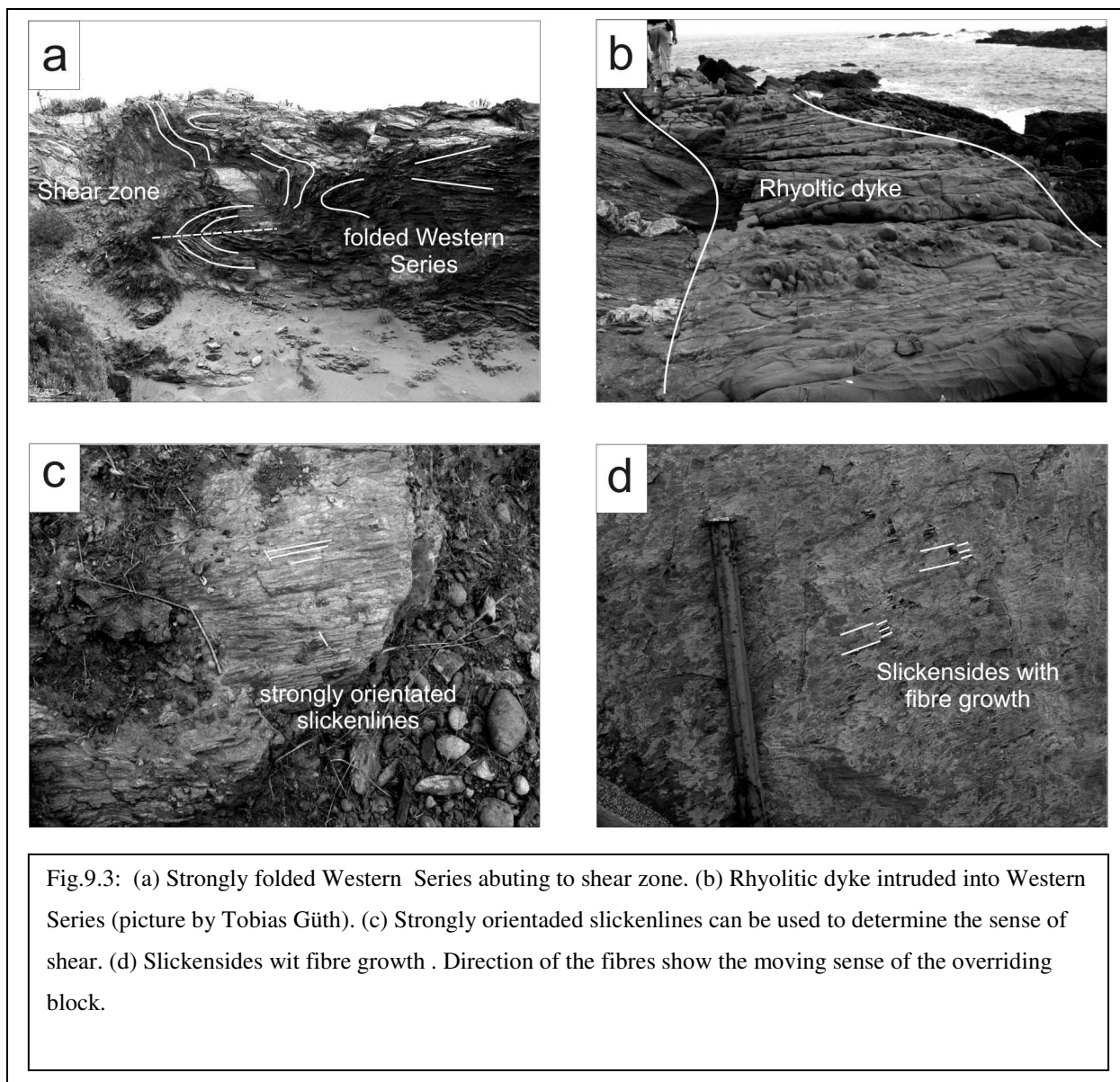
The Pichilemu-Vichuquén fault represents a left-lateral strike slip fault with a reverse faulting component, which is often poorly exposed. As shown by the strain data (Chapter 8) the vertical offset could not have exceeded 3-4 km, because there are no huge breaks in the $\gamma_{oct.}$ values across the fault (Fig. 9.2). However, the lateral offset which cuts off the isogrades is much larger. This is also shown in the $\gamma_{oct.}$ contour lines which adopt to have probably an offset of 20-25km (e.g. Fig. 8.4).

9.3 Los Vilos

The Los Vilos area is characterized by several N-S striking, cataclastic shear zones. The single shear zones considerably vary from each other, but most of them are steep (75°-90°) left lateral strike slip faults with a minor thrust component. Because of the steep alignment of the shear planes they sometimes plunge to the east or to the west and even single shear zones change their dip if they are traced over a longer distance.

The thrust component is solely orientated towards the north, but is in most cases rather small. The shear zones have a thickness of approximately 5-30m. These zones are characterized by cataclastic rocks and a higher amount of quartz veins. The sense of shear of the single zones has mostly been determined by the geometry of Riedel shears and the orientation of slickensides.

These faults are often in combination with the appearance of rhyolytic and basaltic dykes, which are relatively older than the shear zones. In some cases the shear zones cause an offset of the dykes. In other cases (only in the rhyolitic dykes) deformation structures, like the development of a foliation in the dykes, parallel to the foliation in the surrounding rocks, can be observed. Generally the basaltic dykes are younger than the rhyolitic ones.

Fig.9.3: (a) Strongly folded Western Series abuting to shear zone. (b) Rhyolitic dyke intruded into Western Series (picture by Tobias Güth). (c) Strongly orientaded slickenlines can be used to determine the sense of shear. (d) Slickensides wit fibre growth . Direction of the fibres show the moving sense of the overriding block.

Because of the numerous shear zones the original structures of Eastern and Western Series have been partly overprinted. S_0 and S_1 foliations are very prominent in the Eastern Series and also show these large scaled upright folds. Generally the folds get smaller further to the west and in the vicinity of the shear zones often small isoclinal folds on the m to the dm scale can be observed.

These folds have a plunge direction towards NW, which coincides with the mostly left lateral sense of shear of the often east dipping shear zones with thrust component. Within the Eastern Series there is a huge amount of inserted mudstone layers. Inside these mudstones a lot of shear zone parallel shear fractures can be observed as well as extension fractures, which also reflect the sense of shear.

In contrast to other parts of the study area, the Western Series has not this subhorizontal isoclinal S_2 folds, but is characterized by a very open folding, with random orientated limbs dipping to all directions. The main orientation of the S_2 planes is rather flat, except near the faults where the foliation is steepened. In the Western Series kinkbands can often be observed, which have a N-S trending orientation and are parallel to the shear zones.

At the contacts between the series there larger breaks in the $\gamma_{oct.}$ values can be observed. Thus there must have been a larger vertical offset (Fig. 8.5), and probably as well a very huge lateral displacement.
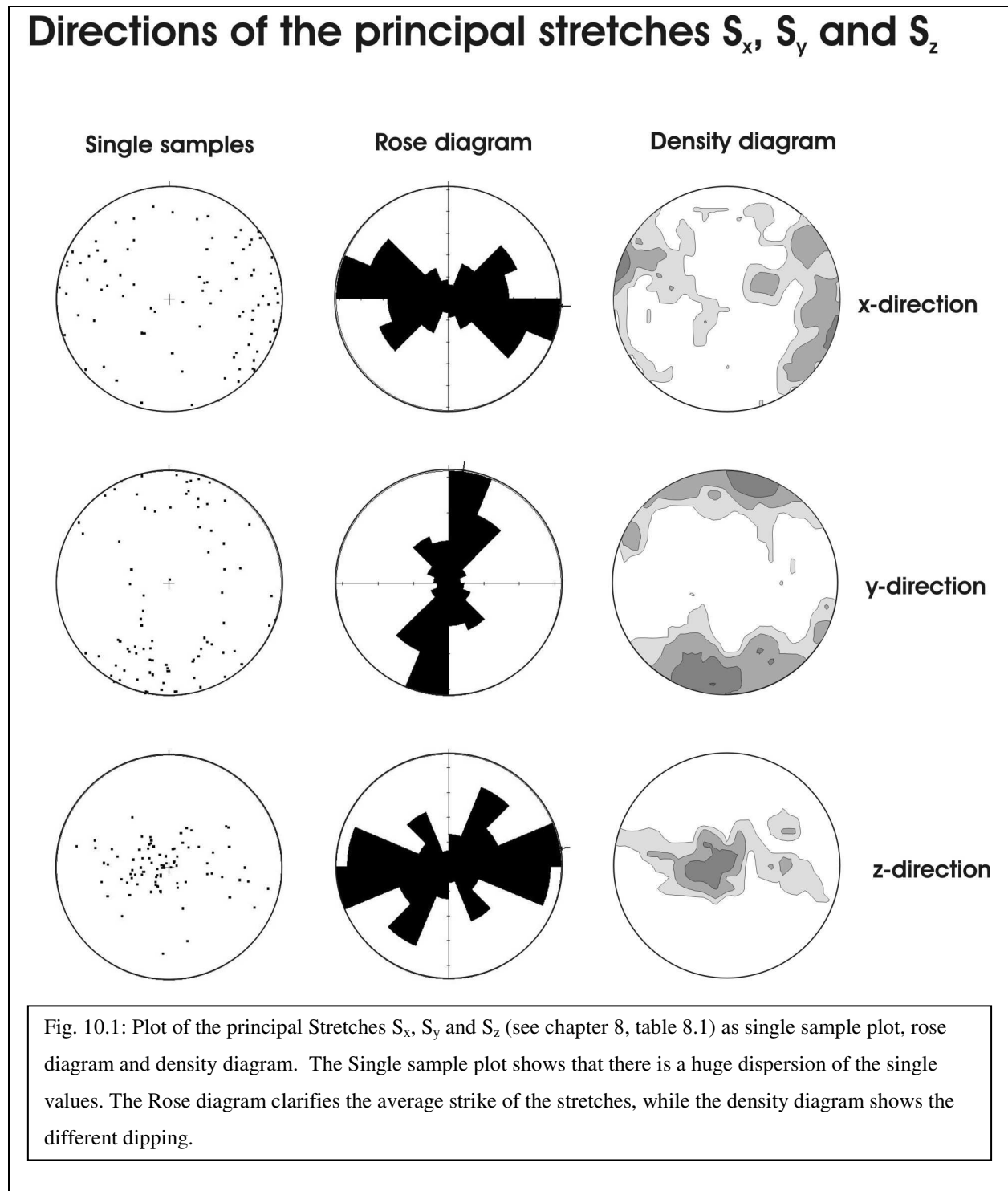
10. Vertical ductile thinning and exhumation

The reported finite-strain data from the accretionary wedge in Chile (Chapter *8: Strain data*) can be used to quantify the contribution of vertical ductile shortening to exhumation. Vertical ductile shortening is, together with erosion and normal faulting, a process that can aid the exhumation of high-pressure rocks, as shown in the schematic illustration by Feehan & Brandon (1999) (Fig. 1.2). Because the vertical rate at which rocks move through their overburden, and the rate of thinning of the remaining overburden at each step along the exhumation path have to be considered (FEEHAN & BRANDON, 1999), very large shortening strains of the order of 70-90% in exhumed high-pressure rocks are needed. Otherwise this process does not aid the exhumation of high-pressure rocks significantly. The deviatoric strain data, obtained by X-ray texture goniometry in phyllosilicate-rich rocks and R_f/Φ analyses in sandstones have shown tensor averages of relative finite strain of S_x =1.65, S_y =0.89 and S_z=0.59. From additional PDS measurements tensor averages of absolute finite strain of 1.24 for S_x, 0.82 for S_y and 0.57 for S_z have been obtained. The average of relative finite strain is indicating a greater vertical shortening in the structurally deeper units.

For calculating the amount of vertical ductile thinning, the program EXHUME (FEEHAN & BRANDON, 1999) was used. The calculation was accomplished with the assumption of a steady state wedge, but thought has been given to the fact that every increase of vertical ductile thinning distributes faster through a continuously thinned out block of the overlying bedding.

As parameters for the residence time of rocks in the wedge, PT data from Willner et al. (2002) have been used. The maximum metamorphic pressure is determined by the thickness of the wedge *H* (Metamorphic conditions in the Western Series: 8-10 kbar and 300-400°C at 292-319 Ma. Subduction-related PT conditions in the Eastern Series are unknown but generally less than in the Western Series. Zircon and apatite fission track ages of 206-221 Ma and 80-112 Ma indicate that both series were slowly exhumed together at rates of 0.2-0.4 km Myr^{-1}. Due to this data a residence time of approximately 90 Ma can be assumed. Furthermore the Western Series must have been subducted to a depth of 30-35km and the overlying Eastern Series to a depth of 20-25 km.

The kinematic vorticity number w* (see chapter:5.1.4) is needed for the calculation of vertical ductile thinning. The calculations with the FIBER program (chapter 5.1.4) show that the average rotation angle, in the structurally upper units of the Easter Series, is 10.2°. Because

structural and strain data show that Eastern and Western Series represent a continuous section and no larger normal faults or shear zones have been observed, this rather low rotational angles can be assumed for the structurally deeper Western Series as well.

Fig. 10.1: Plot of the principal Stretches S_x, S_y and S_z (see chapter 8, table 8.1) as single sample plot, rose diagram and density diagram. The Single sample plot shows that there is a huge dispersion of the single values. The Rose diagram clarifies the average strike of the stretches, while the density diagram shows the different dipping.

For the average directions of the principal stretches the values for S_x, S_y and S_z have been plotted (Fig. 10.1). They show that S_x and S_y are plunging subhorizontally, while the S_z values

have a steep dipping angles. For the average directions the values $S_x = 93°/05°$, $S_y = 04°/01°$ and $S_z = 267°/82°$ have been calculated.
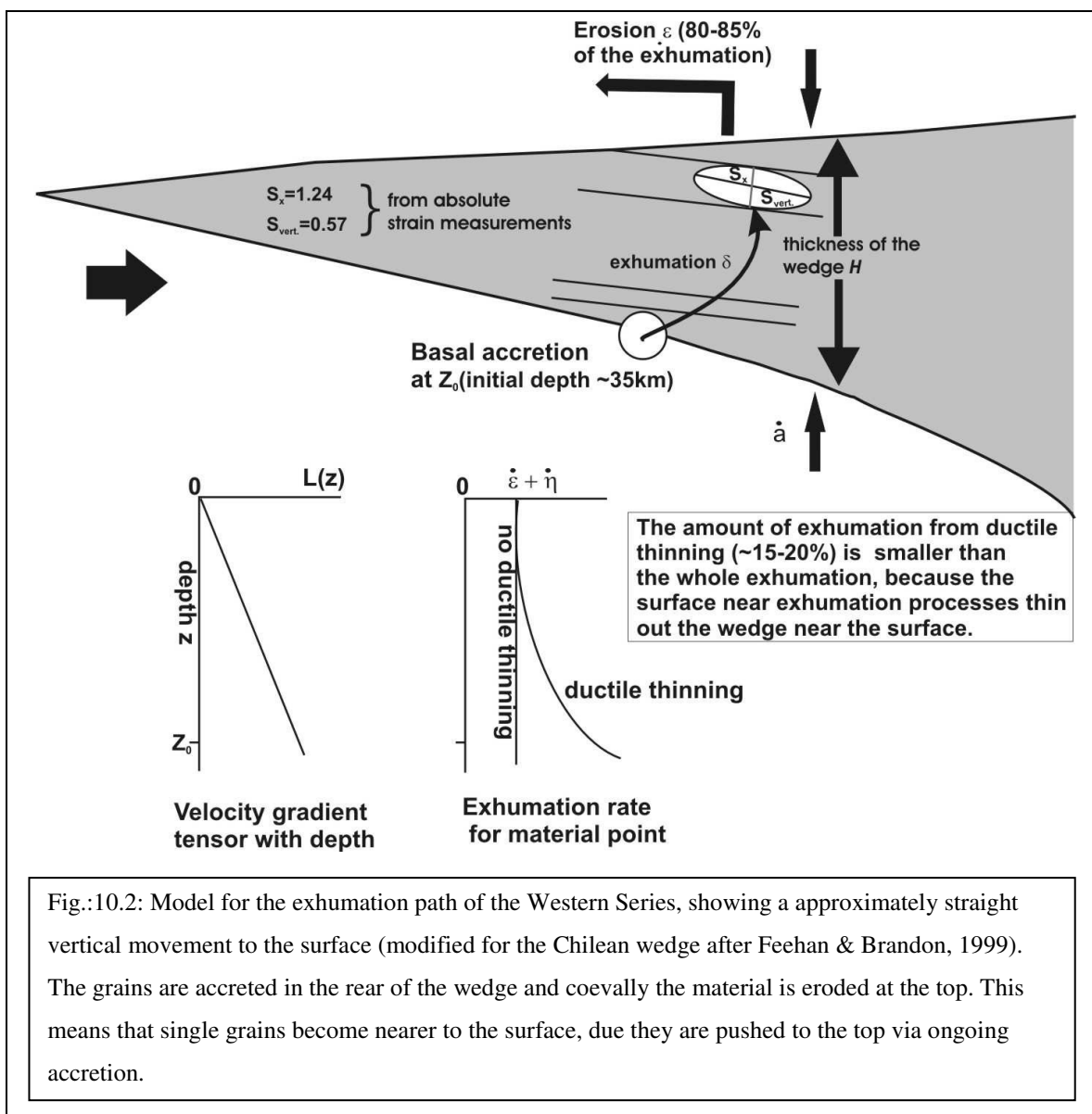
The results of the calculations with slightly varying input data (subduction depth, rotation angle) show that the average percentage of exhumation due of ductile flow is 17.5 %. The values are varying, depending on the input parameter, between ~ 15% - 20%.

Time (m.y.)	Depth (km)	Sx	Sy	Sz	Sv
0.00	35.00	1.000	1.000	1.000	1.000
4.50	32.55	1.023	0.979	0.942	0.943
9.00	30.25	1.045	0.960	0.891	0.894
13.50	28.06	1.066	0.943	0.846	0.850
18.00	25.97	1.086	0.927	0.806	0.811
22.50	23.98	1.104	0.912	0.771	0.777
27.00	22.07	1.122	0.899	0.740	0.747
31.50	20.23	1.138	0.887	0.713	0.720
36.00	18.46	1.153	0.877	0.689	0.697
40.50	16.74	1.167	0.867	0.668	0.676
45.00	15.08	1.180	0.859	0.649	0.658
49.50	13.46	1.191	0.851	0.633	0.642
54.00	11.87	1.201	0.844	0.619	0.628
58.50	10.32	1.211	0.838	0.607	0.616
63.00	8.79	1.218	0.833	0.597	0.606
67.50	7.29	1.225	0.829	0.588	0.598
72.00	5.81	1.231	0.826	0.581	0.591
76.50	4.35	1.235	0.823	0.576	0.586
81.00	2.89	1.238	0.821	0.573	0.582
85.50	1.44	1.240	0.820	0.570	0.580
90.00	0.00	1.240	0.820	0.570	0.579

Table 10.1: Showing a calculation from the program EXHUME with rocks which are exhumed from a depths of 35km to the surface dependent on time. The amount of solved material (Sv) decreases the nearer the material comes to the surface. The Principal stretches Sx, Sy and Sz change during ongoing exhumation.

The thinning rate due to erosion and normal faulting (km/m.y.) would be 0.321 and the thinning rate at base of wedge due to ductile flow (km/m.y.) is calculated with 0.239. For the rate of basal accretion 0.560 (km/m.y.) have been determined from the calculations.

The remaining 80-85% of exhumation must be due either to erosion or to normal faulting. No large-scale normal faults have been mapped so that it has to be assumed that most of the exhumation is due to erosion (Fig. 10.2).

Fig.:10.2: Model for the exhumation path of the Western Series, showing a approximately straight vertical movement to the surface (modified for the Chilean wedge after Feehan & Brandon, 1999). The grains are accreted in the rear of the wedge and coevally the material is eroded at the top. This means that single grains become nearer to the surface, due they are pushed to the top via ongoing accretion.

11. Mass balance

From the PDS measurements on quartz grains an average volume loss of 41% has been calculated (Chapter: 8.2). With the RADIUS method and measurements on quartz vein containing samples a mass balance can be presented, based on the parameters of chapter 6.

In order to illustrate the distribution of the different amounts of veins in Fig.11.1, the results of the measurements on thin section scale and on the sample scale are plotted together. It has to be annotated that this are standardized values to compare the different trends to each other. In absolute values the total amount of solved material increases to the west in every case. Huge quartz veins (on several cm to dm scale) in field have solely been observed in the Western Series. Therefore this approximation gets increasingly imprecise in the coastal areas of zone III.

The contacts of zones I – III and are manually chosen that way, that they reflect the percentages of SiO_2 veins in the rocks. It can be observed, that the lines of the same percental amounts are running subparallel to each other.

At first view there are two different trends observable. The first one shows that small veins <1mm decrease from east to west. Although in the easternmost parts the quartz veins reach an amount of more than 50% relative to the amount of quartz grains affected by pressure solution, the absolute amount is rather small. In zone III in the west, the amount of veins in the thin sections is smaller than 30% and has decreased relative to zones I and II, whereas the absolute amount of solved material has increased, because the total volume of solved material is much more than in the eastern part.

The second trend shows the veins with 1mm to 2cm width. In zone I in the east the amount of these veins is with <30% rather small, although it must be seen relative to the minor amount of quartz, which is solved as a whole.
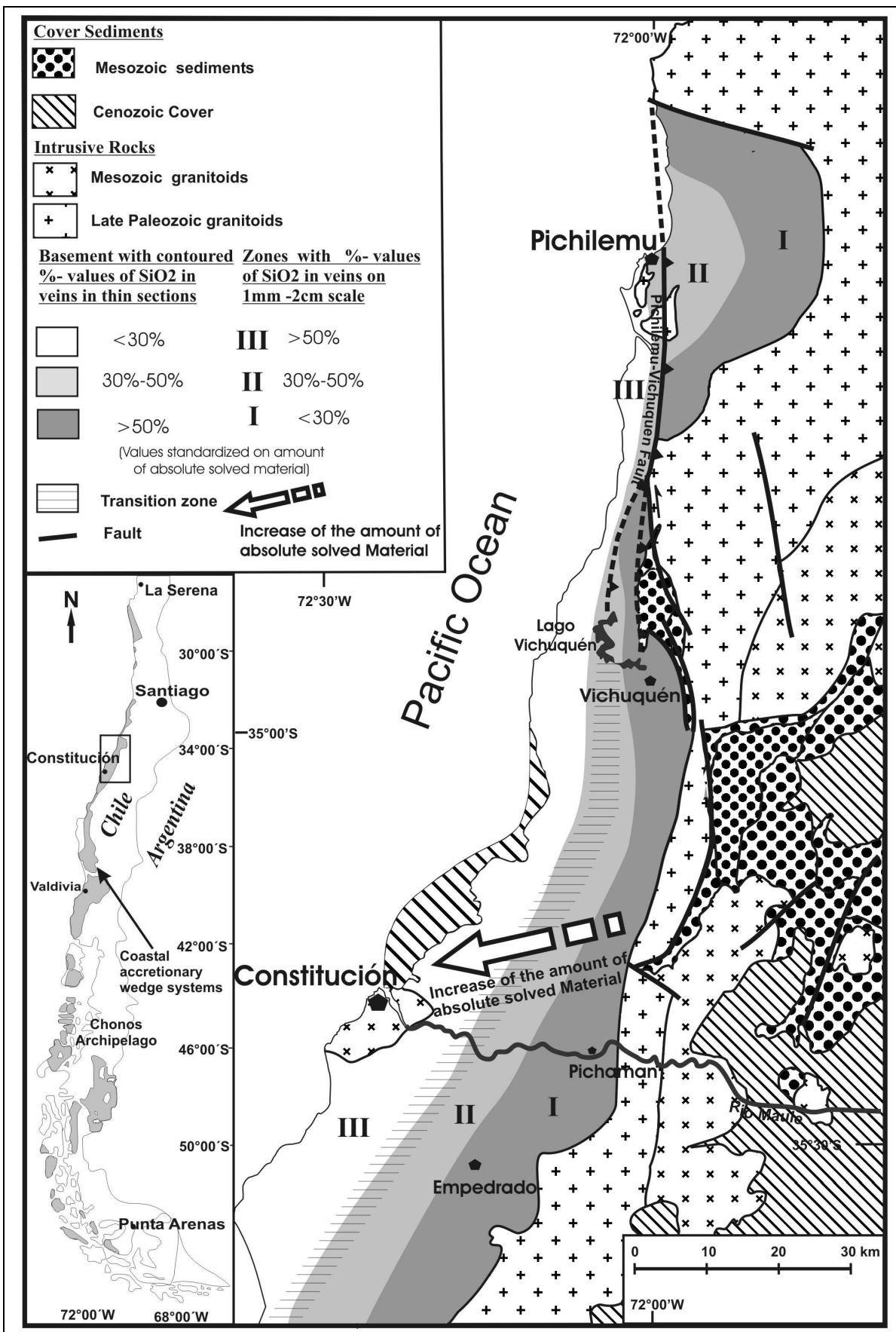
Fig. 11.1: Contour map of the distribution of quartz veins of different scales in the Constitución – Pichilemu area.

Although, on a first look, these two trends seem to run in an opposite direction they are following the same trend. This means that the scale of the veins in which SiO_2 precipitated change from east to west. In the eastern part the precipitated material is frequently bound in smaller veins, whereas to the west the amount of the wider veins increases and become the major factor in zones II and III. This matches also with the fact that huge veins only have been observed in the Western Series and that field observation that quartz veining and quartz rodding becomes more prominent to the west (see chapter *7: Structural data*).

The observations from the outcrop scale support this general trend. Veins on the dm scale become more and more prominent in the structurally deeper units and although they are difficult to quantify they fit into the distribution pattern of the quartz veins.

Even if the scale on which the solved quartz reprecipitates changes, the total amount of solved material increases, which coincides with the fact that the rocks of the Western Series have been subducted to much greater depths than the Eastern Series. Therefore, they have much larger octahedral shear strain values promoting of greater amounts of SiO_2 dissolution.

12. Discussion and Conclusion

12.1 Tectonic model for the Chilean accretionary wedge

The main aim of this study is to develop a comprehensive tectonic model for the Chilean wedge based on the presented structural and strain data.

In chapter *7: Structural data* it has been shown that there are no structural breaks across the boundary between Eastern Series and Western Series. This leads to the conclusion, that the Late Paleozoic accretionary wedge of central Chile represents a continuous structural section. This structural continuity across the contact is fully corroborated by the finite strain data of chapter *8: Strain data*. This can be interpreted as a progressive structural and strain evolution along the Rio Maule transect showing distinct changes in the style of deformation from east to west. Upright large-scale chevron folds become progressively overturned to the west and finally become isoclinal, sheared, recumbent, small-scale intrafolial folds in the west, along with an increase in strain magnitude to the west. With increasing vertical shortening kinematic indicators change from top to the west in the central part of the cross section (Chapter 7, Fig.7.1) to alternating top to the west and top to the east shear sense indicators in the westernmost part of the transect (Chapter 7 Fig. 7.9).

It can be envisaged that this progressive structural change was caused by a temporal change in the mode of accretion. This can be portrayed by using the flow-line model for accretionary wedges by Feehan & Brandon (1999) and Ring et al. (1999) (see chapter *1.1: Mode of accretion*). The rocks of the Eastern series were accreted frontally before c. 300Ma (Fig. 12.1. (a). This frontal accretion promoted horizontal shortening and the development of upright bedding folds. In the ancient wedge of central Chile some rocks followed a flow path that was nearer to the surface than others. Metamorphic processes associated with deformation in the deeper parts of the wedge promoted the development of axial plane foliations, which created the S_0-F_1-S_1 overprinting relationships common in the eastern part of the Eastern Series. Further to the west in the Eastern Series F_2 and S_2 become prominent. It can be suggested, that offscrapping of water rich trench sediments almost fully decoupled the sediments from the mafic rocks of the oceanic crust and therefore only a few imbricated metabasic rocks occur in the Eastern Series.
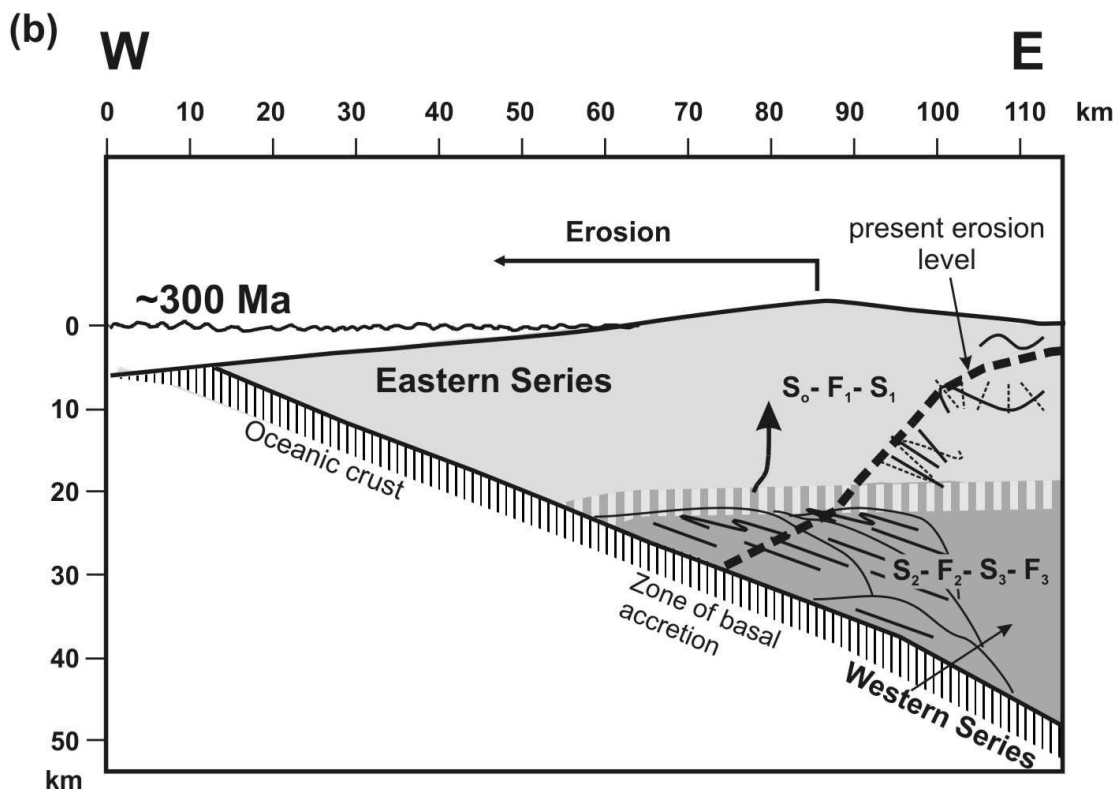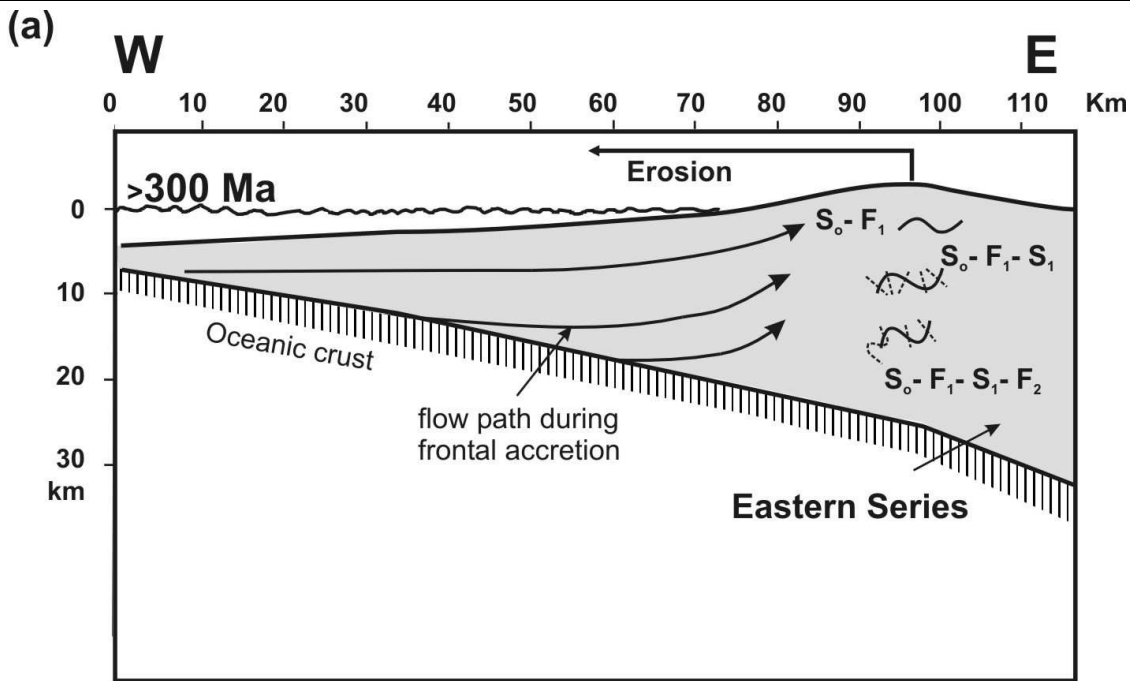
Fig. 12.1.(a) &(b): Proposed tectonic evolution of Late Palaeozoic accretionary wedge illustrated by flow-line model of Feehan & Brandon (1999) and Ring et al. (1999). (a) Frontal accretion of the Eastern Series before 300 Ma. The material is shuffled horizontally through the wedge and bedding is deformed by upright folds due to horizontal E-W shortening. (b) Change to basal accretion as evidenced by the ~300 Ma ages for high-pressure metamorphism in the Western Series. The change in the mode of accretion caused a fundamental change in the flow field and caused vertical shortening as indicated by the subhorizontal foliation. The consistent orientation of the underplating-related stretching lineations and west-vergent folding in the deeper parts of wedge suggests considerable basal traction and also increased imbrication of slices of oceanic crust from the downgoing plate. The lowermost rocks of Eastern Series where affected by basal traction and the F_2 folds are west-vergent near contact to the Western Series. Note that in the Western Series rocks only F_2, S_2, F_3 and S_3 structures have been observed and S_1 occurs only as relicts in these rocks. The pressure of the metamorphic overprint of ~3 kbar indicates that Eastern Series was in the upper crust (10-12 km depth).

At ~300 Ma the mode of accretion changed (Fig.12.1(b).) After being underplated below the accretionary wedge, the rocks of the Western Series were metamorphosed at high-pressure conditions. Underplating caused a major change in the flow field within the wedge and gave rise to vertical shortening and the development of a subhorizontal foliation.

The preferred stretching lineation suggests that the degree of plate coupling is stronger than in other comparable wedges like the Torlesse. This is also consistent with marked imbrication of mafic material from the downgoing oceanic crust. The lowermost rocks of the Eastern Series were affected by this higher degree of coupling and thus basal traction, which caused shear deformation in the lower parts of the accretionary wedge. Due to this shear the F_1 folds have been successively refolded and their axial planes were overturned to the west near the contact to the Western Series.

The change in the mode of accretion can explain the progressive structural and strain evolution, but it cannot be decided whether the change in the mode of accretion was abrupt or wither frontal accretion gradually changed to basal accretion. However, the gradual change of structures and strain data are interpreted to reflect a gradual change. The model implies that the early subduction related metamorphism was continuous across the entire accretionary wedge. The scanty P-T data from the Eastern Series further north and south of the Constitución – Pichilemu area seem to be in line with this proposition.

Subsequently the eastern part of the Eastern Series was overprinted by a static high-temperature metamorphism related to the intrusion of the granitoids of the Early Palaeozoic magmatic arc. The metamorphism at ~300 Ma affected most of the Eastern Series and also the transition to the Western Series in the Rio Maule area. This contact metamorphism affected the rocks at pressures of ~ 3kbar, indicating that the Easter Series were in the upper crust at ~10-12km depth

At about the same time some of the Western Series rocks were underplated and experienced pressures of ~9kbar (30-35km depth) in the Rio Maule profile (WILLNER, 2005). This indicates that these two events occurred at the same time. Therefore they provide an estimate of the depths of the rocks of the Eastern and Western Series at this time. The rocks on which the pressure estimates were made are ~20km apart from each other, which matches with the amount of crustal section of ~20km as inferred from the pressure difference. Furthermore this suggests that the crustal section is largely in its original Late Carboniferous configuration. Because there is not pronounced present topographic difference in the ~20km horizontal distance between the locations on which the pressure estimates have been made, and there is structural continuity between both series, it can be envisaged that the differential exhumation

was resolved rather gradually over a wide region. This differential exhumation must have caused rotation about a horizontal axis of the region and implies backrotation of some 30-45° of earlier formed structures.

A transect with similar structures has been described in the Chonos Archipelago, by Davidson et al. (1987). P-T conditions in the structurally equivalent Eastern belt of the Chonos Archipelago were determined at 5.5 kbar and 250-280 °C which is very similar to the Rio Maule area.

About the same time when the mode of accretion changed at ~300 Ma, the main phase of the intrusion of the magmatic arc took place. This was approximately going on for the next 50 Ma with attenuating activity (e.g. WILLNER, 2005). These magmas are crustal dominated but were intruding into an only marginal thickened crust (LUCASSEN ET AL., 2004). This change in the mode of accretion might be associated with an incremented steepening of the slab. Numerical models of Gorczyk et al. (2007) show that an increased subduction angle might cause the uprise of asthenospheric mantle material with the main production of magma at the beginning of the intrusion and decreasing productivity, while the subduction angle is becoming shallower again.

During Mesozoic times (225-100 Ma) structures of a contractional episode which shortened the forearc formed. These structures crop out in the Pichilemu area but anyhow, the structures of the ancient accretionary wedge are well preserved in this area, except in the direct vicinity of the Pichilemu- Vichuquén fault.

12.2 Comparison to other circumpacific wedges

In the introduction it is mentioned that there are different architectures of the circumpacific accretionary wedges which might reflect changes in the mode of accretion. The Franciscan, Aleutian and Japanese wedges are cases in which the initially subducted rocks were underplated and subsequently accretion became more frontal. The change to frontal accretion caused late horizontal shortening across the wedge and initiated late out of sequence faulting e.g. The Coast Range fault zone in the Franciscan subduction complex (BOLHAR & RING, 2001).

The Chilean coastal accretionary wedge and the Torlesse wedge belonged to the same subduction system that fringed the Gondwana margin in late Palaeozoic and early Mesozoic times. Therefore, they have a deal in common and a lot of similarities can be unravelled. In this context, especially the structural evolution, the distribution pattern of finite strain data as well as the architecture are remarkable. Although coastal accretionary wedge in Chile is of Late Paleozoic time in contrast to the Torlesse accretionary wedge in the South Island of New Zealand which is of Jurassic times (MORTIMER, 1993; DECKERT & BRANDON, 2005; RAHL ET AL., 2005; RING ET AL., 2005).

In the Coastal accretionary belt of Chile, the Torlesse and the Olympics accretionary wedges the opposite accretionary sequence seems to be the case and initial frontal accretion was followed by deep underthrusting. For the Chilean wedge it has been shown that a temporal, gradual change from an early relatively weak subvertical foliation in the frontally accreted Eastern Series to a penetrative subhorizontal transposition foliation in the underplated a basally accreted rocks of the Western Series, took place. The change from frontal accretion to underplating was gradual as well.

Deckert & Brandon (2005) and Ring et al. (2005) showed that a similar transitional contact characterizes the contact between the frontally accreted and underplated rocks in the Torlesse of New Zealand, and this also has been observed in the Olympics subduction wedge (BRANDON ET AL., 1998). Furthermore, the Torlesse wedge also shows no significant synaccretionary structural discontinuities or larger structural breaks (DECKERT ET AL., 2002). For the Torlesse wedge Ring et al. (2005) postulated a similar accretionary history that it has been deciphered for the Chilean wedge in this study.

The change from frontal to basal accretion in the Torlesse may have been due to a period of subduction erosion. This means, that the material at the toe of the wedge is removed by underthrusting and subsequently underplated at the base of the wedge.

Subduction erosion may have been caused by an incoming seamount chain or changes in the pore pressure along the basal decollement. Later on frontal accretion proceeded in the Torlesse wedge and caused a pronounced tectonic contact in the frontal part of the Torlesse wedge. However, the Torlesse wedge has a dimension of >600 km in diameter and is preserved much more complete than the coastal accretionary wedge of Chile which was during the Andean orogeny strongly modified and partially ancient structures have been destructed.

It remains speculative that the Chilean wedge had a similar tectonic evolution as the Torlesse. A notable difference between the two wedges is that the stretching lineation in the Torlesse is less consistent in orientation with an almost random pattern. Deckert & Brandon (2005) showed that the degree of plate coupling in the Torlesse wedge was rather weak and responsible for the weak preferred orientation of the stretching lineation. From the much more consistent NE- SW oriented stretching lineation in the Chilean wedge a stronger degree of coupling between downgoing and overriding plate has been derived.

12.3 Conclusion

In conclusion the following results of this study can be summarized:

- Due to the analyses of structural and strain data of the Chilean accretionary wedge a tectonic model has been developed, which shows that the ancient wedge was a continuous tectonic section.

- The mode of accretion changed from frontal to basal accretion at ~ 300 Ma.

- The amount of ductile thinning in the wedge is with 15%-20% rather low. Because there is a lack of normal faulting as exhumation process, ~80% of the exhumation is due to erosion.

- Most of the solved material in quartz grains stays in the wedge and is precipitated in quartz veins. The wedge has predominantly characteristics of a closed system.

- The structures of the ancient accretionary wedge are in some areas partly destructed by younger faults and shear zones. The direct vicinity of these areas are not applicable to quantify the accretion related structures any more.

Therefrom, it has been shown that Eastern Series as well as Western Series belong to the pre – Andean coastal accretionary belt of Chile and their different P-T-t-D evolutions reflect in the mode of accretion through time. Subsequent differential exhumation did not occur along discrete faults, but was resolved rather gradually over a wide region, which in turn implies that exhumation was not tectonically controlled. The Constitución area is a perfectly preserved transect to study the late Paleozoic accretionary prism. During Mesozoic times compressional episodes occurred, which shortened the forearc and partly affected the older Paleozoic structures, although they are anyhow well preserved in most parts of the study area. These structures are exposed in north-central Chile north of 35°S in the Pichilemu area. During Jurassic times with the Atacama fault system a left lateral strike slip system becomes more and more prominent. In Los Vilos younger shear zones cutting off Jurassic dykes are exposed which may reflect to this evolution.

12.4. Outlook

For the circumpacific accretionary wedges and especially the Chilean wedge there still remain a lot of open questions. Referring to the tectonic model (Chapter12.1) it is of great interest how and why the change in the mode of accretion took place. Furthermore it should be figured out if the degree of metamorphism increases in the same way as the strain magnitude from east to west.

At ~300 Ma the Paleozoic magmatic arc intruded into the Eastern Series and overprinted it partially, which means that there must have been a mantle wedge below this part of the accretionary wedge. Why does this magmatic activity occur at the same time with the change to underplating after the Eastern Series was already accreted?

The magmatic arc is largely undeformed but is highly contaminated with material from the crust. Has the change to the basal accretion mode caused this as well?

Furthermore it has to be unravelled how material is rearranged within the wedge and how long does it take to transport the material. This is only researched very fragmentary in the Chilean wedge, which makes it difficult to compare it to other well-investigated wedges e.g. the Torlesse.

However, the comparison between different wedges in the circumpacific area must be pressed ahead in the future and in detail it has to be investigated where are differences and where are similarities. Maybe it is possible to develop a superior model for different accretion modes and the reasons why there are changes, which is valid in all wedges.

13. References

AGUIRRE, L., HERVÉ, F. & GODOY, E. 1972. Distribution of metamorphic facies in Chile: an outline. *Krystallinikum*, **9**, 7–19.

AUSTRHEIM H., ERAMBERT, M., ENGVIK, A.K. 1997. Processing of crust in the root of the Caledonian continental collision zone: the role of eclogitisation. *Tectonophysics*, **273**,129-253.

BACH, A. 1974. A geochemical investigation of pressure solution and the formation of veins in a deformed grewacke. *Contributions to Mineralogy and Petrology*, **46**, 61-68.

BELMAR, M., MORATA, D., MUNIZAGA, F., PÉREZ DE ARCE, C., MORALES, S. & CARRILLO, F.J. 2004. Significance of K-Ar dating of very low-grade metamorphism in Triassic-Jurassic pelites from the Coastal Range of central Chile. *Clay Minerals*, **39**, 151-162.

BOLHAR, R. & RING, U. 2001. Deformation history of Yolla Bolly terrane rocks at Leech Lake Mountian, Eastern belt, Franciscan subduction complex. *Geological Society of America Bulletin*, **113**, 181-195.

BRANDON, M.T., RODEN-TICE, M.K. & GARVER, J.I., 1998. Late Cenozoic exhumation of the Cascadia accretionary wedge in the Olympic Mountains, northwest Washington State. *Geologic Society American Bulletin*, **110**, 985-1009.

BRANDON, M.T. & RING, U., 1997. Exhumation processes: Normal faulting, ductile flow and erosion. *GSA Today*, **7(5)**, 17-20.

BRANDON, M.T. 1995. Representation of geologic strain data in strain-magnitude space. *Journal of Structural Geology*, **17**, 1375-1385.

BRANDON, M.T., COWAN, D.S. & FEEHAN, J.G., 1994, Fault-zone structures and solution-mass-transfer cleavage in Late Cretaceous nappes, San Juan Islands, Washington: In: Swanson, D.A. & Haugerud, R.A. (eds): Geologic field trips in the Pacific Northwest, Geol. Soc. Am. Ann. Mtg., 1994, Seattle, Washington.

BRANDON, M.T. & CALDERWOOD, A.R. 1990, High-pressure metamorphism and uplift of the Olympic subduction complex. *Geology,* **12**, 1252-1255.

CHARIER, R., 1986. The Gondwana Glaciation in Chile: Description of alleged glacial deposits and Paleogeographic conditions bearing on the Extension of the ice cover in southern south America. *Palaeogeography, Palaeoclimatology, Palaeoecology*, **56**, 151-175.

CHARISSÉ, T., 2004: *Diploma mapping report*. Johannes Gutenberg-Universität Mainz.

COWAN, D.S. 1974. Deformation and Metamorphism of the Franciscan Subduction Zone Complex Northwest of Pacheco Pass, California. *Geological Society of America Bulletin,* **85**, 1623–1634.

COX, S.C. 1993. Veins, Fluid, Fractals, Scale & Schist. An investigation of fluid-rock interaction during deformation of the Torlesse Terrane, New Zealand. *Doctor thesis, University of otago Dunedin, New Zealand.*

COX, S.F., ETHERIDGE, M.A. & WALL, V.A. 1987. The role of fluids in syntectonic mass transport, and the localisation of metamorphic vein-type ore deposits. *Ore Geology Reviews*, **2**, 65-67.

DAVIDSON, J., MPODOZIS, C., GODOY, E., HERVÉ, F., PANKHURST, R.J. & BROOK, M. 1987. Late accretionary complexes on the Gondwana margin of southern Chile: evidence from the Chonos Archipelago. *In*: MCKENZIE, G.D. (ed.) Gondwana Six: Structure, Tectonics and Geophysics. Geophysical Monograph. *American Geophysical Union*, **40**, 221-227.

DECKERT, H., RING, U. & MORTIMER, N. 2002. Tectonic significance of Cretaceous bivergent extensional shear zones in the Torlesse accretionary wedge, central Otago Schist, New Zealand. *New Zealand Journal Geology and Geophysics*, **45**, 537-547.

DIPPLE, G.M., WINTSCH, R.P. & ANDREWS A.W. 1990. Identification of the scales of differential element mobility in a ductile fault zone. *Journal of Metamorphic Geology*, **8**, 645-661.

ERNST, W.G. 1975. Systematics of large-scale tectonics and age progressions in Alpine and Circum-Pacific blueschist belts. *Tectonophysics*, **26**, 229–246.

ETHERIDGE, M.A., WALL, V.J. & VERNON, R.J. 1983. The role of fluid phase during regional metamorphism and deformation. *Journal of Metamorphic Geology*, **1**, 205-226.

FEEHAN, J.G. & BRANDON, M.T. 1999. Contribution of ductile flow to exhumation of low-temperature, high-pressure metamorphic rocks, San Juan–Cascade nappes, NW Washington state, *Journal of Geophysical Reasearch*, **104**, 10883-10902.

FORSYTHE, R. 1982. The late Paleozoic to early Mesozoic evolution of southern South America: A plate tectonic interpretation. *Geological Society of London Journal*, **139**, 671-682.

FRANKLIN, J.N. 1968. *Matrix Theory*. Prentice Hall, New York.

GLODNY, J., LOHRMANN, J., ECHTLER, H., GRÄFE, K., SEIFERT, W., COLLAO, S., FIGUEROA, O. 2005. Internal dynamics of a paleoaccretionary wedge: insights from combined isotope tectonochronology and sandbox modelling of the south-central Chilean forearc. *Earth and Planetary Science Letters*, **231**, 23-39.

GODOY, E. 1970. Estudio petrográfico del granito de Constitución y su aureola de metamorfismo de contacto. Unpubl. B.Sc. thesis, Universidad de Chile, Santiago, 130 p.

GODOY, E. & KATO, T. 1990. Late Paleozoic serpentinites and mafic schists from the Coast Range accretionary complex, Central Chile: their relation to aeromagnetic anomalies. *Geologische Rundschau*, **79**, 121–130.

GONZALEZ-BONORINO, F. 1971. Metamorphism of the crystalline basement of central Chile. *Journal of Petrology*, **12**, 149–175.

GORCZYK, W., WILLNER, A.P., GERYA, T.V., CONELLY, J. & BURG, J.P. 2007. Physical controls of magmatic productivity at Pacific-type convergent margins: Numerical modelling. Physics of the Earth and Planetary Interior (in review).

Güth, T., 2004. *Diploma mapping report*. Johannes Gutenberg-Universität Mainz.

HERVÉ, F., KAWASHITA, K., MUNIZAGA, F. & BASSEI, M. 1984. Rb–Sr isotopic ages from late Paleozoic metamorphic rocks of Central Chile. *Journal of the Geological Society, London*, **141**, 877–884.

HERVÉ, F. 1988. Late Paleozoic subduction and accretion in Southern Chile. *Episodes*, **11**, 183–188.

HERVÉ, F., MUNIZAGA, F., PARADA, M. A., BROOK, M., PANKHURST, R. J., SNELLING, N. J. & DRAKE, R. 1988. Granitoids of the coast range of central Chile: geochronology and geologic setting. *Journal of South American Earth Sciences*, **1**, 185–194.

HERVÉ, F., DEMANT, A., RAMOS, V.A., PANKHURST, R.J. & SUÁREZ, M. 2000. The Southern Andes. *In*: CORDANI, U.G., MILANI, E.J., THOMAZ FILHO, A. & CAMPOS, D.A. (eds.) *Tectonic Evolution of South America*, Rio de Janeiro, 605-634.

HOSSACK, J.R. 1968. Pebble deformation and thrusting in the Bygdin area (Southern Norway). *Tectonophysics*, **5**, 315-339.

IRVINE, J.J., GARCÍA, C., HERVÉ, F. & BROOK, M. 1988. Geology of part of a long-lived dynamic plate margin: the coastal Cordillera of north-central Chile, latitude 30°51´-31°S. *Canadian Journal of Earth Sciences*, **25**, 603-624.

JAEGER, J.C. & COOK, N.G.W. 1979. *Fundamentals of rock mechanics*. Third edition, Chapman & Hill, London.

KATO, T. T. 1985. Pre-Andean orogenesis in the Coast Ranges of Central Chile. *Geological Society of America Bulletin*, **96**, 918–924.

KERRICH, R. & ALLISON, I. 1978. Flow mechanisms in rocks: Microscopic and mesoscopic structures, and their relation to physical conditions of deformation in the crust. *Geoscience Canada*, **5(3)**, 109-118.

LUCASSEN, F., TRUMBULL, R., FRANZ, G., CREIXELL, C., V_ASQUEZ, P., ROMER, R. L. & FIGUEROA, O. 2004. Distinguishing crustal recycling and juvenile additions at active continental margins: the Paleozoic to recent compositional evolution of the Chilean continental margin (36°–41°S). *Journal of South American Earth Sciences*, **17**, 103–119.

MARCH, A. 1932. Mathematische Theorie der Regelung nach der Korngestalt affiner Deformation. *Zeitschrift für Kristallographie*, **81**, 285-297.

MARIOTH, R. 2001. Charakterisierung und Quantifizierung thermischer und diagenetischer Prozesse im karbonischen Akkretionsprisma in Nordchile. Unpublished Ph.D. thesis, Univ. Heidelberg, 155 S.

MARTIN, M.W., KATO, T.T., RODRIGEZ, C, GODOY, E., DUHART, P., MCDONOUGH, M., CAMPOS, A. 1999. Evolution of the late Paleozoic accretionary complex and overlying forearc-magmatic arc, south central Chile (38°-41°): Constraints for the tectonic setting along the southwestern margin of Gondwana. *Tectonics*, **18**, No.4, 582-605.

MIYASHIRO, A. 1973. *Metamorphism and Metamorphic Belts*. Allen & Unwin, London.

MOORE, J.C. & ALLWARDT, A. 1980. Progressive deformation of a Tertiary trench slope, Kodiak Island, Alaska. *Journal of Geophysical Research*, **85**, 4741-4756.

MORTIMER, N. 1993. Jurassic tectonic history of the Otago shist, New Zealand. *Tectonics*, **12**, 237-244.

NADAI, A. 1950. *Theory of Flow and Fracture of Solids, Vol.1. Second edition*, McGraw Hill, New York.

NEWMAN, J. & MITRA, G. 1993. Lateral variations in mylonite zone thickness as influenced by fluid-rock interactions, Linville Falls Fault, North Carolina. *Journal of Structural Geology*, **15**, 849-8638.

NORABUENA, E.,. LEFFLER-GRIFFIN, L, MAO, A., DIXON, T.H., STEIN, S., SACKS, I.S., OCOLA, L. AND ELLIS, M.1998. Space geodetic observations of Nazca-South America convergence across the central Andes. *Science*, **279**, 358-362.

OERTEL, G. 1983. The relationship of strain and preferred orientation of phyllosilicate grains in rocks - a review. *Tectonophysics*, **100**, 413-447.

OWENS, W.H. 1984. The calculation of a best-fit ellipsoid from elliptical sections on arbitrarily orientated planes. *Journal of Structural Geology*, **6**, 571-578.

PASSCHIER, C.W., 1991, The classification of dilatant flow types: Journal of Structural Geology, 13, 101-104.

PASSCHIER, C.W. & TROUW, R. 1996, *Microtectonics*, Berlin, Springer, 289p.

PATERSON S.R., YU, H., OERTEL, G. 1995. Primary and tectonic fabric intensities in mudrocks. *Tectonophysics*, **247**, 105-119.

PEACH, H. & LISLE, R. 1979. A Fortran IV program for the analysis of tectonic strain using deformed elliptical markers. *Computers and Geosciences,* **5**, 325-334.

PEACOCK, S.M. 1996. Thermal and petrologic structure of Subduction zones. *In*: Subduction-Top to Bottom. Geophysical Monograph. Behout, G.E.,Scholl, D.W., Kirby, S.H. & Platt, J. (eds.): *American Geophysical Union*, **96**, 119-131.

PLATT, J.P., SOTO J.I., WHITEHOUSE, M.J., HURFORD, A.J., KELLEY, S.P. 1998. Thermal evolution, rate of exhumation, and tectonic significance of metamorphic rocks from the floor of the Alboran extensional basin, western Mediterranean. *Tectonics*, **17**, 671-689.

PLATT, J.P. 1975. Metamorphic and deformational Processes in the Franciscan Complex: California, Some insights from the Catalina schist terrane. *Geological Society American Bulletin*, **86**, 1337-1347.

PLATT, J.P., 1993. Exhumation of high-pressure rocks: a review of concepts and processes: *Terra Nova*, **5**, 119-133.

PRESS, W.H., FLANNERY, B.P., TEUKOLSKY, S.A. & VETTERLING, W.T. 1986. Numerical Recipes. The art of scientific computating. *Cambridge University Press ,* 526-528.

RAMSAY, J.G. 1967. *Folding and fracturing of rocks*. McGraw-Hill, New York.

RAMSAY, J.G., CASEY, M. & KLIGFIELD, R. 1983. Role of shear in development of the Helvetic fold-thrust belt of Switzerland. *Geology*, **11**, 439-442.

RAMSAY, J.G., & HUBER, M.I. 1983. The *Techniques of Modern Structural Geology, volume 1: Strain analysis*, Academic Press, New York.

RAMSAY, J.G. & WOOD, D.S. 1973. The geometric effects of volume change during deformation processes. *Tectonophysics*, **16**, 263-277.

REBELLEDO, S. & CHARRIER, R. 1997. Evolución del basamento paleozoico en el área de Punta Claditas, Región de Coquimbo, Chile (31-32°S). *Revista Geológica de Chile*, **21**, 55-69.

RICHTER, P.P., RING, U., WILLNER A.P. & LEISS, B. 2007. Structural contacts in subduction complexes and their tectonic significance: The Late Paleozoic coastal accretionary wedge of central Chile. *Journal of the Geological Society London*, **164**, 203-214.

RING, U. 1996. Volume strain, strain type and flow path in a narrow shear zone. *Geologische Rundschau*, **86**, 786-801.

RING, U. & BRANDON, M.T. 1994. Kinematic data for the Coast Range fault and implications for exhumation of the Franciscan complex. *Geology,* **22**, 735-738.

RING, U. & BRANDON, M.T. 1999. Ductile strain, coaxial deformation and mass loss in the Franciscan complex: Implications for exhumation processes in subduction zones. *In*: RING, U., BRANDON, M.T., LISTER, G.S., WILLETT, S. (eds.). Exhumation Processes: Normal faulting, ductile flow and erosion, *Geological Society London Special Publications*, **154**, 55-86.

RING, U. & BRANDON, M.T. 2006. The Tectonic Evolution of the Franciscan Subduction Complex: Implications for the exhumation of high-pressure rocks in subduction-related accretionary wedges. *Geological Society of America*, Special Paper, in press.

RING, U., BRANDON, M.T., WILLETT, S. & LISTER G.S. 1999. Exhumation processes. *In*: Exhumation Processes: Normal faulting, ductile flow and erosion, Ring, U., Brandon, M.T., Lister, G.S., Willett, S. (eds.). *Geological Society London Special Publications*, **154**, 1-27.

RING, U. & RICHTER, P.P. 2004. Normal faulting at convergent plate boundaries: The Del Puerto Canyon shear zone in the Franciscan subduction complex revisited. *Tectonics*, **23**, 1022, doi: 10.1029/2002TC001476, 12p.

RUMBLE, D., FERRY, J.M., HOERING, T.C. & BOUCOT, A.J. 1982. Fluid flow during regional metamorphism at the Beaver Brook fossil locality, New Hampshire. *American Journal of Science* ,**282**, 886-818.

SCHEUBER, E., BOGDANIC, T., JENSEN, A. & REUTTER, K.-J. 1994. Tectonic development of the north Chilean Andes in relation to plate convergence and magmatism since the Jurassic.- *In: Tectonics of the southern Central Andes: structure and evolution of an active continental margin.* (REUTTER, K.-J., SCHEUBER, E. & WIGGER, P.; EDS.), Heidelberg (Springer),121-139.

SCHEUBER, E. & GONZALEZ, G., 1999. Tectonics of the Jurassic Early Cretaceous magmatic arc of the north Chilean Coastal Cordillera (22-26°S): A story of crustal deformation along a convergent plate boundary. *Tectonics*, **18**, 895-910.

SEELOS, K. & SIROCKO, F., 2005. RADIUS – rapid particle analysis of digital images by ultra-high-resolution scanning of thin sections, *Sedimentology,* **52**, 669–681.

SELVERSTONE, J., 1985. Petrologic constraints on imbriction, metamorphism, and uplift in the SW Tauern window, Eastern Alps. *Tectonics*, **4**, 687-704.

SHIMAMOTO, T. & IKEDA, Y. 1976. A simple algebraic method for strain estimation from deformed ellipsoidal objects. 1. Basic theory. *Tectonophysics,* **36**, 315-337.

SUPPE, J. 1973. *Geology of the Leech lake Mountain-Ball Mountain region, California: A cross-section of the northeastern Franciscan belt and its tectonic implications.* University of California Press Vol. 107, Berkley.

SUPPE, J. 1978. Cross section across southern part of northern Coast Ranges and Sacramento Valley, California: (1:250,000 with map, gravity models, and 6 p. text), *Geological Society of America, Map and Chart Series*, MC-28B.

TULLIS, T.E. & WOOD, D.S. 1975. Correlation of Finite Strain from Both Reduction Bodies and Preferred Orientation of Mica in Slate from Wales. *Geological Society of America Bulletin,* **86,** 632–638.

WALLIS, S.R. & BEHRMANN, J.H., 1996. Crustal stacking and extension recorded by tectonic fabrics of the SE margin of the Tauern window, Austria: Journal of Structural Geology, **18**, 1455-1470.

WALLIS, S.R., PLATT, J.P. & KNOTT, S.D., 1993. Recognition of syn-convergence extension in accretionary wedges with examples from the Calabrian arc and the eastern Alps. *American Journal of Science*, **293**, 463-495.

WILLNER, A.P., 2005. Pressure–Temperature Evolution of a Late Palaeozoic Paired Metamorphic Belt in North–Central Chile (34°–35°30´S), *Journal of Petrology,* **46,** 1805-1833.

WILLNER, A.P., HERVÉ, F. & MASSONNE, H.-J. 2000. Mineral chemistry and pressure-temperature evolution of two contrasting high-pressure-low-temperature belts in the Chonos Archipelago, Southern Chile. *Journal of Petrology,* **41**, 309-330.

WILLNER, A.P., THOMSON S.N., KRÖNER, A., WARTHO J.-A., WIJBRANS, J. R., HERVÉ, F. 2005. Time Markers for the Evolution and Exhumation History of a Late Palaeozoic Paired Metamorphic Belt in North–Central Chile (34°–35°30´S), *Journal of Petrology,* **46***,* 1835-1858.

WOOD, D.S. & OERTEL, G. 1980. Deformation in the Cambrian slate belt of Wales. *Journal of Geology*, **88**, 309-326.